POLITECNICO DI TORINO

Ph.D. in Physics

XXXI Ciclo

Ph.D. Thesis

Study and Production of Special Targets for DCE Reactions with $0\nu\beta\beta$-Decay Final States in the NUMEN Experiment

Federico Pinna

2019

No neutrinos were harmed in the achievement of this Ph.D.

ABSTRACT

Among all the different fields of the Nuclear and Particle Physics, the research on neutrino-related topics is recently gaining more and more attention. The precise assessment of the neutrino mass is of extraordinary importance in theory elaboration. The same experiments that measure the neutrino mass are also focusing their efforts in detecting a Neutrinoless double β-decay ($0\nu\beta\beta$), a rare event in which two neutrinos annihilate each other. If observed, the consequences would deeply affect various branches of the current Modern Physics, from Nuclear Physics to Cosmology; for instance, it would prove the Majorana nature of the neutrino (i.e. to be its own antiparticle), deny the conservation of the lepton number, shed light on the abundance of the baryonic matter over the antimatter in the universe. As one can easily imagine, the potential of this discovery is enormous, yet there are several important issues to face. Two of them are the considerably long half-lifetime of the process (more than 10^{24} years) and the uncertainty in the Nuclear Matrix Element evaluation, due to the lack of experimental data. The latter was the reason for which the NUMEN experiment was conceived. The goal of the NUclear Matrix Elements for Neutrinoless double β-decay (NUMEN) Project is to measure the cross-section of Double Charge-Exchange (DCE) reactions, whose initial and final states are analogous to the ones involved in $0\nu\beta\beta$ decays. However, this is not an easy task: a DCE event is more probable than a $0\nu\beta\beta$ decay, but it is itself quite rare with respect to competing processes; moreover, a considerable amount of data needs to be collected to have a good statistics. For these reasons, NUMEN will use intense ion beams of tens of μA, which will react with targets made of special isotopes of different materials. Such targets will be shaped as thin foils to preserve the resolution in the energy measurements. But from the combination of these two factors, a new problem arises: due to the energy deposited by the beam in the targets, the latter undergoes a strong thermal stress, eventually being irredeemably damaged.

The aim of the work presented in this thesis is to provide a possible solution to such problem, producing thin targets resistant to intense ion beams. In order to mitigate the excessive temperature rise, in addition to a cryogenic cooler, the targets can be deposited on a high-thermally conductive substrate, whose contribution had, however, to be evaluated. For this purpose a code written in MatLab language has been developed; the code is able to track the temper-

ature evolution in nanoseconds steps, up to the steady state regime for the target/substrate system. Also the software COMSOL has been used, in order to analyze the contribution of the sample holder, taking advantage of the 3D model analysis. Both of the programs proved the solution to be suitable.
Pyrolytic graphite has been chosen as substrate, for its outstanding thermal and mechanical properties. The films, deposited by Electron Beam Deposition, must meet demanding requirements about homogeneity, both in density and thickness. Hence, the produced targets were thoroughly analyzed with a Field Emission Scanning Electron Microscope, until satisfactory results were achieved.
Finally, using a LASER and ion beams as heat sources, the targets thermal behavior has been tested. The LASER test was aimed at studying the dissipation capability of the target/graphite system alone; the ion beam test, performed at UNAM, involved a cooling system in a vacuum chamber and aimed at studying the target/graphite/sample holder system. For both of the tests, results were in good agreement with expected data.

CONTENTS

1

INTRODUCTION

The scientific research aimed to unveil the basic structure of the universe led to the idea that everything is composed by unsplittable, fundamental entities called Elementary Particles. Those particles and their mutual interactions are described by the Standard Model, a quantum field theory which is able to successfully predict and describe all the known elementary particles and three of the four fundamental forces existing in nature. The basis of the Standard Model were laid in the '70s and since then it proved to be a robust theory multiple times, the last of which with the discovery of the Higgs Boson [1]. Depending on whether their spin is integer or half-integer, the particles described in the Model are grouped in Bosons and Fermions. The vectors of strong, electromagnetic, and weak force (namely gluons, photons, W and Z) and the Higgs Boson belong to the former group, while the actual constituents of matter and anti-matter, quarks and leptons, to the latter. Quarks and leptons are classified into three generations, shown in figure 1; the first generation particles, namely up and down quarks, electron and electron neutrino, compose the major part of the known matter in the universe. Quarks and leptons belonging to higher generations are unstable and eventually decay into the first generation particles.

Despite the unquestionable successes achieved in more than 40 years, the Standard Model has some great intrinsic limitations. As already mentioned, gravity is not accounted in the model because a gravity quantum field theory is still missing. Gravity is accurately described by General Relativity, which is a suitable instrument for large objects but not so easy to couple with the microscopic world of quantum mechanics. Only special relativity fits into the Standard Model, nevertheless the model holds because the effect of gravity at such small scale is negligible. Dark matter and dark energy are also not part of the picture, despite accounting for 95% of the entire universe.
Some issues arise even within the boundaries of the SM, e.g. regarding one of its most elusive particle, namely the neutrino. In the SM all of the three flavors (electron, muon, and tau) are supposed to be massless, yet in 1998 atmospheric neutrinos oscillations were detected [2], proving that neutrinos have mass, as supposed by Pontecorvo [3, 4]. Such groundbreaking discovery, awarded with

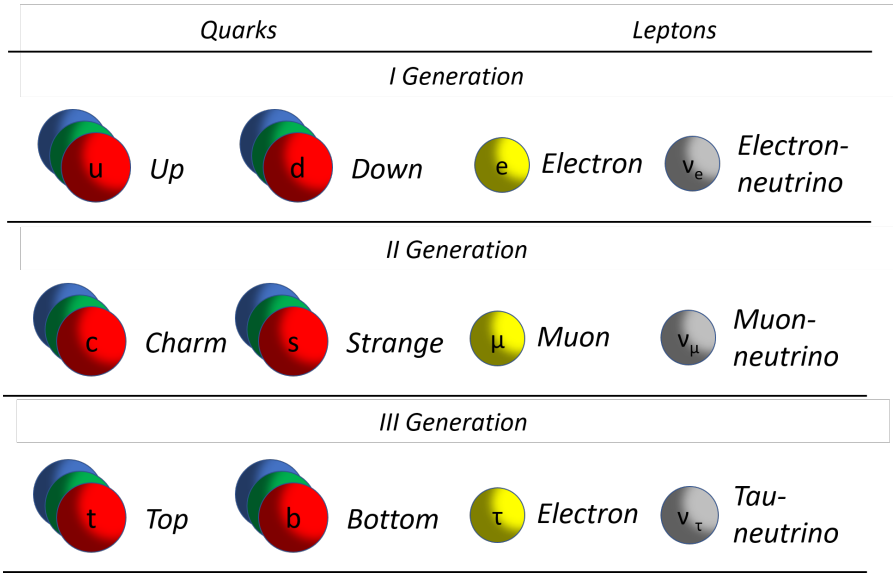

Figure 1: *The three generations of quarks and leptons.*

two Nobel Prizes, was of fundamental importance in deepen our knowledge about neutrinos, but also pointed out another great limit of the SM. Nowadays, several laboratories around the world are working on determining whether the neutrino is a Majorana particle, that is proving if the neutrino is its own antiparticle. The efforts and the resources necessary for these experiments are enourmous, as much as the complexity of the task. A complexity which was always present, since when Dirac theorized the existence of the particle.

1.1 THE BIRTH OF NUCLEAR PHYSICS

In the late XIXth century most part of the periodic table was known, although scientists had very little knowledge of the actual constituents of the atoms. Thanks to studies on ioninzed gases (in 1886, by Goldstein) and the discovery of the electron (in 1897, by Thomson), they knew that atoms had positive and negative parts. On such basis, Thomson proposed an atomic model in which the electrons were embedded in a positively charged matrix, the so called "plum pudding model".
But it was thank to the work of Henri Becquerel that a major breakthrough was achieved. In 1896, he discovered that some elements spontaneusly decay into others: he discovered radioactivity. Conventionally, that year is set to be the begin of nuclear physics. Soon α, β and γ decays were discerned, due to

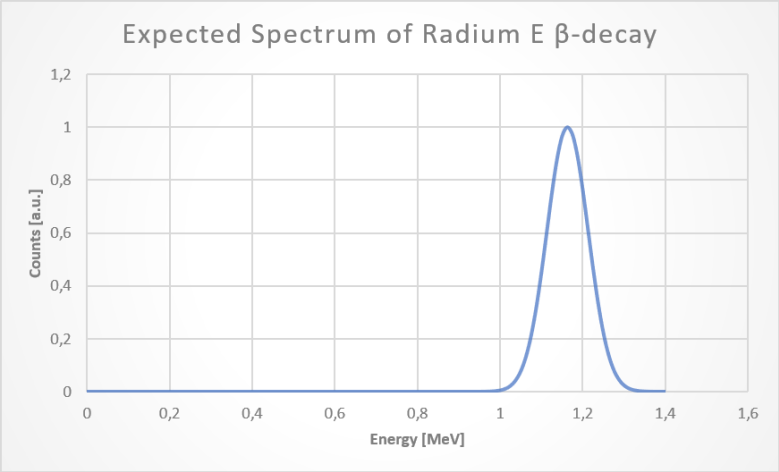

Figure 2: *Energy spectrum expected by Hahn and Meitner for the β-decay of the Radium E, historical name of the ^{210}Bi.*

their different behaviour in the presence of a magnetic or electric field. Initially they were though of as brand new particles and the alphabetical classification was given based on the penetration depth achieved by each one of them. The α-decay in particular was fundamental in the discovery of the atomic nucleus in 1911: it allowed Rutherford to perform the famous experiment in which he bombarded a thin gold foil with α particles. Later on it became clear that the α particle was nothing more that a ^{4}He nucleus, the β one was indeed an electron and the γ ray was just a very energetic photon coming from the relaxation of an excited nucleus.
The theory for the α-decay was developed in 1928 by Gamow, which used the principles of quantum mechanics to explain that the alpha particle, trapped in the potential well of the nucleus, could escape thank to the tunnel effect. It was also observed that an α particle produced in the decay of a certain nucleus has always the same energy; the process involves only the decayed nucleus and the particle, and since the momentum must be conserved, for a given reaction the kinetic energy of the products is fixed. Such energy is always equal to the mass difference between the initial and final state.
Hahn and Meitner expected a similar behaviour for the β-decay, believeing that measurements of β particles energies would give a spectrum analogous to an α-decay one.

Experiments proved them wrong: the energy of the emitted electrons was not centered around a sharp peak, instead several peaks were detected. Initially, the spiked spectrum was attributed to the presence of different elements

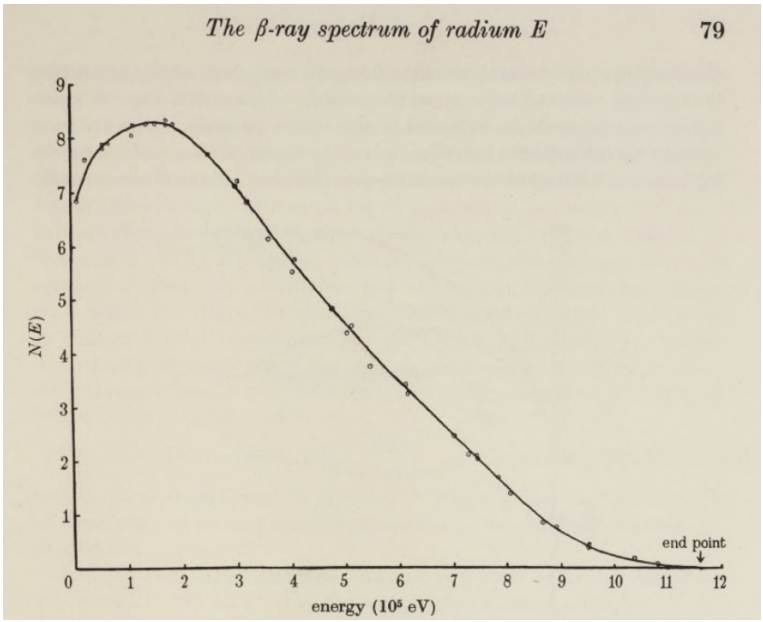

Figure 3: *energy spectrum of the ^{210}Bi decay, historically known as Radium E, acquired by Neary.*

in the emitter, sticking to the idea that a homogeneus substance would emit a β particle of defined energy [5]. In the following years more precise instruments were developed, showing that the energy spectrum of a β-decay is in fact continuous, as showed in figure 3 [6]. The energy difference between the initial and final states (reported in figure 2 for the ^{210}Bi decay) only gives the maximum energy achievable by the electron. Such energy is maximized if both the initial and final nuclei are in the ground state, and decreases if the daughter nucleus is in some excited state. However, the spectrum would only be shifted toward lower energies, but the shape would remain unaffected.

This unexpected outcome puzzled physicists for three decades and even led some of them to question the validity of the law of conservation of energy. More subtle but equally important is the apparent violation of the conservation of angular momentum. The nuclear spin is related to the mass number A of the nucleus: it's integer if A is even, half-integer if A is odd. Since A is unchanged in a β-decay, the spin variation must be integer; but the emitted electron only carries an half-integer spin. Either the conservation laws are wrong, or something crucial is missing in the picture.

The turning point arrived in 1930, when Pauli proposed the existence of a *neutron*, a neutral particle with small or zero mass, hosted inside the nucleus and

expelled along the electron in the decay. The involvement of a third particle provided an intuitive solution to both of the conservation problems.
The concept of neutron was not entirely new; physicists knew that the nucleus contained some sort of electrically neutral particle, since the masses of protons and electrons alone didn't suffice to reach the mass of a nucleus. The gap was filled in 1931 by Chadwick, who discovered that nuclei contained a neutral particle massive nearly as much as a proton: he called it *neutron*, like Pauli did for the β-decay particle. Edoardo Amaldi, a friend of Enrico Fermi and member of his research group, jokingly renamed the latter *neutrino* because of its small (or maybe null) mass. Such name, meaning "little neutral one" in Italian, was thereafter kept.

It took almost 40 years and a vast number of discoveries and theories to arrive at the concept of neutrino. However, such particle was not predicted or expected to exists, but rather suggested by the great discrepancy between expectation and results in β-decay experiments. The actual mechanism of the decay was still largely unknown and many questions remained unanswered. No one was certain whether the neutrino and the electron were already in the nucleus before the decay, or, if not, from where did they come from.

1.2 FERMI THEORY OF β-DECAY

The italian contribution to the newborn field came from a proficient group of young scientists, whose leader was Enrico Fermi; the group was specialized in nuclear and molecular spectroscopy, but it was also involved in artificial radioactivity. Fermi curated the theoretical aspects of the research, while simultaneously authoring several important works by himself, one of which was his groundbreaking "Tentativo di una teoria dei raggi β" (Tentative for a β-rays theory), published in 1933 [7]. Initially refused by the famous journal Nature for being too far fetched, hence for decades available only in italian and german, the paper was instead pioneering.
The work is based on three fundamental hypothesis. In the first, Fermi vigorously rejected the speculations about the existence of nuclear electrons, supposedly contained inside the nucleus and emitted in the decay. In fact, according to basic principles of quantum mechanics, no orbit could possibly exist so close to the nucleus. Fermi hypothesized that the electron and the neutrino seen in a β-decay were indeed created in the process, as much as a photon is created when an electron goes in a lower atomic orbital. Hence, the total number of

electrons and neutrinos is not strictly constant.
In the second, according to an idea of Heisenberg, the proton and the neutron are seen as different states of the same particle having value 1/2 of a new quantum number called isospin. This variable is dicotomic and proton differ from neutron by the value of the third component, respectively 1/2 and -1/2.
The last hypothesis concerns the choice of a suitable hamiltonian for heavy and light particles alike, so that when a neutron decays into a proton, an electron and a neutrino are created, thus conserving the total charge. The opposite transition from a proton to a neutron must be valid as well.
The core of the Fermi's theory is his famous Golden Rule, which states that the transition probability density λ between two states depends on the density of final states:

$$\lambda = \frac{8\pi^3 g_F^2}{\bar{h}^4 c^3} |V_{fi}|^2 \bar{\psi}_s \psi_s (W - H_s)^2 \tag{1}$$

being g_F the interaction coupling constant, V_{fi} the nuclear matrix element, H_s the total energy of the electron and W the energy difference between the neutron and the proton. Such energy difference must be greater or at least equal to the sum of the masses of the electron and the neutrino:

$$W \geq (m + \mu)c^2$$

Fermi found that the spectrum of a β-decay could be reproduced quite accurately if the neutrino had no mass, or at most a very small one. The precise value of the matrix elements were not known at Fermi's time, as well as the actual mechanism of the decay.
However, Fermi was able to perform some numerical evaluation of the formulae he calculated (see figure 4), showing that the shape of the most well-known β emitters spectra (in figure 5 are reported those collected by Sargent [8]) could be reproduced quite accurately. The discrepancy between theory and experiment can be addressed to fluctuations in the matrix element value, to unaccounted Coulomb interactions, and to experimental errors.

For his calculations, Fermi used a matrix element value which did not affect the shape of the spectrum, the so-called *allowed approximation*. In this picture the potential of the decay is approximated as a δ-function centered around the decay point. Then, the values of the matrix elements are non vanishing only if the initial and final nuclear wavefunctions have the same parity. The electron and the neutrino are assumed to be non-interacting right after the decay; their

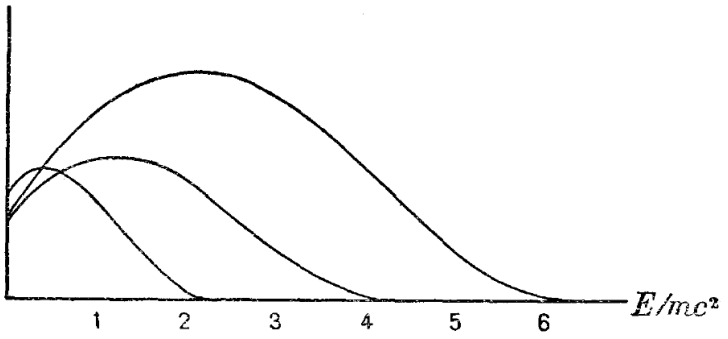

Figure 4: *spectra evaluated by Fermi for different maximum energies of the β particle.*

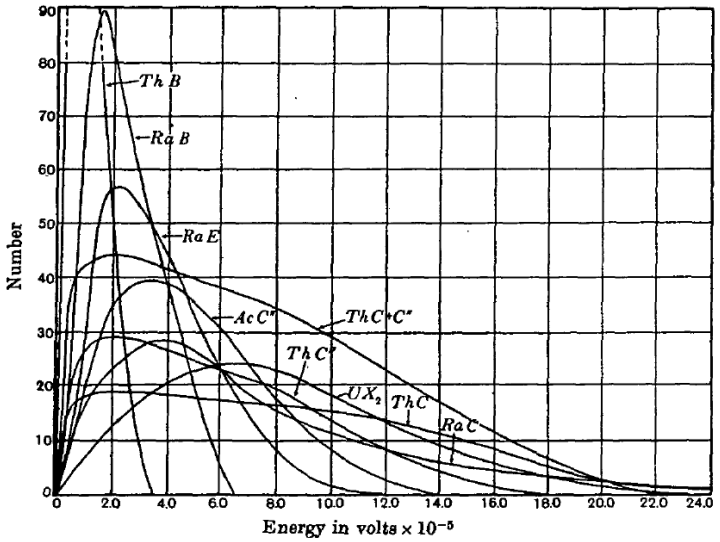

Figure 5: *experimental curves of the 8 most used elements for β-decay studies, collected by Sargent.*

wavefunction can be therefore represented as a plane wave. Taking into account that both the neutrino and electron wavenumbers are very small, Fermi considered only the first term of the series expansion, which is the constant g_F of equation 1.
Fermi's theory was extended by Gamow and Teller to take into account the electromagnetic interaction between the leptons and the nucleus. A term including the total spin momentum of the leptons was added to the Fermi's local potential. This term is proportional to $\sigma \cdot s_L$, being s_L the total spin momentum of the leptons and σ the spin operator of the nucleus. Due to its axial properties, the term s_L has parity $(+)$; therefore, the initial and final states must have the same parity to have a non vanishing matrix element. Hence, the parity does not change in both of the model. The parity is related to the orbital angular momentum ℓ through the relation $(-1)^\ell$, and since in these models the parity does not change, the variation of ℓ must be zero. This means that, according to angular momentum conservation law, a change in the total spin of the nucleus ΔI can only be addressed to the orientation of the spins of the leptons, namely s_ν and s_e. If they are antiparallel, then:

$$S = s_\nu + s_e = 0; \quad \Delta I = 0$$

The potential term added by Gamow and Teller, $\sigma \cdot s_\ell$, vanishes, and the model return to be the one used by Fermi. This kind of event is in fact known as Fermi decay. If, conversely, the spins are parallel:

$$S = s_\nu + s_e = \pm 1; \quad \Delta I = \pm 1$$

The term added by Gamow and Teller does not vanish and the total spin of the nucleus changes accordingly; this event is known as Gamow-Teller decay. A change of the total spin of the nucleus equal to $\Delta I = 0, 1$ associated with a conservation of parity define the selection rule for allowed decays, which reads:

$$\Delta I = 0, 1; \quad \Delta \pi = no$$

Being π the parity.
Fermi results were in good agreement for nuclei which decay through allowed transitions, but forbidden decays could not be correctly predicted. The latter are not *stricktly* forbidden, but the transition probability decreases as the grade of forbidness increases. When the orbital angular momentum is not zero, both parity and total angular momentum change accordingly, and the complexity of V_{fi} increases. Each value of the matrix must be measured experimentally

to correctly reproduce the spectrum, which can be quite difficult for highly forbidden decays; in fact, each degree of forbidness decreases the transition probability by a factor $\propto 10^{-4}$ [9].
The first experimental confirmation of the theory arrived in 1956, roughly 20 years after Fermi's paper, when Cowan detected the neutrino [10]; the discovery confirmed Pauli hypothesis of the third light particle involved in the β-decay. During the same period physicists began to theorize how the decay actually occurred, an effort which culminated, in 1968, with the electroweak theory [11]. The theory identifies the responsibles of the interaction between hadrons and leptons in the W^+, W^- and Z^0 bosons, the vectors of the weak force. For their discovery it was necessary to build particle accelerators able to reach the necessary high energies, a task which took more than a decade to be fullfilled. In 1976 the Super Proton Synchrotron (SPS) was built at CERN and thanks to it, in 1983, Rubbia and Van der Meer found the vectors of the weak force [12].

1.3 THE DOUBLE β-DECAY

Schematically, β^- and β^+ decays of a nucleus with A nucleons and Z protons can be represented respectively by formulae 2a and 2b:

$$ {}^{A}_{Z}\mathrm{X} \rightarrow {}^{A}_{Z+1}\mathrm{Y} + e^- + \bar{\nu}_e \tag{2a} $$

$$ {}^{A}_{Z}\mathrm{X} \rightarrow {}^{A}_{Z-1}\mathrm{Y} + e^+ + \nu_e \tag{2b} $$

while the weak process itself can be represented with a Feynman diagram (fig. 6), in which the conversion of a down quark in an up quark through the emission of a W^- boson is explicitly shown.

As already said, the parent nucleus cannot decay β if its isobars with $Z = Z_{parent} \pm 1$ have a lower binding energy; however, the energy difference with the isobars with $Z = Z_{parent} \pm 2$ may be sufficient to make the parent nucleus β-decay twice, event which is called double β-decay ($2\nu\beta\beta$). Such condition is more likely to occur in even-even nuclei, where a single β-decay is strictly forbidden or strongly suppressed. In an ordinary double β-decay , two β particles and the two corresponding neutrinos/anti-neutrinos are emitted (formulae 3a and 3b).

$$ {}^{A}_{Z}\mathrm{X} \rightarrow {}^{A}_{Z+2}\mathrm{Y} + 2e^- + 2\bar{\nu}_e \tag{3a} $$

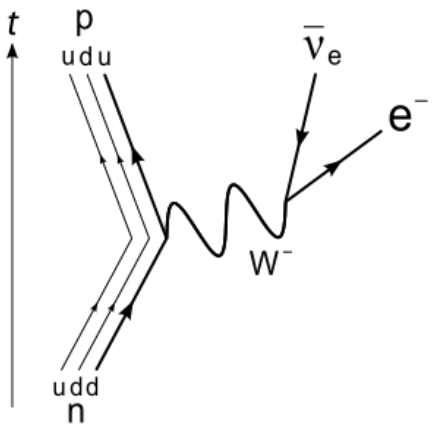

Figure 6: *Feynman diagram of a β^- decay of a neutron.*

$$ {}^{A}_{Z}\mathrm{X} \rightarrow {}_{Z-2}{}^{A}\mathrm{Y} + 2e^+ + 2\nu_e \tag{3b} $$

The corresponding Feynman diagram for a $\beta^-\beta^-$ decay event is the one reported in figure 7.

A $2\nu\beta\beta$ process satisfies all of the conservation laws of the Standard Model. It can be seen as two single β-decays occurring simulaneously and the energy spectrum is in fact similar. Although the half-life of a $2\nu\beta\beta$ decay is rather long and can exceed 10^{20} years, such decays have been observed several times, the first of which in 1987, using ^{82}Se as isotope [13].
However, if neutrino were not a Dirac particle, but instead a Majorana one, there would be another way for the decay to occur. Majorana made the hypothesis of the double nature particle-antiparticle of the neutrino, i.e. the neutrino is antiparticle of itself. Let's first observe that:

a) a beta decay occurs as in equation 2a or 2b;

b) a beta emission can occur after absorption of a neutrino in a nucleus, as in equation 4b;

Under this assumption, the neutrino of equation 4b could be the antineutrino of the decay reported in equation 4a. This mechanism was thought by Racah [14], who schematized the process as occuring in two steps:

$$ (Z, A) \rightarrow (Z+1, A) + e^- + \bar{\nu}_e \tag{4a} $$

$$ (Z+1, A) + \nu_e \rightarrow (Z+2, A) + e^- \tag{4b} $$

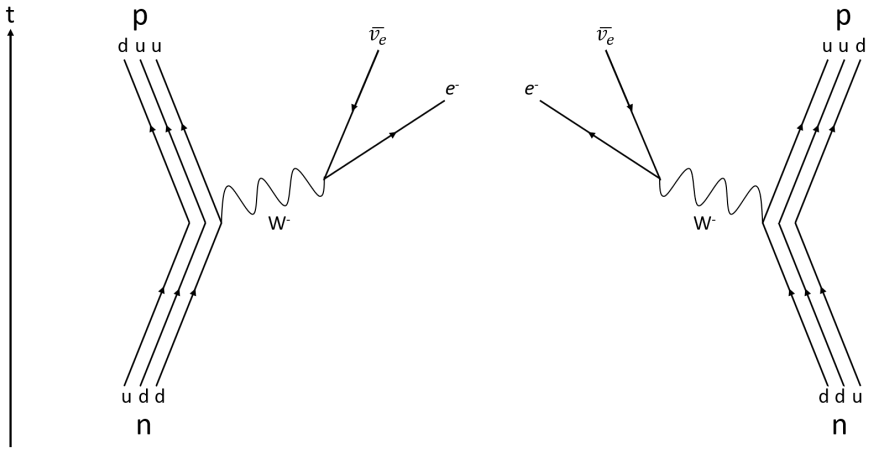

Figure 7: *Feynman diagram of a double β^- decay, in which 2 electrons and 2 neutrinos are generated.*

Formula 4a describes the beta decay of a neutron, while equation 4b describes the absorption of the emitted antineutrino (now operating as neutrino in the Majorana hypothesis) by another neutron of the same nucleus. In the first reaction, a neutron decays β^-, emitting an antineutrino which is subsequently captured by another neutron of the nucleus. Since a neutrino is emitted and one is absorbed, the net amount of neutrinos is zero:

$$(Z, A) \rightarrow (Z + 2, A) + 2e^- \tag{5}$$

It is worth noticing that this chain can occur only if the neutrino behaves as described by Majorana itself [15], otherwise the second step would be impossible. A striking characteristic of $0\nu\beta\beta$ decay is the violation of the lepton number conservation, which changes from 0 to 2. This is forbidden in the Standard Model, and in fact the theory describing the process falls within the "Physics Beyond the Standard Model".
The lepton number violation (LNV) would have a great impact on current theories, but the observation of a $0\nu\beta\beta$ event would have other implications. It would help in establishing the effective neutrino mass [16], due to the inverse proportionality of the latter with the half-life of the process; also, combining the lepton number violation and the CP violation, a possible explanation may be found for the difference in barionic matter and antimatter in the universe, namely the leptogenesis [17].
Several experiments are currently involved in the detection of $0\nu\beta\beta$ decay [18], but such experiments are of exceptional difficulty, for both experimental and

theoretical reasons. Due to the extremely long half-life (about 10^{24} years), few events are expected to be detected, hence the necessity to remove all the sources of background events. The simplest way of detecting the decay is collecting the two electrons created in the process, whose summed energies correspond to the Q-value of the reaction. This signal however must be discerned by the far more numerous processes which emit a single electron or from the continuous background of β or $2\nu\beta\beta$ decays. The experiments must be performed deep underground to limit the noise coming from cosmic radiation, but the radiation coming from the underground long lived isotopes (^{232}Th, ^{238}U,...) must be effectively shielded as well.
Experiments investigating $0\nu\beta\beta$ use particular isotopes in which single β decay is strongly suppressed or forbidden,so that the $\beta\beta$-decay is the most probable decay. Albeit being the most likely decay path, the expected $0\nu\beta\beta$ half-life remains greater than $\sim 10^{24}$ years. The exact value, or even the actual order of magnitude, is something still under study. Predictions cannot be very accurate, since the factors contributing to the calculation of the half-life are not precisely known. The half-life can be expressed as:

$$[T^{0\nu}_{1/2}]^{-1} = G_{0\nu}|M^{0\nu}|^2\langle m_{\beta\beta}\rangle^2 \tag{6}$$

Where $G_{0\nu}$ is the phase-space factor for the two emitted electrons, $M^{0\nu}$ is the Nuclear Matrix Element (NME), and $\langle m_{\beta\beta}\rangle$ is the effective Majorana mass for the electron neutrino [19]. The $G_{0\nu}$ factor can be calculated quite accurately, thanks to precise measurements of the Q-value of the decays [20, 21], while the other two quantities are more difficult to evaluate. The calculated values of the NMEs strongly depends on the calculation method and the $\langle m_{\beta\beta}\rangle$ term depends on the relative difference of the neutrinos masses:

$$\langle m_{\beta\beta}\rangle = \sum_k U^2_{ek} m_k \tag{7}$$

m_k are the masses of the respective neutrino flavours and U_{ek} are the Pontecorvo–Maki–Nakagawa–Sakata matrix elements for the electron neutrino. Even though the values of the single masses are not precisely know, the limit value of their sum has been evaluated quite precisely [22]. In the end, the major source of uncertainty are the NMEs of the decay, which are intrinsically difficult to measure due to the rarity of the process itself. But there is a way to obtain such information, which inspired the NUMEN project.

2

THE NUMEN PROJECT

As already said previously, in the $0\nu\beta\beta$ half-life formula the NME factor is the most affected by uncertainties. This is due mainly to the model used for the calculation, since each method uses different approaches, but also to the non-trivial task of solving a complex nuclear multi-body problem. In addition, there is a severe lack of experimental data to test the validity of the theoretical results. Several other reactions, like Single Charge Exchange or transfer reactions [23, 24], are used to constrain the calculations, but such constraints are not stringent. The fundamental idea of the NUclear Matrix Elements for Neutrinoless double beta decay project (NUMEN) [25] is to measure the cross-sections of Double Charge Exchange (DCE) reactions, whose initial and final states are equal to those of a $0\nu\beta\beta$ event. Even though a $0\nu\beta\beta$ decay involves weak processes and DCE likely proceeds through strong interaction, the NME of the two processes are closely related. To name just a few shared characteristics, a part from initial and final states, the two processes share, in transition operators, the same Fermi, Gamow-Teller and rank-2 tensor components and the non-locality nature of the processes [26, 27].
The NUMEN project unfolds in 4 phases, each of which is propaedeutic for the following one and serves to gain specific information and knowledge. Phase one, ran in 2013, served mainly for proving the feasibility of the idea, using the reaction ^{40}Ca (^{18}O,^{18}Ne) ^{40}Ar as benchmark. Phase two, which is currently running, is providing preliminary information about the isotopes which will be used in the following phases. Phase three will concern the upgrade of the LNS facility, while the phase four will study a number of different isotopes in the upgraded facility.
Several isotopes which are going to be studied in NUMEN are also used in the experiments involved in the $0\nu\beta\beta$ search, such as the ^{130}Te in CUORE [28] or the ^{76}Ge in GERDA [29]. The isotopes used in the phase two of NUMEN are ^{116}Sn, ^{76}Se, ^{116}Cd, ^{76}Ge, ^{130}Te. The first two elements will be irradiated with an ^{18}O beam, while for the remaining elements a ^{20}Ne beam will be used. The occurring DCE reactions are listed in table 1.

The list of the isotopes which are planned to be used is longer, even though still not conclusive, and includes ^{100}Mo, ^{96}Zr, ^{150}Nd, ^{160}Gd, ^{198}Pt among the others. The complete list can be found in reference [25].

List of DCE reactions in NUMEN
^{116}Sn (^{18}O,^{18}Ne) ^{116}Cd
^{76}Se (^{18}O,^{18}Ne) ^{76}Ge
^{76}Ge (^{20}Ne,^{20}O) ^{76}Se
^{116}Cd (^{20}Ne,^{20}O) ^{116}Sn
^{130}Te (^{20}Ne,^{20}O) ^{130}Xe

Table 1: *List of the isotopes which are going to be used in the second phase of NUMEN, showed with the respective ion beam.*

The NUMEN project is hosted at the Laboratori Nazionali del Sud of the Istituto Nazionale di Fisica Nucleare (LNS - INFN), where are located the most important equipment necessary to the experiment: the Superconducting Cyclotron K800 and the MAGNEX spectrometer.

Figure 8: *The MAGNEX spectrometer. From the lefthand side, one can see the scattering chamber, the quadrupole (in red) and the dipole (in blue).*

The K800 SC is able to accelerate a wide range of ion beams, from protons to uranium, with maximum beam currents of some tens of nA and energies up to 80 MeV/u for the lightest species. Concerning MAGNEX, it is a spectrometer designed specifically to investigate low yields phenomena. For this purpose, it has a large acceptance both in solid angle (50 msr) and impulse ($-14\% < \delta p/p < +10.3\%$), characteristic of great importance for measuring cross sections at wide angles and different energies; the apparatus is suitable for the identification of heavy ions ($\delta A/A \sim 1/160$), with a resolution in energy of about $\delta E/E \sim 1/1000$ [30].

These two apparatuses are currently able to acquire valuable information about the investigated phenomena, but the maximum beam current delivered by the accelerator and the acceptance rate of the spectrometer do not fully match the NUMEN requirements.

2.1 SC AND MAGNEX UPGRADE

A DCE event is not as rare as a $0\nu\beta\beta$, but still the expected order of magnitude of the cross section is few hundreds of nb/sr [31]. The precise measurement of a cross section requires the meeting of some conditions. To name but a few, it is mandatory to have a significant statistics, which means:

a) collecting a large amount of data;

b) having an hardware able to collect and discern the events of interest;

c) reducing the errors as much as possible.

To this end, the LNS facility, particularly the SC and MAGNEX, will undergo an important upgrade to boost the performances of the equipment, making it up-to-date for the requirements of modern nuclear and particle physics experiments.
In fact, the number of produced events depends, not uniquely, on the maximum beam current delivered by the particle accelerator. The upgraded SC will be able to produce ion beams with intensity up to 50 μA and energies between $15 - 70$ MeV/u [32]. Quite predictably, this upgrade does not come without drawbacks. The performance of the quadrupole and the dipole of the MAGNEX spectrometer have to be enhanced as well, to increase the acceptance in energy; the radiation hardness of the Si detectors must be increased, since the much higher flux would deteriorate them at an unacceptable rate; a suitable beam dump must be built, in order to safely stop such a strong beam and avoid activation issues.
Another disadvantage of a ten-thousand fold increase of the maximum beam current is the huge thermal stress at which the target is forced. The obvious solution of cooling it down must however couple with a number of constrains, which make the task not trivial to solve.

2.2 THE NUMEN TARGET

In the first and second phase of NUMEN, targets are shaped as thin foils of about 1 μm in thickness, supported by a carbon film some tens of nanometers in thickness. The metal frame hosts several targets, some of which are used to calibrate the beam. The target of choice can be remotely selected by using a vertical-shifter motor, without the need of opening the chamber.

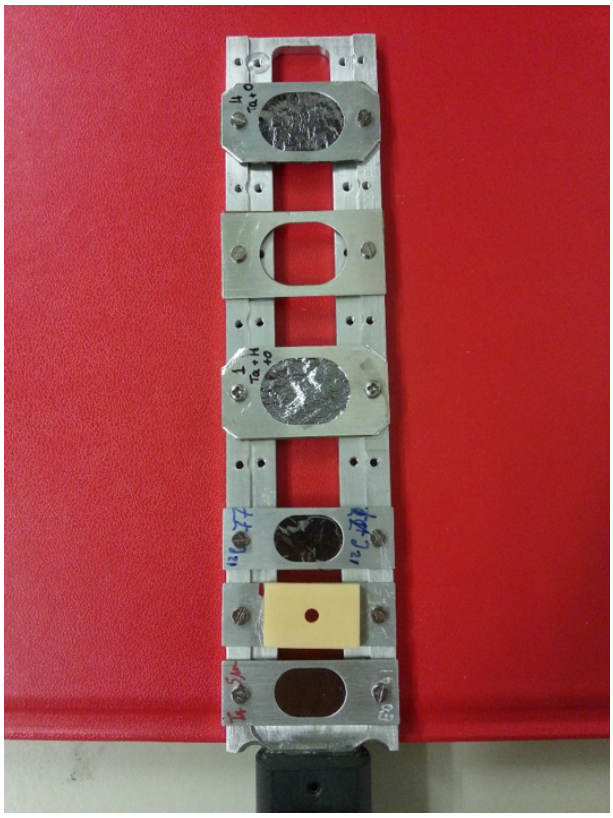

Figure 9: *Target used in phases one and two. Materials are deposited on a thin carbon film and held in position by a metal frame. The bottom targets are used for calibration purposes.*

The metal frame is connected only to the motor and does not provide any cooling to the targets, since the beam deposits small amounts of heat.
When a charged particle crosses an object, it deposits a certain amount of energy, mainly by ionization processes. The formula to evaluate the average energy loss per unit path is the Bethe-Bloch formula:

$$-\frac{dE}{dx} = 4\pi N_A r_e^2 m_e c^2 z^2 \rho \frac{Z}{A}\frac{1}{\beta^2}\left(\ln\frac{2m_e c^2\gamma^2\beta^2}{I} - \beta^2 - \frac{\delta}{2}\right) \tag{8}$$

Where $4\pi N_A r_e^2 m_e c^2$ are constants, namely the Avogadro number, the classical electron radius and mass and the speed of light, the product of which is equal to 0.3071 [MeV/(g/cm^2)]; z is the charge of the incident particle; ρ, Z, A and I are respectively the density, the atomic and mass number and the ionization potential of the target material; lastly, δ is a term related to the shielding of the projectile electric field due to the polarization of the medium [33].
The charge of the incident particle has a strong influence on the amount of deposited energy. Since equation 8 refers to a single particle, the deposited energy increases linearly with the beam intensity, e.g. with the number of particles per second.
The intensity of the beam in phases one and two of the project is about 10 nA and the average deposited power in the targets is below 1 W. Thus, a dedicated cooling system is not required, because the target frame is sufficient to dissipate the generated heat. However, with such a limited beam the number of reactions is fairly low and few interesting events can be collected. To increase the statistics, one could think of increasing the thickness of the target, but the related errors would increase as well, cancelling the benefits. The error sources which limit the target thickness will be described in the next section.

2.3 ENERGY RESOLUTION EVALUATION

Knowing the beam energy, the measured quantities are the energy and the direction of the product exiting the target. The final value of the energy is affected by several factors; the ones which depend on the target are the dispersion, the straggling and the non uniformity of the target surface.
The dispersion error is due to the uncertainty on the position at which the DCE reaction occurs: such position cannot be known, because no detector can measure it. Since the DCE reaction changes the product atomic number by 2 units, the point at which the reaction occurs strongly influences the product final energy.
This latter is also affected by the straggling, a statistical effect which accounts for the fluctuation of the single particle energy loss around the average and for random Coulomb collisions between the incident particles and the nuclei of the target.
Both of the aforementioned error sources are worsen if the target thickness is

not uniform, a condition far from being unlikely. The non uniformity further spreads the energy distribution coming from the dispersion and the straggling. The other main sources of error are directly ascribable to the equipment. In fact, both the SC and MAGNEX introduce an error on the order of 0.1% of the particles energy (these values should remain unchanged after the upgrade).
For each target, the resolution of the energy measurement must be sufficient to distinguish between the ground state and the first excited level of the daughter nucleus. The total resolution can be obtained summing in quadrature the various contributions:

$$\Delta E_{Resolution} = \sqrt{\Delta E_{Target}^2 + \Delta E_{MAGNEX}^2 + \Delta E_{SC}^2} \tag{9}$$

Being $\Delta E_{Resolution}$ the FWHM of the energy distribution and ΔE_{Target}, ΔE_{MAGNEX}, ΔE_{SC} the FWHM of the error distribution due to the target, MAGNEX and the cyclotron, respectively.
The error introduced by the dispersion, the straggling and the thickness non uniformity are statistical; therefore, in order to evaluate them, a Monte Carlo code has been written in MatLab environment. The code works as follows.
The target is supposed to have a gaussian distribution of the thickness roughness around its average value, with standard deviation σ_{Target}. For each incoming ion, a number is randomly sorted following a gaussian distribution and then added (or subtracted) to the target average thickness. The resulting gaussian distribution has a standard deviation equal to σ_{Target}. Afterward, the DCE reaction point is randomly sorted within the new thickness. Since the cross section does not depend on the thickness, the DCE reaction probability is constant throughout the target.
Then, the projectile energy loss and straggling are calculated up to the reaction point. The straggling has been calculated using the Gaussian approximation (equations 10a, 10b, 10c):

$$f(E,x) = \frac{1}{\sqrt{2\pi\sigma^2}} e^{\frac{(E-<E>)^2}{2\sigma^2}} \tag{10a}$$

$$\sigma^2 \equiv \xi \cdot E_{Max}\left(1 - \frac{\beta^2}{2}\right) \tag{10b}$$

$$\xi \equiv \frac{2\pi z^2 e^4 N_A Z \rho x}{m_e c^2 \beta^2 A} \tag{10c}$$

Where the symbols are defined after equation 8 and x is the target thickness.

Before the reaction, the straggling is taken into account by adding or subtracting a gaussianly weighted quantity, sorted randomly, to the average energy loss. The standard deviation of such distribution is calculated by using formula 10b. If the reaction products are in the ground state, as they are considered here, the DCE reaction can be accounted for by considering the conservation of momentum and total energy, together with the change of the projectile atomic number (see appendix A.2). The energy loss and the straggling are then calculated for the remaining portion of the target, now using the ejectile atomic number. The straggling is taken into account as before, by adding a random number with a gaussian weight.
The resolution has been calculated for each target, supposing a σ_{Target} equal to the 6.7% of the average thickness. this value correspond roughly to a maximum non uniformity of $\pm 20\%$ with respect ot the average thickness. Results are shown in figures 10-14, which report the energy resolution of the DCE reaction products. The FWHMs of the energy resolution are reported as a function of the target thickness, for the contributions of target (straggling+dispersion+non uniformity), MAGNEX and SC, together with the total resolution. For thicknesses smaller than about 1 μm, in most of the cases the resolution is sufficient to distinguish the ground state and the first excited level of the daughter nucleus. In the reaction ^{116}Sn(^{18}O,^{18}Ne)^{116}Cd, the limit thickness is slightly higher than about 800 nm.

For most of the targets (^{116}Cd, ^{130}Xe, ^{76}Ge, ^{76}Se) the gap between the ground state and the first excited level is about $500 - 550$ keV [34–36].
The situation is rather different in the ^{116}Cd(^{20}Ne, ^{20}O)^{116}Sn reaction. In ^{116}Sn the gap between the ground state and the first excited level is much wider compared to all other cases. The energy gap of the ^{116}Sn nucleus is so wide, about 1.3MeV, that even using a ^{116}Cd target thicker than 1 μm the total resolution in energy would still be well below the resolution limit. However, there are other limitations to the target thickness, which will be exposed later, in chapter 4.
It is worth noticing that 15 MeV per nucleon is the lowest beam energy used in NUMEN; in this condition, the errors introduced by both the SC and MAGNEX are minimized. Since the error of the two instruments is proportional to the beam energy, at higher energies the loss in resolution due to the target characteristics becomes relatively less important. That said, a target must be build in order to meet the experimental standards in every experimental condition, hence the target uniformity remains a parameter of paramount importance.
As a final remark, it must be kept in mind that these resolutions have been calculated for a certain target non uniformity; the total resolution would of course worsen with a higher thickness inhomogeneity. The above mentioned evalua-

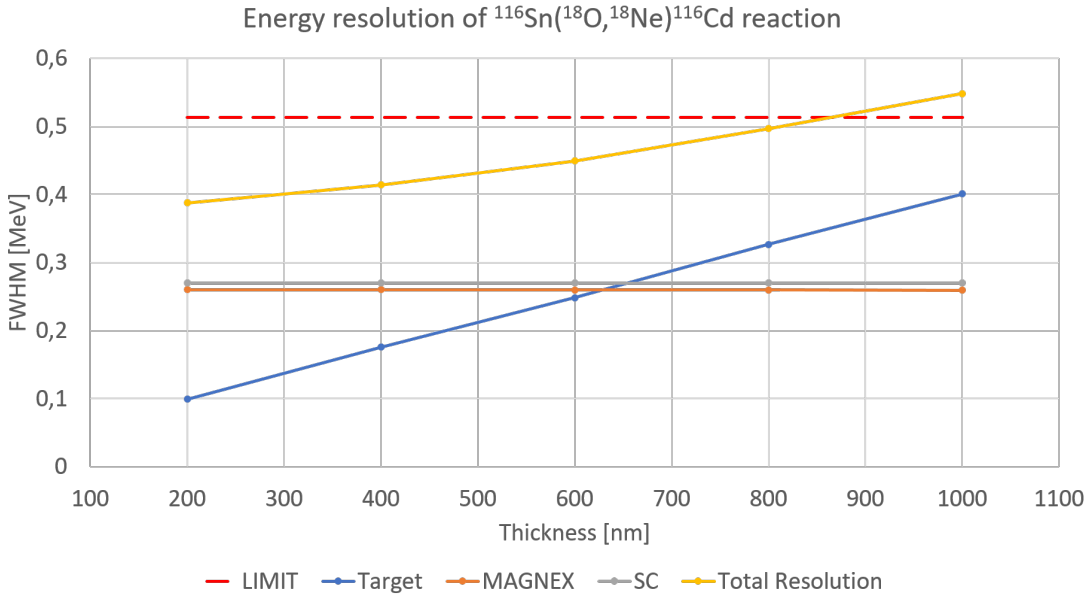

Figure 10: *Energy resolution for a Sn target in the ^{116}Sn(^{18}O,^{18}Ne)^{116}Cd reaction at* 15 *MeV/u, as a function of the target thickness. The dotted red line is the upper limit of the tolerable error. The target non uniformity is supposed gaussian, with a σ_{Target} equal to* 6.7% *of the average thickness.*

tions set the limits at which the target thickness is bound; increasing the beam intensity seems the only viable solution to obtain a much higher statistics, but there are several drawbacks to deal with.

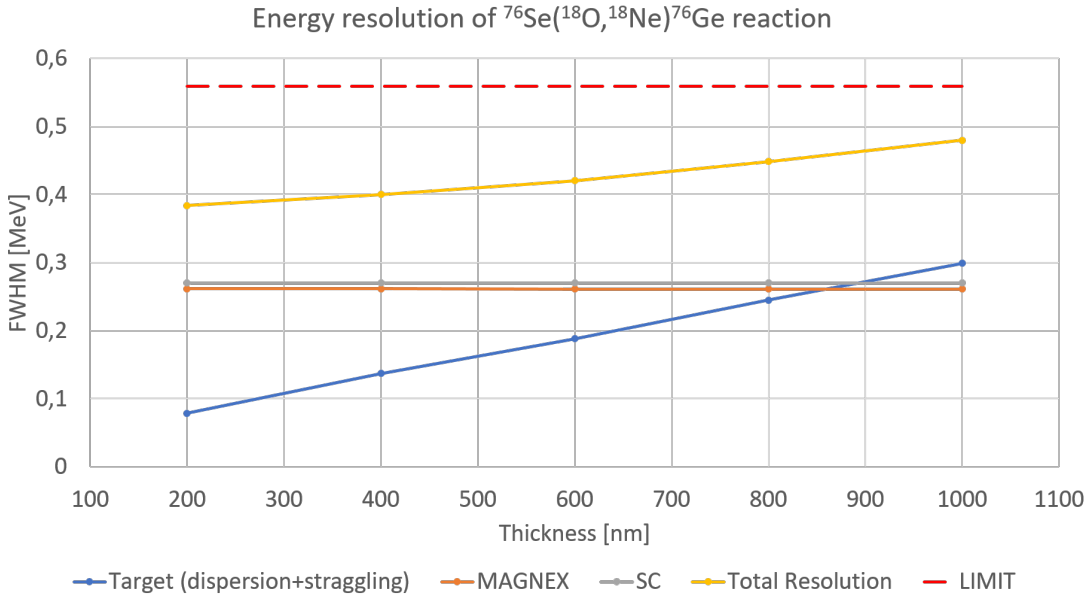

Figure 11: *Energy resolution for a Se target in the $^{76}Se(^{18}O,^{18}Ne)^{76}Ge$ reaction at* 15 *MeV/u, as a function of the target thickness. The dotted red line is the upper limit of the tolerable error. The target non uniformity is supposed gaussian, with a σ_{Target} equal to* 6.7% *of the average thickness.*

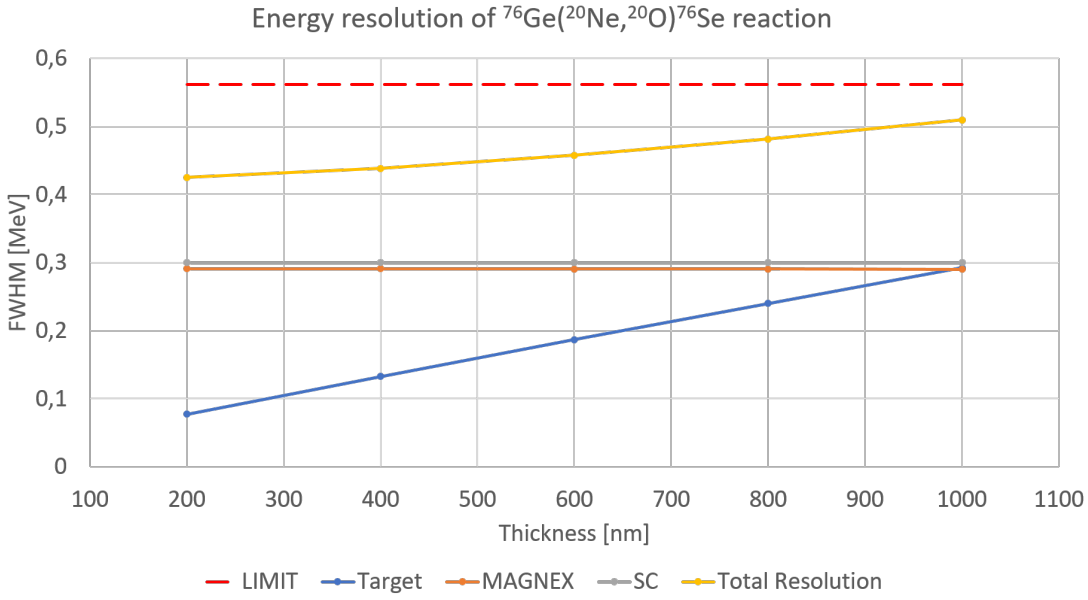

Figure 12: *Energy resolution for a Ge target in the $^{76}Ge(^{20}Ne,^{20}O)^{76}Se$ reaction at* 15 *MeV/u, as a function of the target thickness. The dotted red line is the upper limit of the tolerable error. The target non uniformity is supposed gaussian, with a σ_{Target} equal to* 6.7% *of the average thickness.*

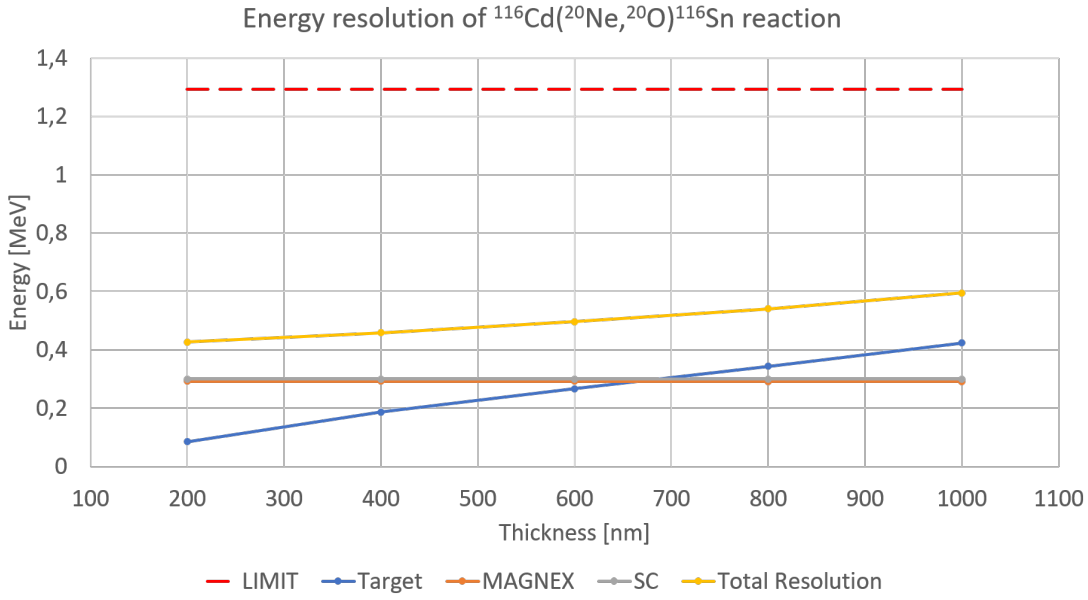

Figure 13: *Energy resolution for a Cd target in the $^{116}Cd(^{20}Ne,^{20}O)^{116}Sn$ reaction at 15 MeV/u, as a function of the target thickness. The dotted red line is the upper limit of the tolerable error The target non uniformity is supposed gaussian, with a σ_{Target} equal to 6.7% of the average thickness.*

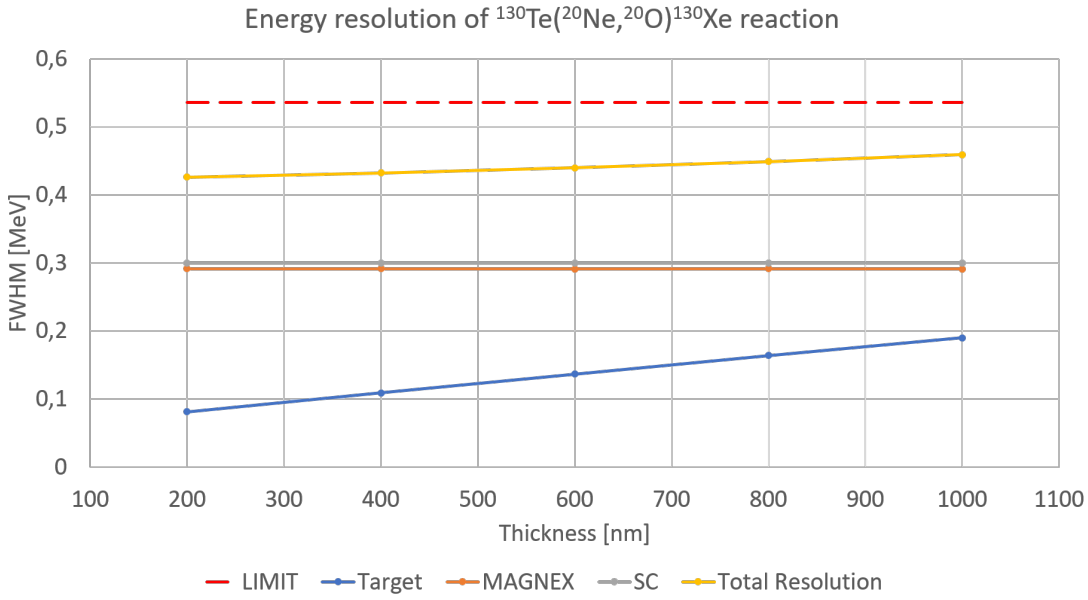

Figure 14: *Energy resolution for a Te target in the $^{130}Te(^{20}Ne,^{20}O)^{130}Xe$ reaction at 15 MeV/u, as a function of the target thickness. The dotted red line is the upper limit of the tolerable error. The target non uniformity is supposed gaussian, with a σ_{Target} equal to 6.7% of the average thickness.*

3

TARGET FOR HIGH INTENSITY BEAMS

A high intensity ion beam must be paired with a suitable equipment in order to be used, both for practical reasons (e.g. collect all the reaction products) and security reasons (e.g. to safely stop the beam in a beam dump). Concerning the target, it must be built to resist the high thermal stress provoked by the beam.
To begin with, one must first evaluate how much heat is produced by the ion beam inside the target.
To this end, the Bethe-Bloch formula (Eq. 8) has been numerically evaluated for each target material, at different projectile energies. Considering the evaluations reported in figures 10 - 14, the study on ^{116}Cd, ^{130}Te, ^{76}Ge, ^{76}Se targets has been performed on a reference thickness of 1 μm. The ^{116}Sn target has been supposed only 800 nm thick, due to resolution limits. The amount of power deposited by a beam with 50 μA of current intensity is reported in table 2.

	Beam Energy [MeV/u]			
	15	30	45	60
Power in ^{116}Sn [W]	4,01	2,39	1,76	1,42
Power in ^{76}Se [W]	3,73	2,2	1,61	1,3
Power in ^{76}Ge [W]	4,9	2,88	2,11	1,7
Power in ^{116}Cd [W]	7,19	4,28	3,15	2,54
Power in ^{130}Te [W]	4,93	2,94	2,17	1,75

Table 2: *Heat deposited in* 1 *µm thick targets (*800 *nm for* ^{116}*Sn), for different beam energies. The beam current is supposed equal to* 50 *µA.*

According to the Bethe-Bloch formula, the energy released in a medium by a charged projectile increases as the energy itself decreases. Consequently, targets are heated more by the low energy beams (i.e. 15 MeV/u) than highly energetic ones.
Once the power deposited by a 50 μA beam has been calculated for each target, one can figure how much power such targets are able to dissipate. All the fol-

lowing calculations has been firstly performed in the worst case scenario, that is considering the heat produced by a 15 MeV/u ion beam.

3.1 OLD TARGETS MAXIMUM RESISTANCE

Evaluating the maximum power dissipated means firstly to find a suitable function of the temperature. To this end, one can use the heat equation, whose steady-state solution can be here found analytically.
The heat equation in cartesian coordinates reads:

$$k_x \frac{\partial^2 T}{\partial x^2} + k_y \frac{\partial^2 T}{\partial y^2} + k_z \frac{\partial^2 T}{\partial z^2} + \frac{dQ}{dtdV} = \rho c \frac{\partial T}{\partial t} \tag{11}$$

Where ρ, c and $k_{x,y,z}$ are respectively the material density, specific heat and thermal conductivity. If the material is isotropic, then $k_x = k_y = k_z = k$.
To understand how the heat is dissipated in the frame, the NUMEN target has been schematized in a simple squared geometry shown in figure 15.

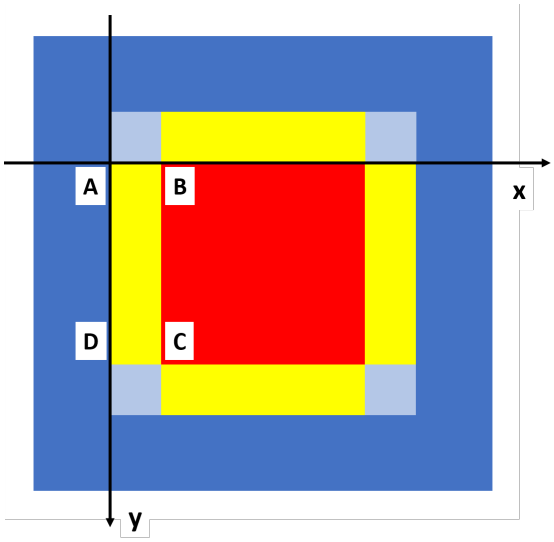

Figure 15: *Model used in a first approximation of a NUMEN target. The red region is illuminated by the target and heated at uniform temperature; the yellow regions are pinched by the cold frame; the cold frame is showed in dark blue and its temperature is fixed at a certain value T_{cold}; corner squares, light blue colored, are supposed to be at temperature T_{cold}, like the dark blue frame.*

Some assumptions have been made to perform the calculations:

i) The target is pinched by a cold frame kept at temperature T_{cold}. Yellow regions in figure 15 show where the target is clamped, while the cold frame is pictured in dark blue. All of the exposed target surface (red region) is illuminated by the beam. Light blue corner squares are supposed to be at the same temperature T_{cold} of the frame;

ii) The system is in stationary conditions, so all of the heat entering in the red region is dissipated in the cold ones;

iii) The heat equation (11) has been evaluated in one of the yellow regions, where the heat term is null.

Treating the temperature function as composed by the product of three independent functions of x, y and z, say $X(x), Y(y), Z(z)$, the solution is found to be a series of oscillating damped functions:

$$\begin{aligned} T(x,y,z) =& T_{cold} + \frac{16T_{hot}}{\pi^2} \sum_{m,n=1,3,\ldots}^{\infty} \frac{1}{mn} \sin\left(\frac{m\pi}{h}y\right) \sin\left(\frac{n\pi}{s}z\right) \\ & e^{\sqrt{\alpha_{mn}}(x-w)} \frac{1-e^{-2\sqrt{\alpha_{mn}}x}}{1-e^{-2\sqrt{\alpha_{mn}}w}} \end{aligned} \tag{12}$$

Where w, h, s are the full dimensions of one yellow parallelepiped target along x, y, z respectively. The details of these calculations are reported in Appendix A, together with the values of the α_{mn} parameters.

The formula 12 gives the temperature inside a yellow volume in stationary conditions. This volume receives heat from the unclamped target and releases the same amount of heat (per unit time) to the cold frame. The spatial behavior of the temperature can be deduced looking at the various terms of equation 12:

a) the temperature of each point (x,y,z) inside the clamped (yellow) region is linear with the temperature at the surface BB'C'C (see appendix): the proportionality coefficient is a product of $\frac{16}{\pi^2}$ multiplied by the series over m,n;

b) The proportionality coefficients on y and z behave as sin functions, i.e. their value is within ± 1;

c) Each term of the series contains a factor $\frac{1}{m \cdot n}$, which is less than 1;

d) The dependence on x is contained in one fraction times an exponential: the fraction is always smaller than 1 (unless for $x = w$), while the exponential has an exponent always negative. This exponent is in modulus very big for all x apart in the region close to $x = w$. Therefore, the exponential is nearly null in the yellow region, except for a thin layer close the red region, of thickness of the order of s: in other words, the temperature in the most part of the clamped region is the same of the cold frame.

It can be safely assumed that the target region clamped by the cold frame remains almost entirely at the frame cold temperature. In figure 16 the temperature inside the yellow region is reported as a function of the x coordinate. The solution (equation 12) is analogous for the remaining 3 yellow regions; the total heat deposited inside the illuminated region by the ion beam is transferred to the cold frame through yellow regions, or, equivalently, through one (yellow) parallelepiped of height $4h$.

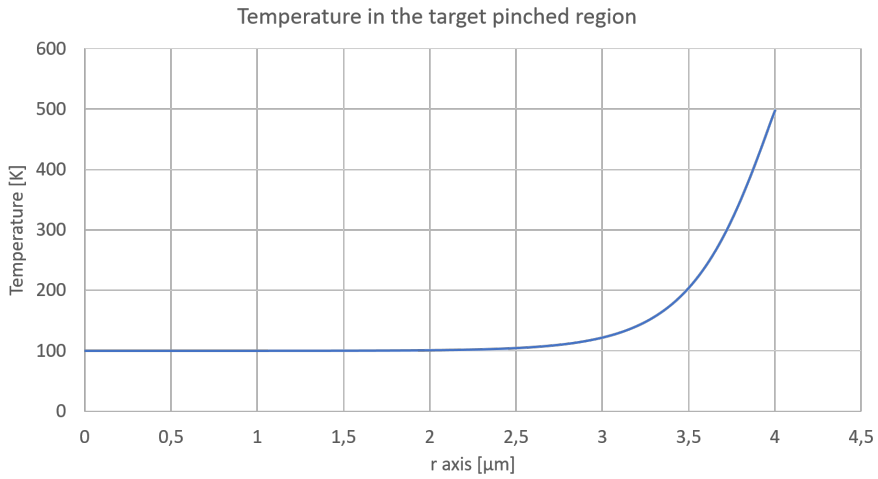

Figure 16: *Temperature profile along the x-axys, in the center of the BB'CC' face ($y = h/2, z = s/2$). The cold temperature is set equal to* 100 *K, while the hot one is equal to* 500 *K.*

This simple model shows that heat propagates just slightly beyond the limit of the clamped region. The temperature quickly falls to the T_{cold} value, has schematized in figure 17; hence, in further calculations, T_{cold} can be rightfully used as boundary condition.

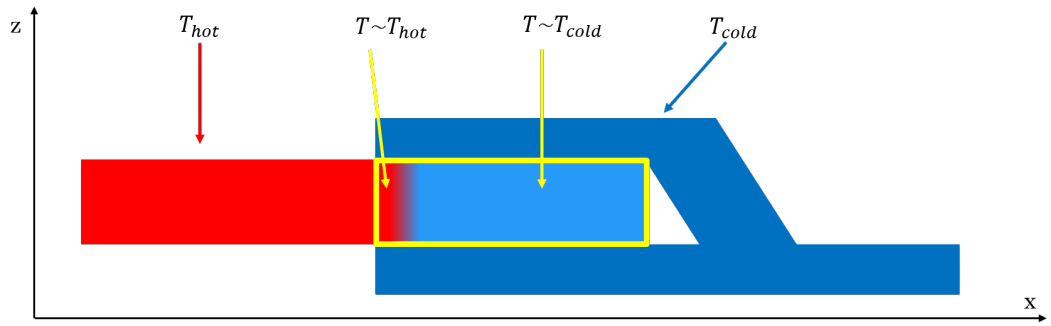

Figure 17: *Qualitative, not in scale, profile of the temperature along the x-axys in the target region pinched by the cold frame.*

Now that the boundary conditions have been established, it is possible to use a model more adapt for the actual target. In fact, the shape of the target showed in figure 9 is closer to be circular, rather than rectangular; thus, it may be convenient to switch to cylindrical coordinates. The complete heat equation, which contains also the time dependence, reads:

$$k_r \left(\frac{1}{r} \frac{\partial T}{\partial r} + \frac{\partial^2 T}{\partial r^2} \right) + k_\theta \frac{1}{r^2} \frac{\partial^2 T}{\partial \theta^2} + k_z \frac{\partial^2 T}{\partial z^2} + \frac{dQ}{dtdV} = \rho c \frac{\partial T}{\partial t} \tag{13}$$

Like in the previous case, the target boundary is clamped by a cold frame, kept at T_{cold}. In this scheme, the region irradiated by the beam is limited to a red spot in the target center. It is extremely important to keep the beam spot size within few mm in diameter, even after the upgrade of the apparatus. In fact, the future beams of NUMEN will be very intense and the tail of their Gaussian profile would otherwise overlap the frame, increasing the background.
In this configuration, the center of the target is irradiated by the beam and heated up to the melting temperature T_{hot}. The solution of eq. 13 in the red region indicates that the temperature does not vary appreciably. Therefore, it can be considered uniform in the range $0 \leq r \leq r_{beam}$. Figure 18 shows a scheme of the system under study.

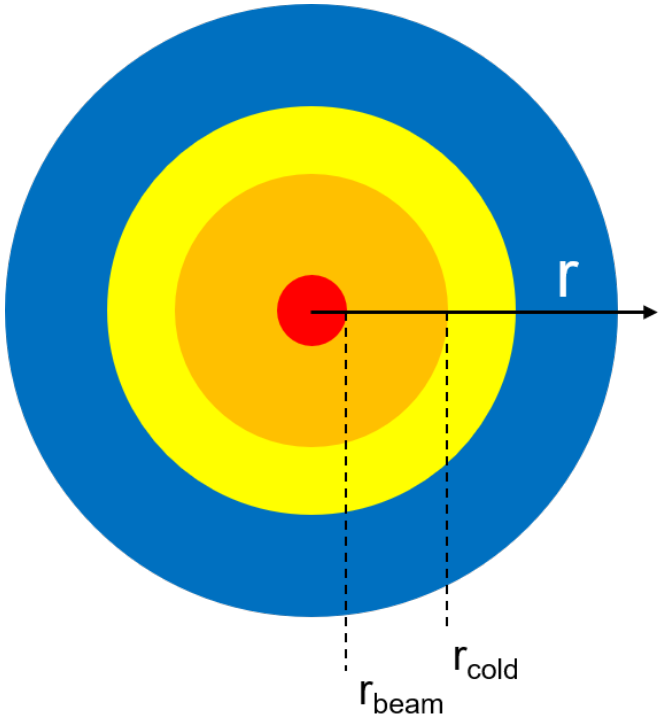

Figure 18: *Scheme of a cylindrical target, top view. The red region corresponds to the beam spot; the yellow region represents the target clamped by the cold frame at T_{cold}; the temperature is evaluated between r_{beam} and r_{cold}.*

Again, few approximations have been used in the calculations:

- The beam has a radius of 1.5 mm and heats uniformily the center of the target;
- The system has a cylindrical symmetry, and so has the temperature. Thus, the derivative along the θ coordinate is null;
- Since the heat is generated uniformly along the z-axis, the temperature is constant with respect to the z coordinate;
- The equation is solved outside the beam spot, where the heat source term is null;
- The system is supposed to be in stationary conditions, i.e. $\frac{\partial T}{\partial t} = 0$

With the aforementioned conditions, the equation reduces to:

$$k_r \left(\frac{1}{r} \frac{\partial T}{\partial r} + \frac{\partial^2 T}{\partial r^2} \right) = 0 \tag{14}$$

The heat equation is evaluated in the region between r_{beam} and r_{cold}; in those two points, the temperature is set equal to the melting point of the material and the cold frame temperature, respectively. With those boundary conditions, the solution of equation (14) is:

$$\begin{aligned} T(r) &= \frac{T_{hot}\ln r_{beam} - T_{cold}\ln r_{cold}}{\ln r_{cold} - \ln r_{beam}} + \frac{T_{cold} - T_{hot}}{\ln r_{cold} - \ln r_{beam}}\ln r = \\ &= K + T_0 \ln r \end{aligned} \tag{15}$$

Provided a suitable temperature function, it is now possible to relate the heat provided by the beam and the temperature profile of the target by using the Fourier equation:

$$\frac{dH}{dt} = -k_r S \frac{dT}{dr} \tag{16}$$

Where H is the heat supplied and S the surface through wich the heat flows. For a cylindrical target, S is proportional to the radius r:

$$\frac{dH}{dt} = -k_r 2\pi r s \frac{dT}{dr} \tag{17}$$

Where s is the target thickness. The maximum heat tolerable by the target can be calculated integrating along the radius and fixing the temperature to the material melting point. The melting temperature is then equal to:

$$T_{melting} = \frac{W_{tot}}{2\pi\ s\ k_r}\ln\frac{R}{r} \tag{18}$$

Being W_{tot} the power necessary to reach $T_{melting}$ and R the radius of the target. Rearranging for W_{tot}, equation 18 becomes:

$$W_{tot} = \frac{T_{melting} 2\pi \cdot s \cdot k_r}{\ln\frac{R}{r}} \tag{19}$$

Once the maximum tolerable power has been evaluated, one can calculate the beam intensity which generates such power, knowing the energy E_{ion} deposited by one particle by using the Bethe-Bloch equation 8. Dividing the total

power by the energy deposited by one particle one obtains the number of incoming ions per second. The current is then obtained by simply multipling the charge of each ion:

$$I_{max} = e \cdot z_{ion} \frac{W_{tot}}{E_{ion}} \tag{20}$$

The maximum beam current for each NUMEN target is reported in figure 19.

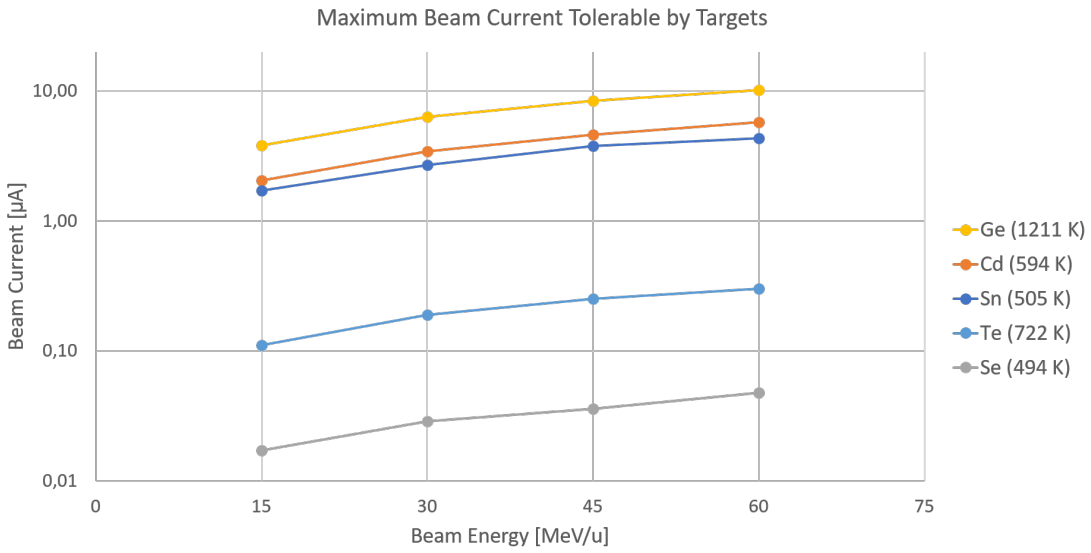

Figure 19: *Semilogarithmic plot showing the maximum beam currents calculated for* 1 *μm thick* ^{116}Cd, ^{130}Te, ^{76}Ge, ^{76}Se *targets and* 800 *nm thick* ^{116}Sn *target. In the legend is reported, in bracket aside the material name, the melting point of the material.*

The plot reported in figure 19 shows that stand-alone targets can tolerate fairly small beam currents, due to their geometry. In fact, heat has to travel a relatively long distance before reaching the cold sink, while the thickness through which it can flow is extremely thin. Geometrical factors paired with generally low thermal conductivity of the target hamper the heat dissipation and, therefore, limit the maximum current to few μA for Ge, down to few nA for Se.
It is evident that targets cooled just by a simple frame cannot withstand the beams expected for the NUMEN project. Therefore, the thermal resistance of the targets must be improved.

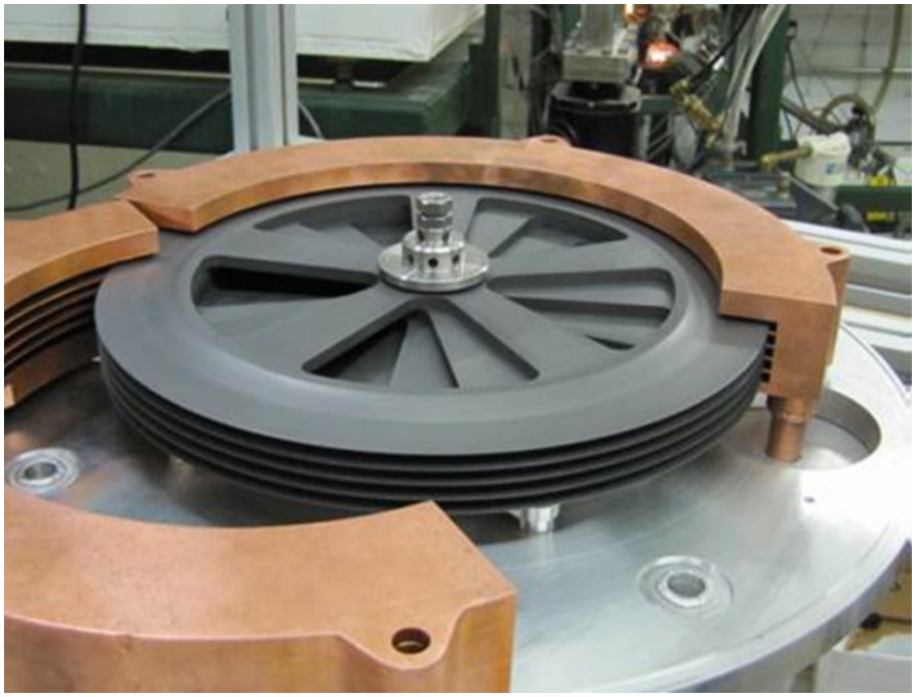

Figure 20: *Carbon target used at the Facility for Rare Isotope Beams (FRIB) for the production of heavy isotopes [39]. The multi-slice design improves the heat dissipation.*

Currently, the most diffused solution involves the usage of spinning targets [37, 38]. The target material is deposited on an annulus, in several sections of variable length. Such kind of target is often used in the production of heavy elements ion beams; the target material, which in this cases is usually graphite, can be several millimeters thick. The fast rotation allows to keep the target below the melting temperature, the heat being dissipated mainly through thermal radiation.

However, this kind of apparatuses are large and cumbersome, requiring moving parts under vacuum. Moreover, heat is dissipated mainly through thermal radiation, since the fast spinning movement prevents an efficient liquid driven refrigeration [40]. The irradiated power is proportional to $\propto T^4$, hence this approach is not suited for low melting point targets. The latter statement is an issue of major concern for the NUMEN project, but there are several other reasons on why spinning targets are not a viable solution, starting from the large area of the target. If the thickness uniformity is a crucial parameter, like in NUMEN, the vast area makes it more problematic to obtain a uniform deposition of few hundreds of nanometers. Also, it should be possible to move the target for calibrating reasons, but to move the whole spinning

system would be a delicate operation. Lastly, a spinning target would clutter the scattering chamber, covering other detectors or totally preventing their placement. The problem needs to be seen from another perspective.

3.2 HIGHLY CONDUCTIVE SUBSTRATE

The targets scarce thermal conductivity is the major obstacle in the heat dissipation. Backing the targets with a high thermally conductive substrate may offer an easy solution to the problem, providing the heat with a faster path to reach the cold sink. A part from being highly conductive, the substrate must meet other requirements: it must be thin, mechanically and thermally strong, it must not interfere excessively with the beam or the reactions.
A suitable candidate which meets all of these demands is carbon, which comes in a variety of allotropic forms with different properties. In general, carbon based materials are light, have low density and a great thermal resistance. Moreover, the interactions between the carbon and the oxygen and neon beams are well known from background measurements in NUMEN phase one.
Among all of the carbon allotropes, diamond is the one having the best physical characteristics. It possesses the highest thermal conductivity among natural occurring materials, having a value of k higher than 2200 $\mathrm{Wm^{-1}K^{-1}}$ [41]. It is also extremely hard, mechanically strong and chemically inert under normal conditions. Disk shaped diamonds, deposited by Chemical Vapor Deposition (CVD), having an excellent cristallinty, being few μm thick and several cm wide are commercially available.
At first glance, diamond would be the perfect substrate for this application, but there are some important issues to face. Some of them, such as the handling and the cost, are not impossible to overcome. Addressing the former issue, the substrate should be only few μm thick in order to not interfere with reaction products, like the target used in the PANDA experiment [42]; however, such a thin lamella it's quite fragile, and would require an extremely careful handling during target deposition, mounting and characterization. It would not be possible to produce expendable targets for characterization purposes, some characterization techniques being undoubtedly useful but destructive (e.g. cross-section imaging with a SEM, a Scanning Electron Microscope).
The first issue is closely related to the cost of such substrates: each substrate would have a cost in the range of a thousand euros, and to find the proper deposition conditions for each material would easily require tens of substrates.
There is a problem which could not be solved with just a vast amount of money:

radiation related damages. The diamond lattice would undergo graphitization under ion beam irradiation [43, 44], losing its properties and possibly compromising the heat dissipation. The high intensity ion beam used in NUMEN would readily destroy the diamond structure, and hence all the cooling system.
An alternative to diamond is graphite. Generally, graphite is composed by flakes of hexagonal-arranged carbon atoms. The dimension and the orientation of those flakes determines the type of graphite and its peculiar physical and chemical properties [45]. In particular, one special kind of graphite may be a good candidate for the intended application: the Highly Oriented Pyrolytic Graphite (HOPG). It is an artificial graphite made of stacks of graphene layers, whose relative orientation angle is less than 1°. It can be produced in large, thin foils some μm thick, which are relatively inexpensive, lightweight, flexible and mechanically resistant. HOPG most important characteristic, however, is its anisotropic thermal conductivity. Considering some commercially available HOPG sheet, such as Panasonic's (10 μm thick) or Optigraph's (5 μm thick), the value $k_{\parallel}$ of the thermal conductivity along the planes can be as high as 1950 $\mathrm{Wm^{-1}K^{-1}}$, while in the perpendicular direction $k_{\perp}$ is about 3 $\mathrm{Wm^{-1}K^{-1}}$ [46, 47]. Differently from diamond, defects in the HOPG crystal do not compromise the performances, making this material resistant against radiation damages [48].
The minimum available thickness for Panasonic graphite is 10 μm, a thickness which would introduce an excessive error due to the straggling of the particles. For this reason, a thinner graphite only few μm thick will be likely used (such as Optigraph's). The contribution of the HOPG substrate to the total resolution has been evaluated by considering a 5 μm thick sheet, using the same code used in section 2.3. The non uniformity of the targets have been considered equal to the previous case: gaussian, with a $\sigma_{Target} = 6.7\%$.

By looking at figures 21 - 25, it can be noticed that the error introduced by the graphite is roughly of the same order of magnitude of the one introduced by the SC and the spectrometer.
The addition of a further layer affects the maximum target thickness. In order to maintain the total energy resolution below the maximum tolerable limit, the thickness of the target must be reduced. For instance, the upper limit thickness for the ^{116}Sn target lowered from 800 nm to 400 nm (figure 21). For other targets (such as ^{130}Te, ^{76}Ge, ^{76}Se, figures 25, 23 and 22 respectively) the limit is less compelling, but for target thicknesses around $400 - 600$ nm the total resolution is very close to the upper limit. The only exception is ^{116}Cd (figure 24), for

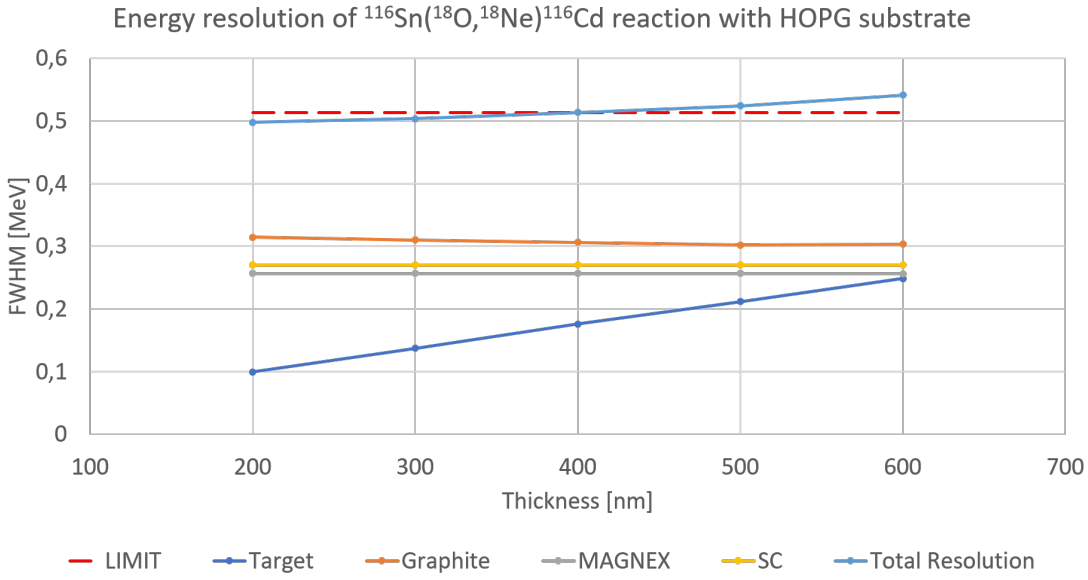

Figure 21: *Energy resolution for a Sn target in the $^{116}Sn(^{18}O,^{18}Ne)^{116}Cd$ reaction at* 15 *MeV/u, as a function of the target thickness. The dotted red line is the upper limit of the tolerable error. The target non uniformity is supposed gaussian, with a σ_{Target} equal to* 6.7% *of the average thickness. The HOPG is supposed* 5 *µm thick.*

which the limit is still much higher than the total resolution.
The drawbacks in terms of resolution seem easily manageable, but evaluations of the thermal behaviour are needed in order to validate the idea.

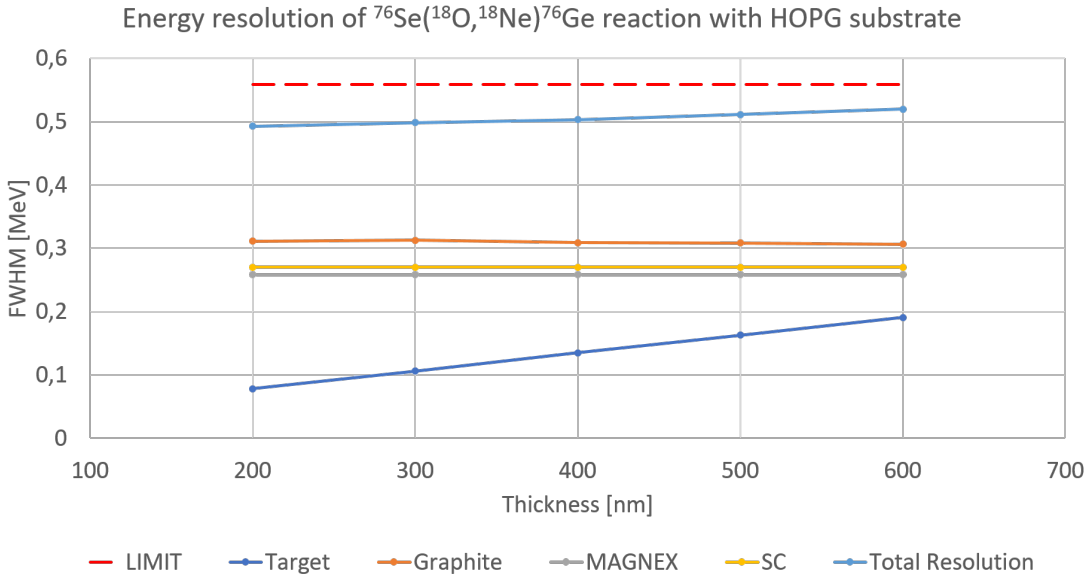

Figure 22: *Energy resolution for a Se target in the ^{76}Se(^{18}O,^{18}Ne)^{76}Ge reaction at* 15 *MeV/u, as a function of the target thickness. The dotted red line is the upper limit of the tolerable error. The target non uniformity is supposed gaussian, with a σ_{Target} equal to* 6.7% *of the average thickness. The HOPG is supposed* 5 *µm thick.*

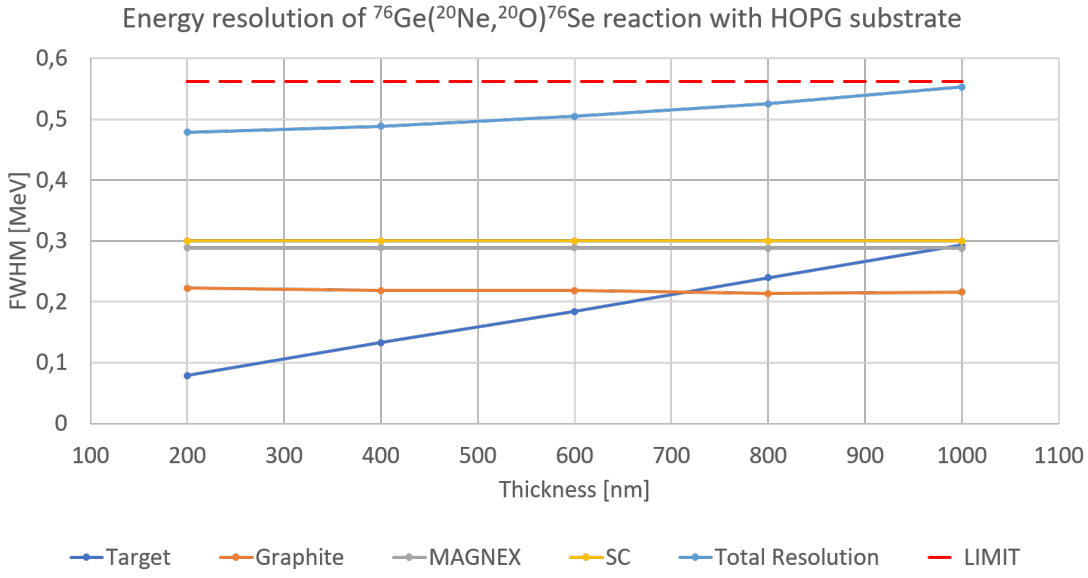

Figure 23: *Energy resolution for a Ge target in the ^{76}Ge(^{20}Ne,^{20}O)^{76}Se reaction at* 15 *MeV/u, as a function of the target thickness. The dotted red line is the upper limit of the tolerable error. The target non uniformity is supposed gaussian, with a σ_{Target} equal to* 6.7% *of the average thickness. The HOPG is supposed* 5 *µm thick.*

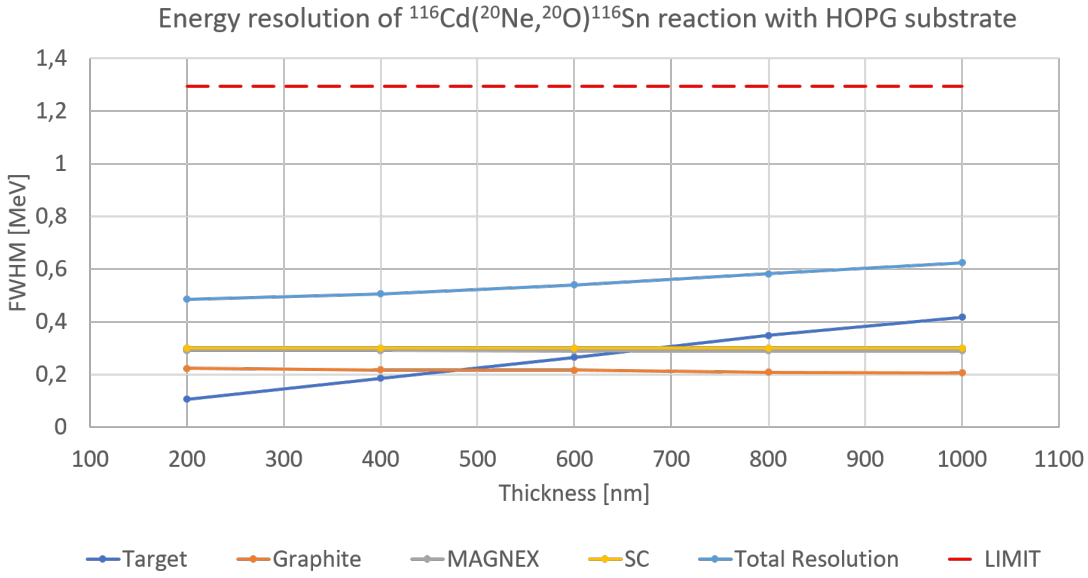

Figure 24: *Energy resolution for a Cd target in the $^{116}Cd(^{20}Ne,^{20}O)^{116}Sn$ reaction at 15 MeV/u, as a function of the target thickness. The dotted red line is the upper limit of the tolerable error The target non uniformity is supposed gaussian, with a σ_{Target} equal to 6.7% of the average thickness. The HOPG is supposed 5 µm thick.*

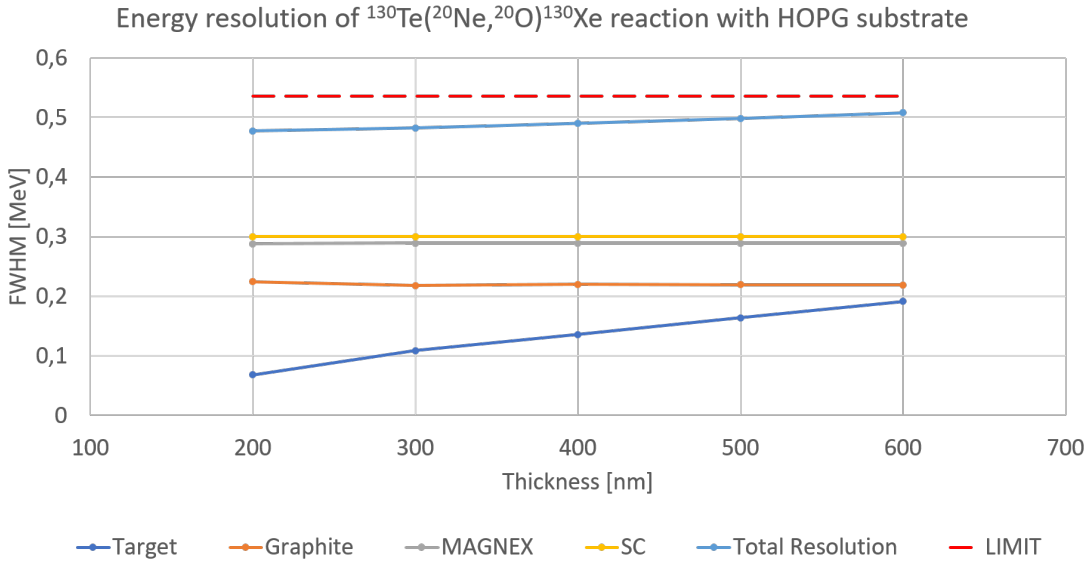

Figure 25: *Energy resolution for a Te target in the $^{130}Te(^{20}Ne,^{20}O)^{130}Xe$ reaction at 15 MeV/u, as a function of the target thickness. The dotted red line is the upper limit of the tolerable error. The target non uniformity is supposed gaussian, with a σ_{Target} equal to 6.7% of the average thickness. The HOPG is supposed 5 µm thick.*

4

NUMERICAL EVALUATION OF THE GRAPHITE SUBSTRATE CONTRIBUTION

The addition of a substrate increases the complexity of the target, in particular for what concerns the understanding of its the thermal behaviour. The temperature profile for a standalone target (eq. 15) was obtained in a quite straightforward way, but relied on some assumptions, some of which are not applicable in this case, such as the temperature uniformity along the z-axis. Complications of adding a second material as substrate include, e.g., the usage of different properties of two materials or different amounts of heat deposited in the target and in the substrate.
The solution to the problem can be approached from both the analytical side and from the numerical one. The analytical solution would be more precise, nonetheless it would also be more complex and time consuming. Thus, the numerical calculus has been chosen to perform a quicker feasibility study, even though intrinsically approximated. The code, reported in Appendix A, has been written in MatLab environment [49].

4.1 CODE FOR THE NUMERICAL SOLUTION OF THE TEMPERATURE EQUATION

The most general statement about the code is that it solves the non stationary heat equation, in cylindrical coordinates, for the target-substrate system. The substrate, a 5 μm thick HOPG sheet, is supposed larger than the target, in order to be easily clamped by the cold frame. The only region which needs to be exposed is the target, to guarantee that the beam can pass through without interacting with the sample holder.
The idea is schematically showed in figure 26. The portion of the graphite clamped by the sample holder can be considered at fixed temperature, thanks to the solution derived in the cartesian geometry (equation 12); such solution has been applied to the graphite and the results are shown in the plot reported in figure 27: even supposing a pretty high temperature at the border, only a thin layer few tens of μm has a temperature dissimilar to the cold frame

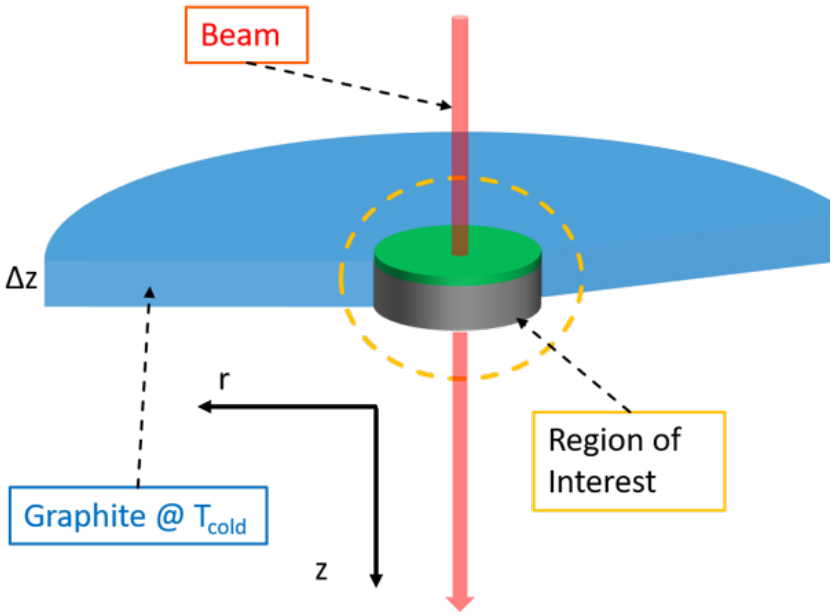

Figure 26: *Scheme of the target-graphite system. The graphite which exceeds the target, showed in light blue, is pinched by the sample holder and kept at T_{cold}; the region of interest (ROI - yellow dashed circle) is the one considered in the calculations. The beam deposits heat at the center of the ROI.*

one. Thus, the temperature equation can be solved only in the target and the underlying graphite. The boundaries of this region are supposed at the constant temperature T_{cold} of the clamped graphite. The beam crosses the system at the center, depositing a certain amount of heat in the target and in the substrate.

The power deposited in the targets has already been calculated and showed in table 2. However, the plots reported in figures 21-25 highlight that, for most of the targets, the total energy resolution approaches the limits, due to the HOPG substrate. Hence, for precaution reasons, the calculations have been performed supposing an average thickness of the targets of 400 nm. The values of the power deposited in 400 nm thick targets are reported in table 3.

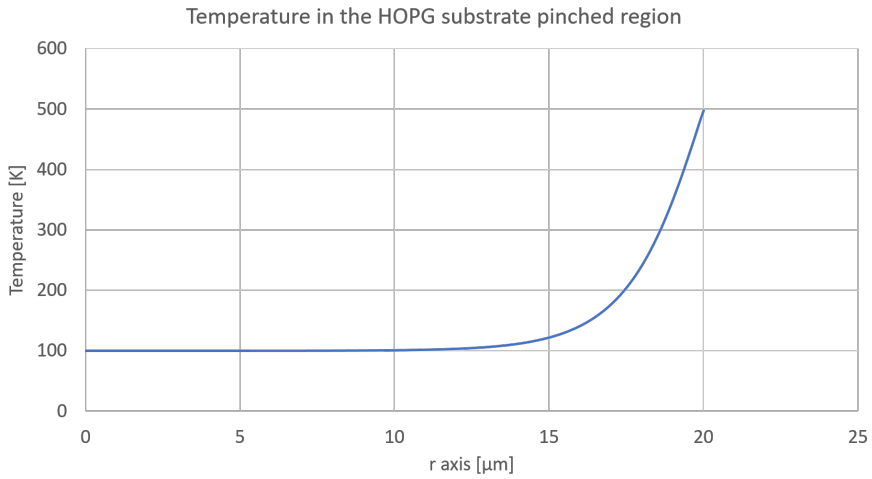

Figure 27: *Temperature profile along the r-axis in the graphite region clamped by the cold frame, at* $z = 2,5$ *µm. Supposing a temperature of* 500 *K at the clamped region boundary, only a* 10 *µm thick layer is warmer than the frame.*

	Beam Energy [MeV/u]			
	15	30	45	60
Power in ^{116}Sn [W]	2,01	1,2	0,88	0,71
Power in ^{76}Se [W]	1,49	0,88	0,64	0,52
Power in ^{76}Ge [W]	1,96	1,15	0,85	0,68
Power in ^{116}Cd [W]	2,87	1,71	1,26	1,02
Power in ^{130}Te [W]	1,97	1,17	0,87	0,7

Table 3: *Heat deposited in* 400 *nm thick targets, for different beam energies. The beam current is supposed equal to* 50 *µA.*

Crossing a second material, namely the graphite, the beam will generate additional heat. Again, using the Bethe-Bloch equation (8) it is possible to evaluate the power deposited into the substrate. The values are reported in table 4.

	Beam Energy [MeV/u]			
	15	30	45	60
^{18}O Beam [W]	12,49	7,09	5,11	4,07
^{20}Ne Beam [W]	15,63	8,86	6,39	5,09

Table 4: *Power deposited in* 5 *μm graphite by* ^{18}O *and* ^{20}Ne *ion beams, at different energies, after crossing* 400 *nm thick targets. The beam current is supposed equal to* 50 μA.

Even though the absolute values of the power deposited in the graphite are higher than the ones deposited in the targets, the energy densities in the latter are significantly higher. Considering the values reported in table 5, it appears clear that the targets must endure a higher thermal stress with respect to the graphite substrate.

Power density per unit length [W/μm] under ^{18}O/^{20}Ne beams					
Graphite (^{18}O/^{20}Ne)	^{116}Sn(^{18}O)	^{76}Se(^{18}O)	^{76}Ge (^{20}Ne)	^{116}Cd (^{20}Ne)	^{130}Te (^{20}Ne)
2,5/3,12	5,02	3,73	4,9	7,19	4,93

Table 5: *Linear power density deposited by a* 50 μA *beam at* 15 *MeV/u in targets and graphite substrate.*

The starting point, analogously to the procedure used in section 3.1, is equation 13. However, in this case the only approximation is the cylindrical symmetry, which reduces the original equation to:

$$k_r \left(\frac{1}{r} \frac{\partial T}{\partial r} + \frac{\partial^2 T}{\partial r^2} \right) + k_z \frac{\partial^2 T}{\partial z^2} + \frac{dQ}{dtdV} = \rho c \frac{\partial T}{\partial t} \tag{21}$$

This approximation is justified by the shape of the object under investigation: the beam propagates radially, since the target, the graphite and the boundaries are cylindrical. The system is therefore divided into a series of concentric rings; the inner rings are heated by the beam, which has a gaussian profile with $\sigma = 1$ mm, while the boundaries of the outermost rings are at fixed temperature T_{cold}. The division of a continuous object into a discrete one

is called discretization, and the collection of such discrete points is called *mesh*. The studied function is solved in each one of such points; the denser the mesh, the more the numerical solution approaches the analytical one. A scheme of the mesh is showed in figure 28.

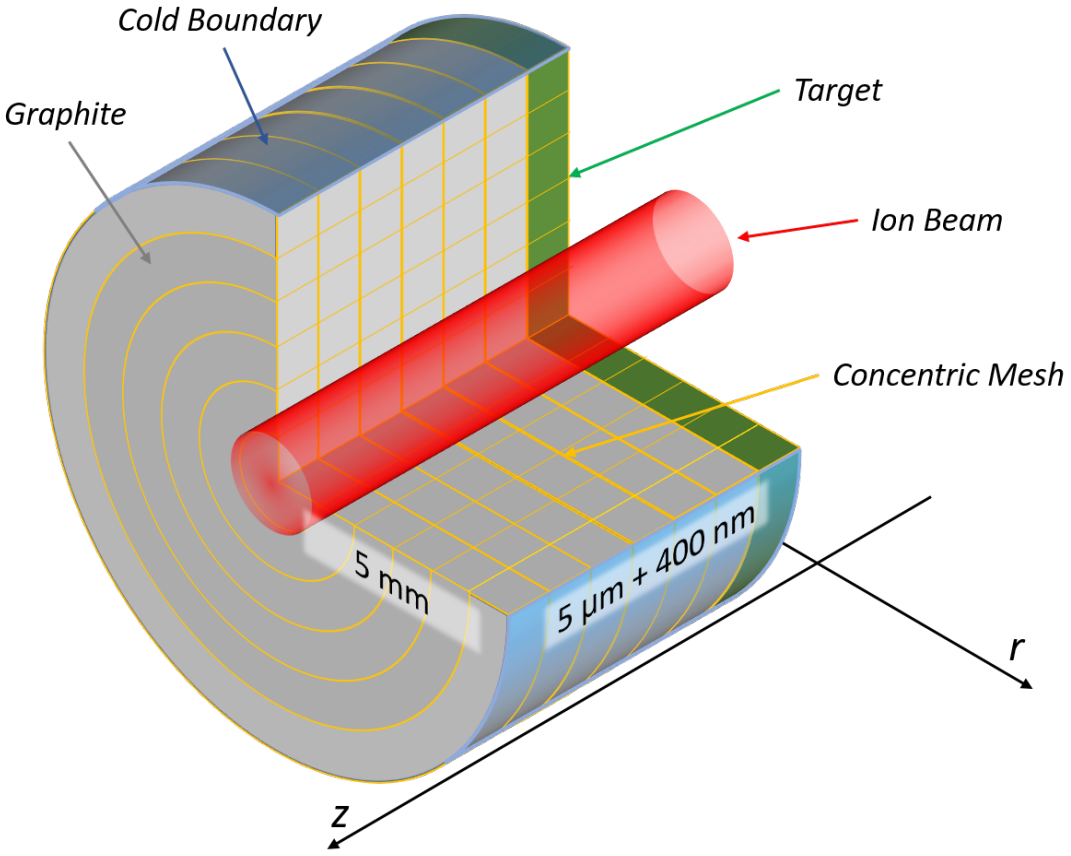

Figure 28: *Scheme (not in scale) of partition of the target-graphite system. The rings which fall within the gaussian ion beam receive a certain amount of heat, according to their characteristics (position, material, etc); the generated heat is dissipated in the cold boundary at fixed temperature.*

The physical properties of the material and the amount of heat received are associated to each point of the mesh: (ρ_{target}, c_{target}, k_{target} if the point is within the target, $\rho_{graphite}$, $c_{graphite}$, $k_{graphite\perp}$ and $k_{graphite\parallel}$ elsewhere).
The value of the spatial infinitesimal dr can be chosen quite freely, its minimum

size being limited only by an excessive increase of the computational time. On the other hand, the physical dimension of the system along the z-axys is much smaller than the radial one; thus, the value of dz is bound to be smaller than dr. Moreover, the target is much thinner than the graphite, so using a single value for dz would make the mesh in the graphite extremely dense, increasing the computational time with no appreciable advantage in the precision. Hence, dz may have different values in the two materials. On one hand, this approach allows to save computational time, but the two values of dz introduce an issue at the target-graphite interface. To get around the problem, the formula used for compute the second derivatives along z for an interface mesh point has been rewritten. For a general j-th mesh point, the central derivative formula is:

$$\frac{d^2T_j}{dz^2} = \frac{\Delta T_{j-1} - 2\Delta T_j + \Delta T_{j+1}}{\Delta z^2} \tag{22}$$

For a i-th point at the interface, formula 22 was rewritten specifying each contribution:

$$\frac{d^2T_i}{dz^2} = \frac{\frac{\Delta T_{i-1}}{\Delta z_{target}} - \Delta T_i \left(\frac{1}{\Delta z_{target}} + \frac{1}{\Delta z_{graphite}}\right) + \frac{\Delta T_{i+1}}{\Delta z_{graphite}}}{\Delta z_{target}} \tag{23}$$

The space intervals dz and dr can be chosen quite arbitrarily, but the value of the time interval dt cannot. In fact, its value must be taylored on the used computational method and on the space intervals. The code uses an explicit method, in which the stability is achieved if the time derivative satisfies the condition:

$$dt \leq \frac{\rho c}{2k} min(\Delta x^2, \Delta z^2) \tag{24}$$

Since in the target region dz has a value of the order of 10^{-7} m (at most half of the target thickness), dt value ranges from $10^{-8} - 10^{-11}$ s, depending on the material properties. Decreasing the value of dz would not only increase the points in the mesh, but would also shrink the dt.
The code is supposed to calculate the state of the system after few seconds of irradiation, which would require to solve the heat equation for each point of

the mesh 10^{10} times. Therefore, a compromise between precision , e.g. the values of the infinitesimals, and computational time must be found.

To verify the accuracy of the code, the values of the temperature evaluated with it have been compared to the known analytical solution for the stand alone targets in stationary conditions. Targets were given the heat supplied by a 50 μA ion beam; such condition is of course non physical, since the targets would vaporize instantly. Nevertheless, despite the extremely high values reached by the temperature, it is a constructive comparison. In this case, to properly draw a parallel, the beam was supposed uniform across the beam spot. The results, reported in table 6, were satisfying.

	Temperature next to the beam spot				
	^{116}Sn	^{76}Se	^{76}Ge	^{116}Cd	^{130}Te
Analytical Solution [K]	20098	1951446	21781	19881	444573
Numerical Solution [K]	20158	1955811	21846	19940	445900
Discrepancy	0.3%	0.22%	0.3%	0.3%	0.3%

Table 6: *Comparison between the solutions obtained analytically and numerically for* 400 *nm thick targets, irradiated by a* 50 *μA ion beam. The agreement is very good nearby the beam spot.*

The agreement between the two solutions for all the targets is remarkable, the discrepancy on the reached maximum temperature being just of the 0.3% for most of the targets. For the Se target, the error was even lower; due to the exceptionally low thermal conductivity, the constrains on the time derivative had to be tighter for stability reasons. The results of the numerical code are always slightly greater than the analytical ones. As an example, figure 29 shows such comparison for a Sn target.

Calculations for the whole target-graphite systems were then performed, showing a net improvement in the heat resistance. The time evolution of the temperature is tracked from few ns up to the stationary state. The temperature profile is stored in plots, 10 for each order of magnitude from 10^{-9} s up to $10^{-2} - 10^{-1}$ s. Four plots of a Tin target are shown in figure 30, as a representative collection of typical plots. The first plot, figure 30a, shows the

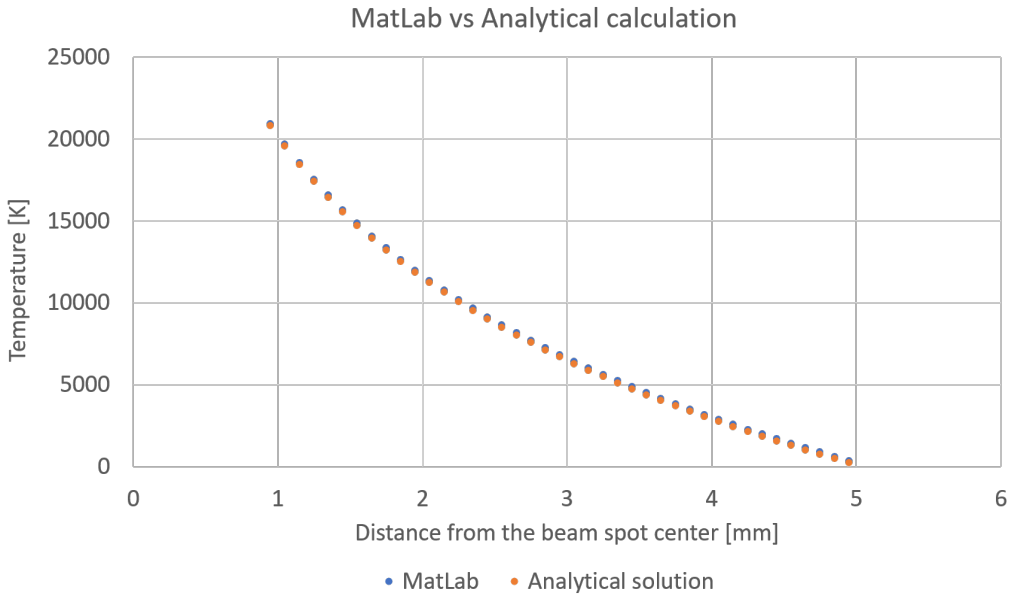

Figure 29: *Comparison of the temperature between the analytical and numerical solution for a* 400 *nm thick Sn target, as a function of the radius. The difference of the maximum values is of 0.3%.*

temperature distribution right after the beginning of the irradiation; the temperature is higher in the target due to the higher energy density deposited. After just few milliseconds, the temperature is uniform along the z-axis (30b), due to the overall limited thickness. The steady state is quickly reached in few ms (30c-30d).

By looking at the plots reporting the temperatures reached at the steady state, figures 30d - 34, it can be seen that most of the targets are able to endure a 50 μA ion beam. The only exception is the Se target, which hypothetical maximum temperature reached with a 50 μA beam current exceeds its melting point. For this target, the maximum current is estimated to be about 25 μA (figure 35). In all of the above-mentioned plots, the maximum temperature is always located in the center of the target.
Keeping record of the temperature reached in each time step by the targets, it is possible to plot the entire time evolution for each one of them: in figure 36 are reported the maximum temperature value of each of those plots. Even though the materials have quite different thermal properties, the steady state is always reached within 100 ms. Also the spread among the maximum reached

temperature in different targets is strongly reduced, suggesting that the temperature evolution is mainly driven by the graphite contribution. In table 7 are summarized the maximum temperatures reached by the targets irradiated with a 50 μA, 15 MeV/u ion beam.
By looking at table 7 it can be understood why the ^{116}Cd target thickness is limited to 400 nm. Differently from all of the other isotopes, for which the limit is due to the energy resolution, here the limitation comes from the heat generated by the beam. In a thicker target the generated power would be too high, bringing the target dangerously close to the melting point (or beyond). Of course it would be possible to lower the ion beam current, but then one would have the same reaction rate with a worsened energy resolution.

Maximum temperatures reached with a 50 μA, 15 MeV/u ion beam

^{116}Sn ($T_{melting}$ = 505 K)	^{76}Se ($T_{melting}$ = 494 K)	^{76}Ge ($T_{melting}$ = 1211 K)	^{116}Cd ($T_{melting}$ = 594 K)	^{130}Te ($T_{melting}$ = 722 K)
423 K	857,3 K	504,8 K	504,6 K	599 K

Table 7: *Summary of the maximum temperature reached by targets backed by a graphite substrate, irradiated by a* 50 μA, 15 *MeV/u ion beam.*

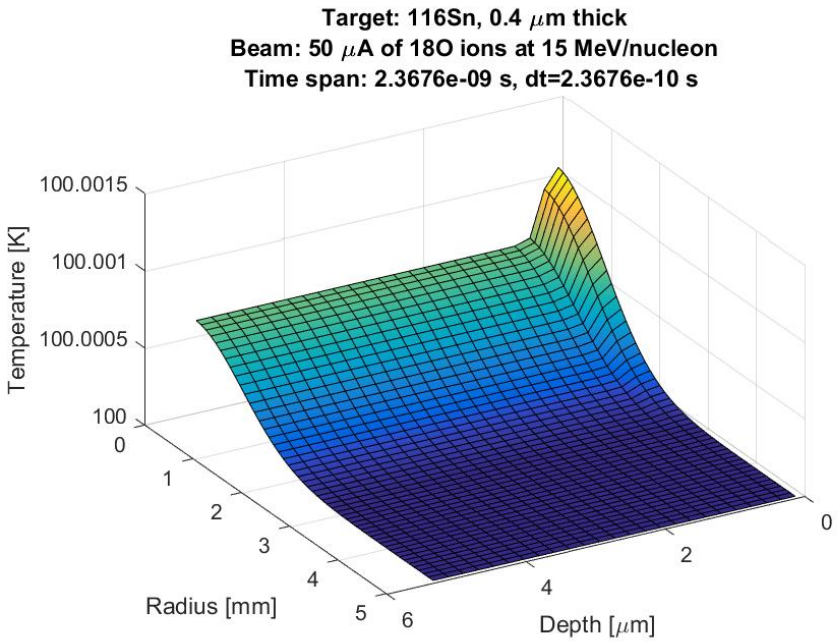

(a) *Tin target temperature profile after* 2.36 *ns*

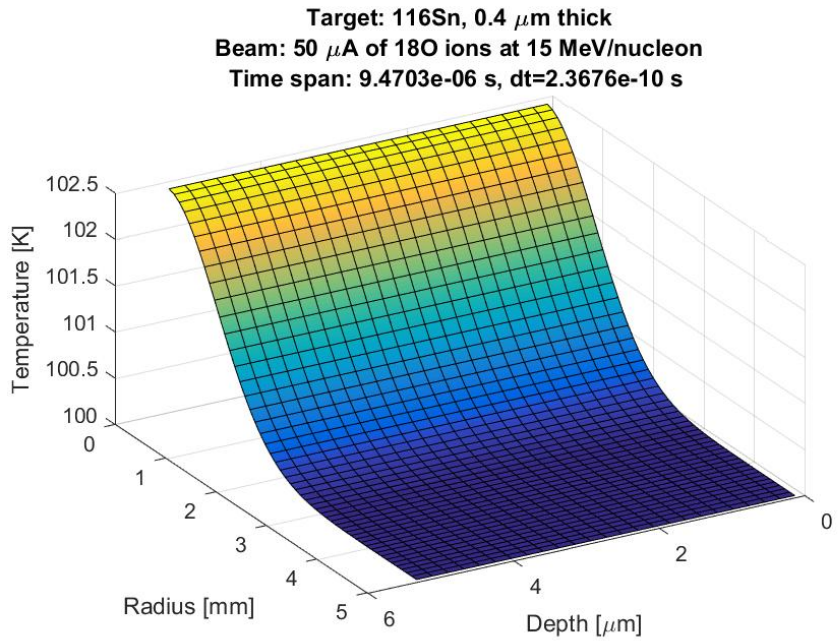

(b) *Tin target temperature profile after* 9.47 *μs*

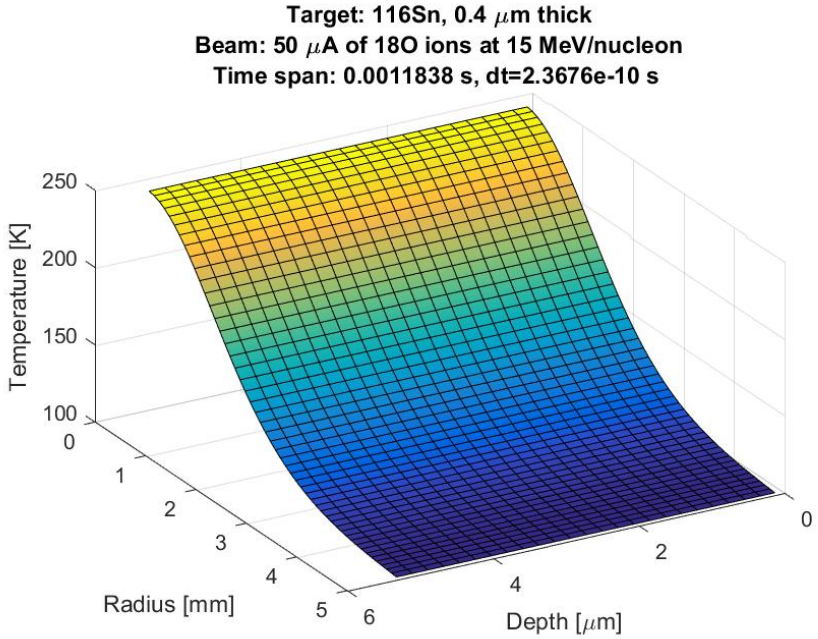

(c) *Tin target temperature profile after* 1.18 *ms*

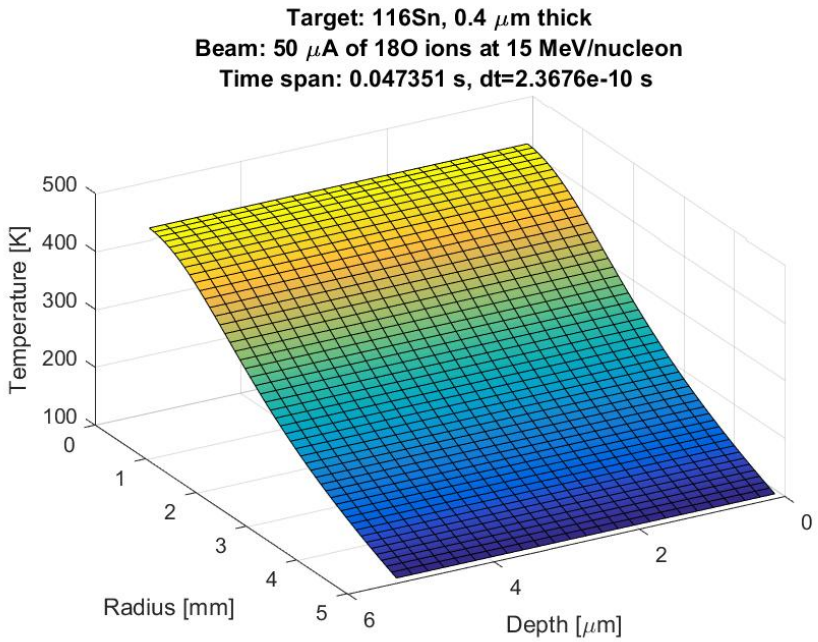

(d) *Tin target temperature profile after* 47 *ms*

Figure 30: *Temperature evolution of a* 400 *nm thick Tin target backed by a graphite substrate, from few ns up to the steady state. Equilibrium is reached after few tens of ms.*

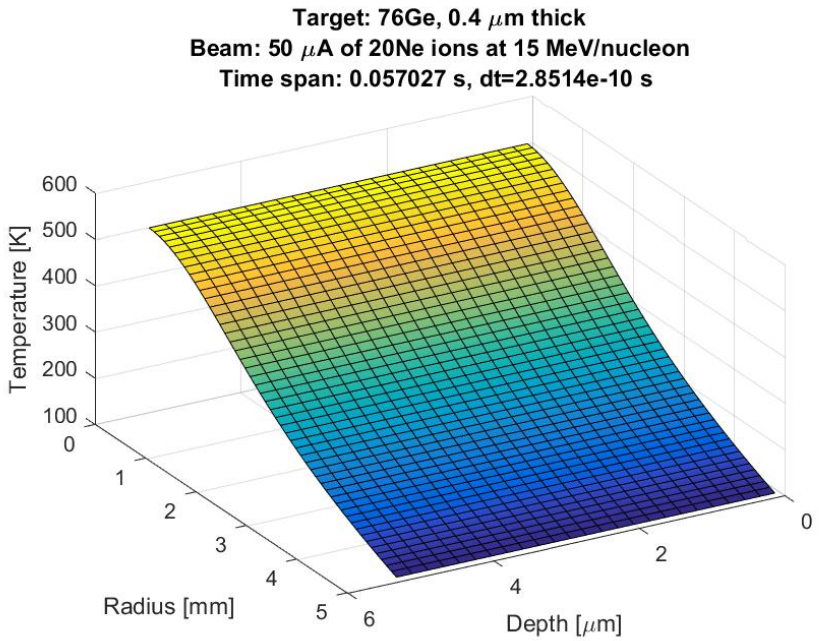

Figure 31: *Distribution of the steady.state temperature in ^{76}Ge target, with a* 50 μ*A,* 15 *MeV/u ^{20}Ne ion beam.*

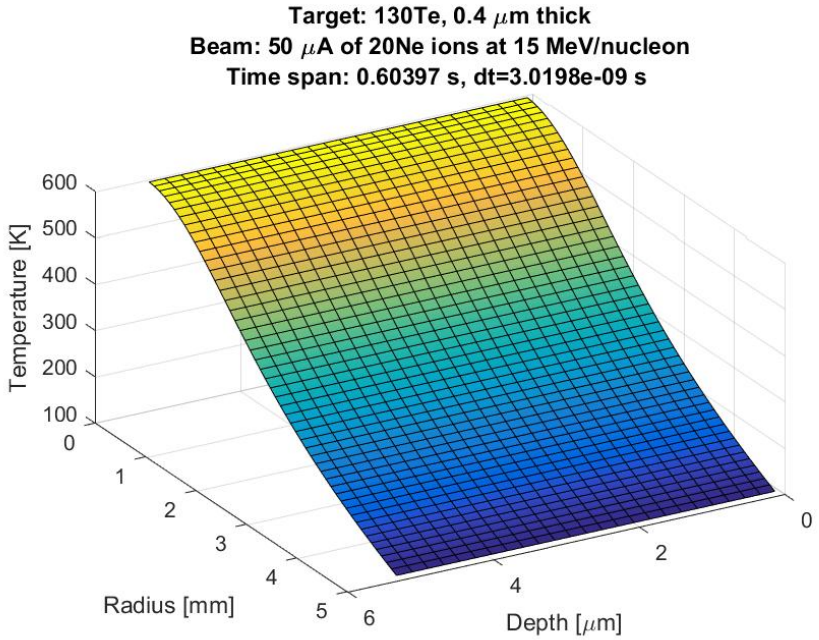

Figure 32: *Distribution of the steady state temperature in ^{130}Te target, with a* 50 μ*A,* 15 *MeV/u ^{20}Ne ion beam.*

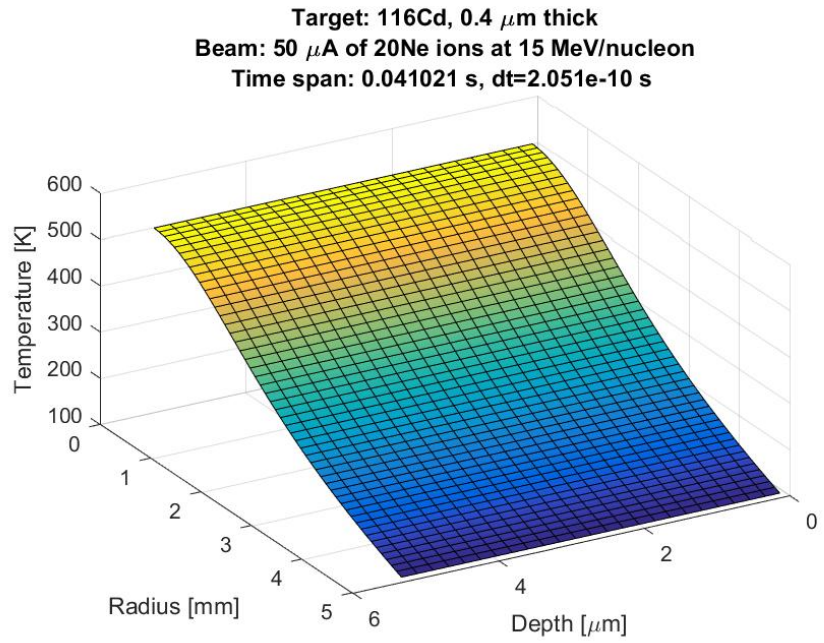

Figure 33: *Distribution of the steady state temperature in* ^{116}Cd *target, with a* 50 μA, 15 *MeV/u* ^{20}Ne *ion beam.*

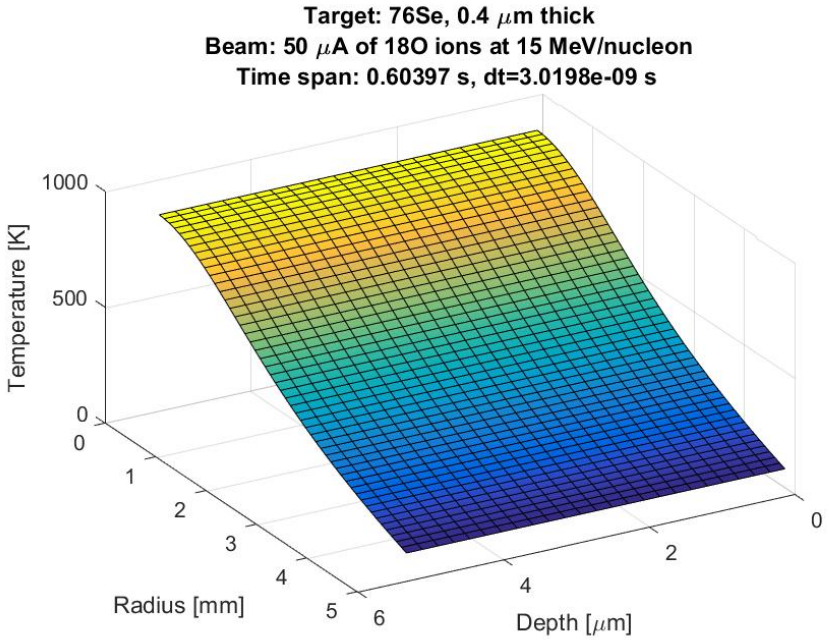

Figure 34: *Distribution of the steady state temperature in* ^{76}Se *target, with a* 50 μA, 15 *MeV/u* ^{18}O *ion beam.*

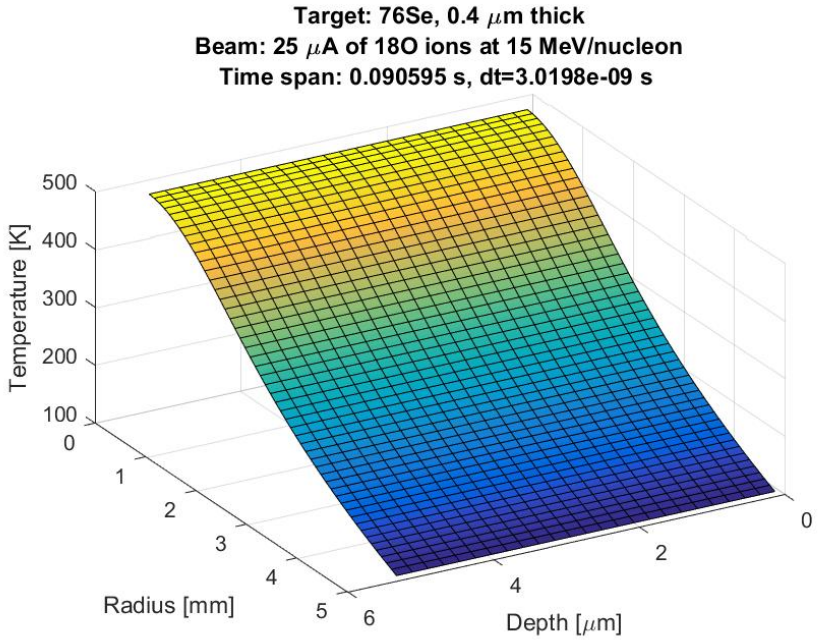

Figure 35: *Distribution of the steady state temperature in ^{76}Se target, with a* 25 *μA,* 15 *MeV/u ^{18}O ion beam.*

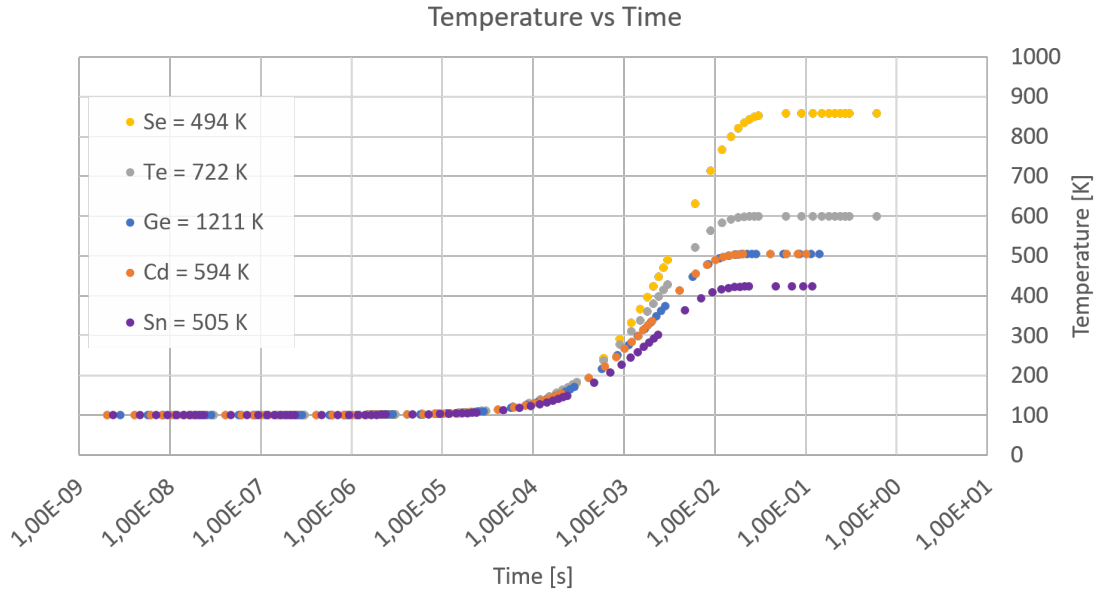

Figure 36: *Time evolution of the maximum temperature (at $r = 0$) for each target, irradiated by a* 50 *μA,* 15 *MeV/u ion beam. Only the Se target overcomes the melting point.*

5

DESIGN OF THE SAMPLE HOLDER AND COMSOL SIMULATIONS

The numerical evaluations performed with the numerical code provided promising results for the HOPG substrate solution. The next step in the work flow is then the design of a suitable sample holder, paired with a cooling system powerful enough to dissipate the generated heat.
However, there are some constrains concerning the satellites apparatuses or specific needs that must be met. To begin with, one must deal with the limited space available in the NUMEN scattering chamber. Although the upgrade of the whole experimental apparatus will include the modification of the chamber, its design is limited by the presence of the existing instrumentation, such as the beam line and the spectrometer, whose positions cannot be modified. The chamber will have to host a number of detectors, the most demanding of which, in terms of space, is the γ-ray detector.
Some of the nuclei targeted in NUMEN, such as the ^{76}Ge or the ^{116}Cd, are spherical. At low energies, the ground state and the first excited state can be well discerned even considering the error introduced by the SC and the spectrometer, which amounts to the 0.2% of the beam energy. The situation changes when moderately and strongly deformed nuclei are used, such as ^{110}Pd, ^{150}Nd, ^{160}Gd, or higher beam energies (40-60 MeV/u). In these cases the resolution of the spectrometer is not sufficient to distinguish between ground and excited states and, therefore, an ancillary detector is needed, namely the γ-ray detector [50].
The low cross section of the searched reactions requires a very good solid angle coverage, as close as possible to 4π. Hence, the cooling system must be small enough to not interfere with the γ detector placement, while leaving the target-detector line of sight as free as possible. As a final requirement, it must be mobile along the vertical axis, for calibration purposes; to this end, an alumina target with a pinhole and a graphite target are used. They must be placed on top of the actual target, requiring a vertical displacement of about 5 cm.
Keeping in mind all of these requirement and constrains, two cooling systems with relative sample holder were designed.

5.1 LIQUID NITROGEN BASED COOLING SYSTEM

The first system to be designed relies on liquid nitrogen to cool down the target. The graphite is clamped between two copper halves, whose shape is cylindrical, with a wide angular aperture near the target. The inside is hollow, to allow the flow of the liquid nitrogen. The hole in the center is wide as much as the target, i.e. 1 cm, while the outer diameter is 7 cm large. This dimension has been chosen to have a sufficiently large flowing chamber, 5 cm in diameter, leaving room for the 4 alignment rods and the 6 through screws. The liquid nitrogen enters the sample holder from a hole in the lateral side and exits from a diametrically opposite hole. The inlet faces downward, while the outlet upward, in order to avoid bubbles and clogs inside the sample holder.

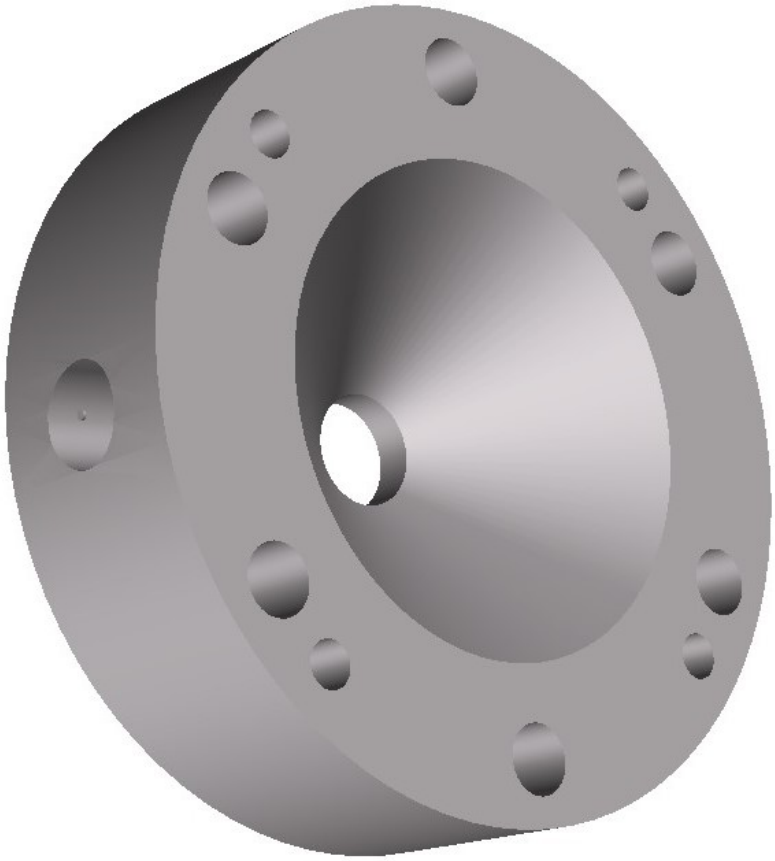

Figure 37: *3D image of the LN_2 cooled sample holder, front view. The hole is* 1 *cm wide, while the outer diameter is* 7 *cm. The external flat ring,* 1 *cm wide, is bulk copper and hosts the alignment rods (in the* 4 *smaller holes) and the screws (6 larger holes).*

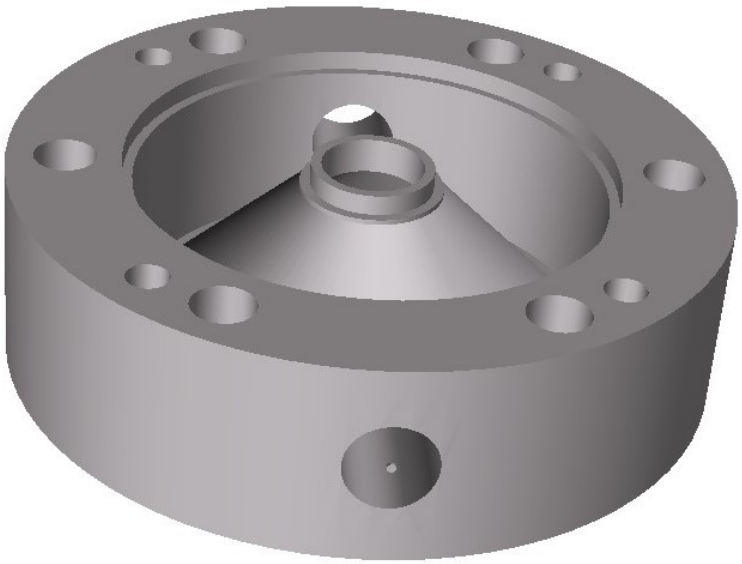

Figure 38: *3D image of the LN_2 cooled sample holder, rear view. The coolant flows only below the conical region, entering and exiting from the lateral side. The chamber is closed by a soldered copper disk.*

A clear advantage of this solution is the simple design; the sample holder does not require a custom scattering chamber to be mounted, but only a pass-through flange for the 2 inlets and 2 outlets. Liquid nitrogen can be easily provided and it is sufficient to connect a pressurized dewar to make the coolant flow. Moreover, the large copper object acts as a cold sink, having a considerable thermal capacity.
Unfortunately, there are also several drawbacks. If on one hand the size helps in keeping the system cold, it is an hindrance for the γ detection. Even providing a conical aperture near the target, as shown in figure 37, the large structure covers almost 3π of the full solid angle. The need for cryogenic pipes suitable for high vacuum adds complexity to the whole: in fact, they must be also quite flexible to allow the vertical shift required for calibration. Even by using compact pipes, they contribute to clutter the scattering chamber. This is not the only issue for using liquid nitrogen; it is in fact difficult to precisely evaluate the amount of heat which can be dissipated. It is also difficult to diagnose in

real time the free flow of the coolant and, despite the precautions, clogs may happen. Finally, a target change would be extremely time consuming, due to the cumbersomeness of the cooling system.

The simplicity of this apparatus does not balance the numerous drawbacks that come with it. This kind of sample holder could be used in preliminary tests of the target/graphite dissipation capabilities, where no γ detectors or displacement are needed, but is not suited for being used in the actual experiment. Finding a more reliable solution is mandatory.

5.2 CRYOCOOLER BASED COOLING SYSTEM

Generally speaking, a cryocooler is a device composed by a compressor, a circuit in which the refrigerant liquid flows, a cold finger and a heat exchanger [51]. The refrigerant liquid, usually liquid helium, cools down the cold finger, on which the object to be cooled is mounted. The warm helium is then compressed by the piston, to be cooled afterwards in the heat exchanger, by either water or air. Cryocooler can be with one or two cooling stages, depending on the characteristics one is looking for.
Cryocoolers are an ideal solution to cool down a sample without relying on external liquid coolant, such as liquid nitrogen in section 5.1. Getting rid of the LN_2 means a lot less clutter in the scattering chamber, due to absence of pipes. No pipes also means to ease the vertical displacement during calibration, and to facilitate the target change if required. The sample holder itself could be much thinner, since no liquid would flow in it, increasing the aperture of the target toward the γ-detectors.
This kind of system are generally extremely reliable, since they have no moving parts in vacuum, and produce very little vibrations. Another important point is the relation between base temperature and dissipated power, which is established by the manufacturer. In figure 39 it is shown a 2-stages Leybold cryocooler, able to dissipate up to 18 W while keeping the second stage at 20 K. This kind of cryocooler uses the Gifford-McMahon cycle [52], a thermodynamic cycle widely used in this kind of machines.

The sample holder can be directly mounted on top of the second stage, by means of screws or small magnets. The design of the new sample holder, shown in figure 40, is much lighter with respect to the previous one, even though the basic idea remains unchanged. The two identical halves are screwed together, squeezing the graphite substrate but leaving the target exposed; the

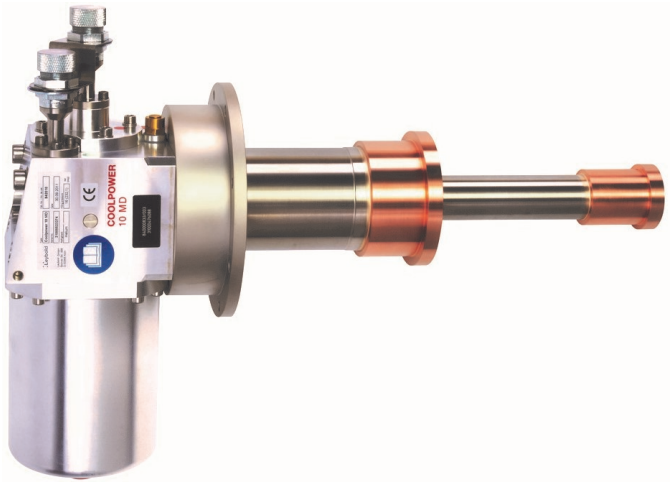

Figure 39: *The Leybold* 10 *MD cryocooler guarantess the heat dissipation needed for NUMEN, being able to dissipate up to 18W of power while keeping the second stage at 20K. The large copper part is the first stage, while the smaller copper end is the second stage cold finger.*

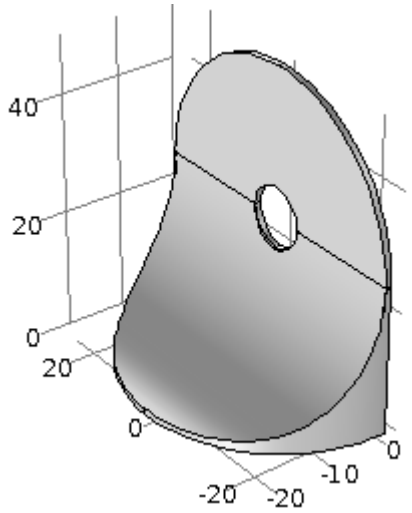

(a) *Preliminary design of one sample holder half.*

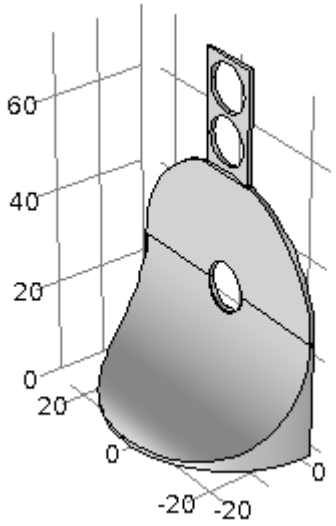

(b) *Preliminary design of one sample holder half, with the calibration targets slots on top.*

Figure 40: *This sample holder is designed to be mounted directly on top of the cold finger of the second stage, by means of screws or small magnets. The inner hole is* 1 *cm wide, the outer disk is* 5 *cm in diameter, as well as the base.*

whole thing is then fixed on the second stage. This design is suited for quick changes of the targets in case of failure or necessity. On top of the main body of the sample holder, it is possible to easily host the two calibration targets slots. Such targets can be placed away from the cold finger without fearing overheating issues, since the calibration is performed with low intensity beams (figure 40b).

Figure 41: *A Leybold 5/100 cryocooler joined with a bellow flange.*

The vertical displacement needed to select the target, either for calibrating or for data taking, can be achieved with a simple bellows flange (paired with a suitable motor). This solution is showed in figure 41: the cryocooler is fixed to the bellow thanks to the flange connection right above the motor.
Lastly, thanks to the fact that both the cold stage temperature and the dissipated power are known, evaluating the thermal behavior of the sample holder is now much more straightforward than with the LN_2 cooling system. To

evaluate the temperature distribution of the cryocooler sample holder, which receives heat from the irradiated target/graphite and dissipates it into the cold stage, the software COMSOL had been used, as explained in section 5.3.

5.3 COMSOL CALCULATIONS

COMSOL Multiphysics is a software platform for finite element analysis, able to simulate a large variety of physical systems, from mechanical to electromagnetic and heat transfer (https://www.comsol.com/). The physical system can be modeled through a CAD interface; the created object is then divided into a tri-dimensional mesh and the chosen physical model is solved in each mesh point.
The advantage with respect to the MatLab code resides in the possibility of evaluate the thermal behavior of the entire system, composed by target, graphite substrate and sample holder, in spite of several discontinuity points in the geometry and in the materials. However, as a first step the same geometry used in MatLab was analyzed, i.e. the cylinder composed by the target and the underlying graphite, with a fixed temperature at the boundary.

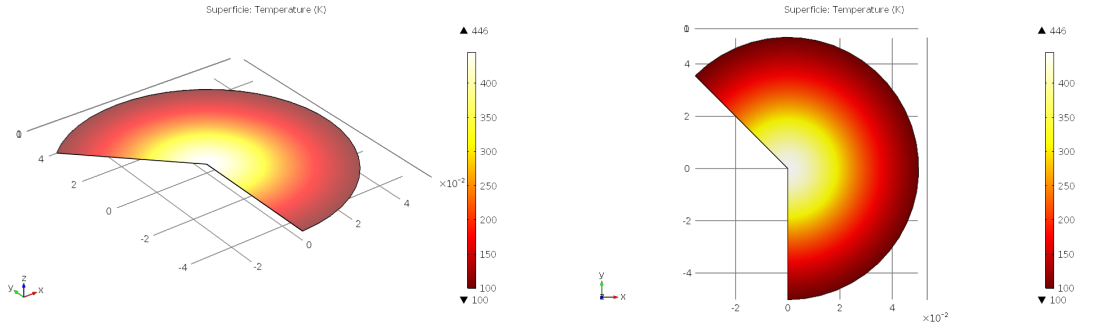

(a) *Perspective view of a Sn/Graphite target representation.*

(b) *Top view of a Sn/Graphite target representation.*

Figure 42: *Temperature distribution in a scaled representation of a Sn target on a graphite substrate.*

Using the geometry reported in figure 42, simulations were performed for the remaining targets as well. As it can be seen in figure 43, there is a difference in the results calculated by two programs; this is particularly true for the Se. However, a part from the latter, the relative error between the two programs is within ±6.6%. Despite the discrepancy, including the full object in the calcula-

tion could provide some information about the influence of the copper sample holder on the whole system.

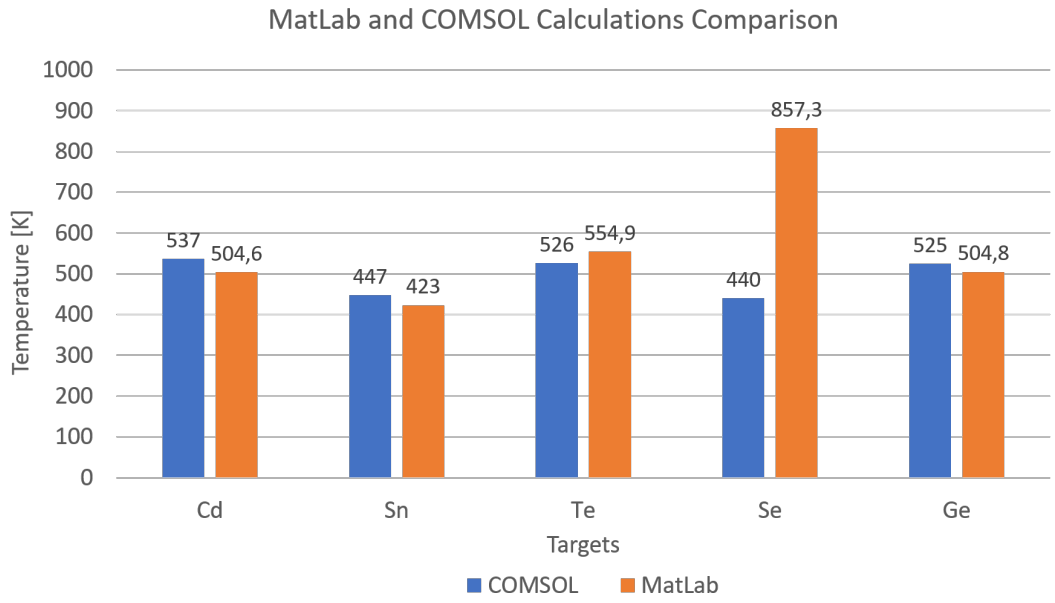

Figure 43: *Comparison between MatLab code and COMSOL; the difference between most of the results is within 6.5%, a part from the selenium, for which it is much more important (about -50%).*

An exploded-view of the complete system is shown in figure 44; it is clear the big difference in dimensions of the involved objects. The target, represented by the small disk 1 cm large, is only 400 nm thick, while the graphite and the copper sample holder are several cm large. There is a difference of 5 orders of magnitude in the dimensions, which surely requires a special attention when establishing the mesh.

COMSOL is able to modify the mesh according to the volume under analysis, making it denser in sharper regions and larger in bulk regions. Albeit extremely useful, this feature is not able to fill the 5 order of magnitude gap. Using a minimum mesh size suitable for the target dimension, i.e. few hundreds of nm, would have led to have an exceedingly vast amount of mesh point in the residual domains. The cost in term of computational power and time would have been excessive.

The issue was resolved by using two distinct meshes: a refined one for the tar-

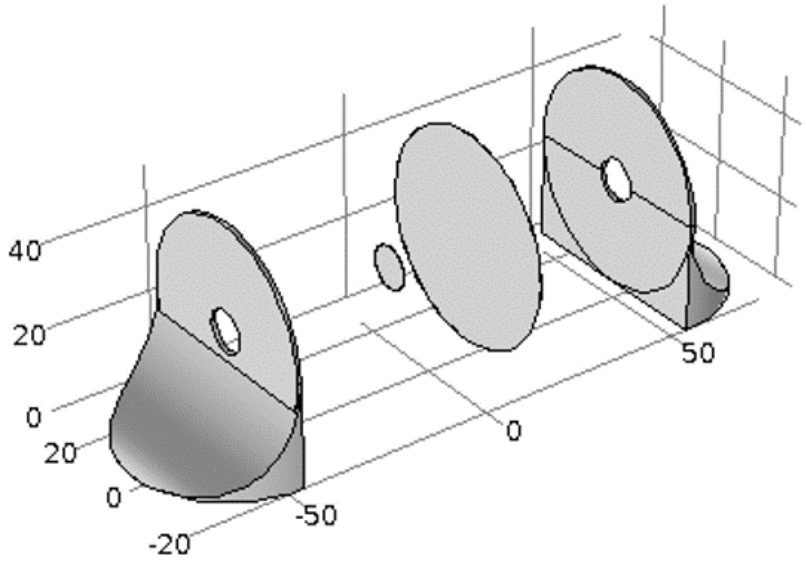

Figure 44: *Exploded view of the entire system simulated in COMSOL environment.*

get and a larger one for the graphite and the sample holder; both of the meshes use a tetrahedral structure. The Heat transfer Module was used to evaluate the thermal evolution of the system; it solves the temperature equation using some user-defined inputs and boundary conditions. In this case, the ion beam was simulated with two heat sources, one associated with the target while the other with the graphite. The two heat sources have a gaussian profile, with a $\sigma = 1$ mm, to reproduce the actual beam; they differ in the deposited power.
The only imposed boundary condition is at the bottom of the geometry, where the sample holder touches the cold finger. This is a fair assumption, since the cryocooler guaratees a cold temperature if dissipating a proper power. This is another substantial difference with respect to the LN_2-based sample holder: with the latter design, the cylindrical symmetry was valid also for the cold boundary. In the new sample holder, designed to fit a cryocooler, the cold sink is at the bottom and not all around. Even though both the graphite and the copper are excellent conductors, the asymmetry may cause some regions of the target to overheat. COMSOL could help also in assessing this issue.

Few designs were studied before arriving at the definitive one, showed in figure 40. Firstly, it was evaluated the effect of the outer diameter on the over-

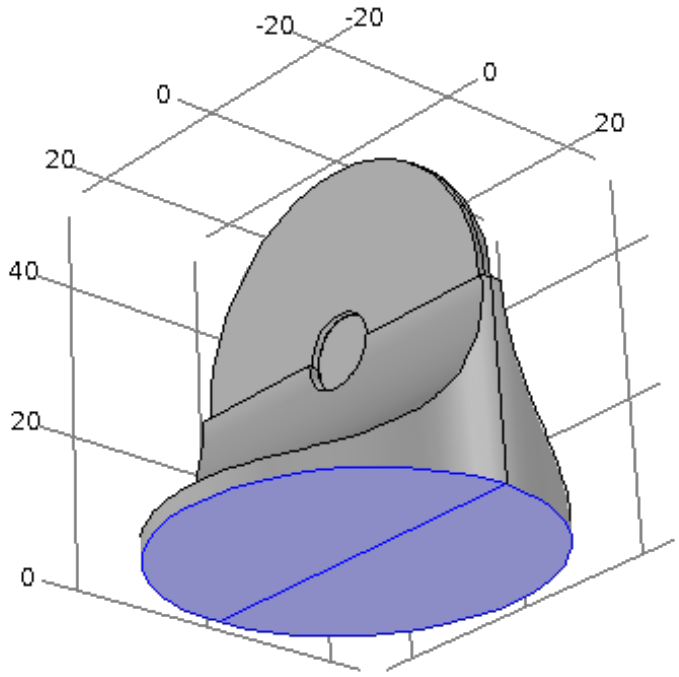

Figure 45: *Picture of the sample holder model, where the cold boundary at fixed temperature, representing the cold finger, is highlighted.*

all cooling efficiency. Two different radii of 7 cm and 5 cm were considered; the two designs are showed in figure 46a and figure 46b, respectively. As it can be seen by looking at the color scales, the temperature is slightly higher in the larger sample holder, while the only advantage in using a larger radius could be a very modest increase in the solid angle for the detectors; considering pros and cons, the 5 cm diameter was preferred. Further decreasing the radius would likely have a small impact on the final temperature, while could be a disadvantage for practical purposes. In fact, the closer the target is to the cold finger, the more the free solid angle is reduced. Moreover, and this is likely a more delicate point, if the target is too close to the cold finger, a slight fluctuation of the beam alignment could damage and activate the copper stage. To avoid this sort of problems, the outer diameter was chosen to be 5 cm.

A similar study was performed for the target diameter, which means the distance separating the hot source (i.e. the beam) from the cold sink (i.e. the copper frame). Unlike the external radius, this parameter is of great impor-

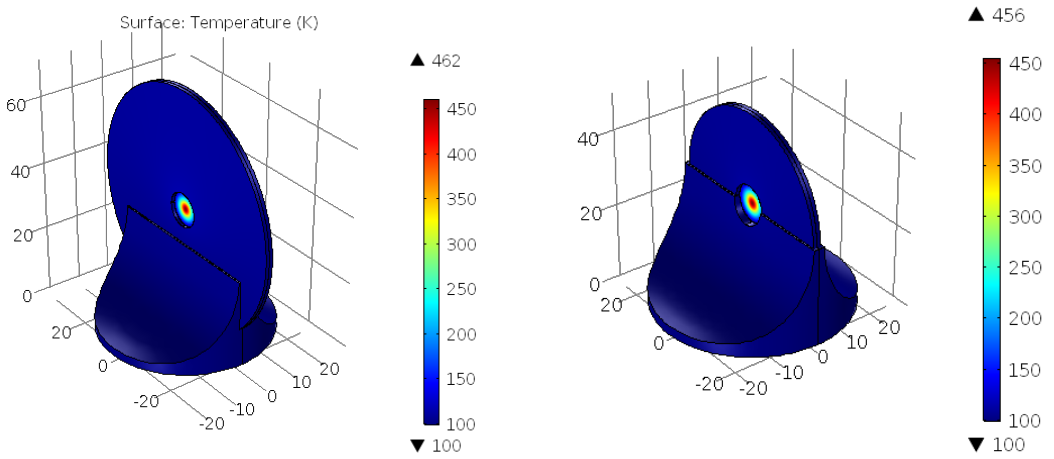

(a) *Design of a sample holder; the diameter of the disk is 7 cm.*

(b) *Design of a sample holder; the diameter of the disk is 5 cm.*

Figure 46: *The comparison between the two designs highlights the poor influence of the width of the disk on the general thermal behavior of the whole.*

tance, as well as the shape of the beam. The combined effect was studied and is summarized in figure 47.

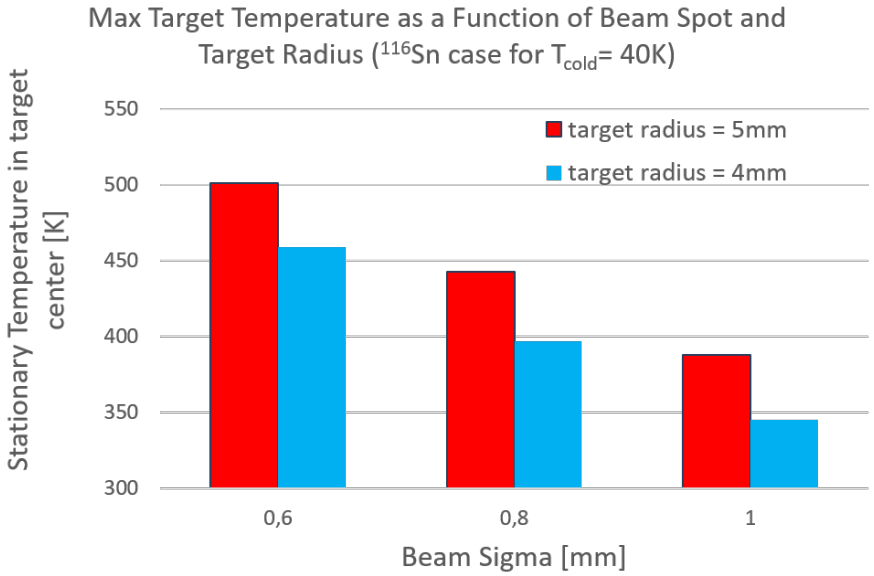

Figure 47: *Effects of the size of the target in relation to the beam spot width. A larger target, as well as a sharper beam spot, leads to a higher temperature in the beam spot.*

A sharper beam means a higher energy density localized in the beam spot, hence a higher stationary temperature. It must be noticed, however, that supposing a beam with a $\sigma = 1$ mm is a safe assumption, since it should be the beam spot of the upgraded apparatus. Also, despite the net gain in the cooling efficiency, it is not advisable to reduce the target size below 1 cm, for precaution reasons: some far tails of the beam could hit the sample holder if the passage is not wide enough. this would cause the generation of spurious events, in addition to collateral damages at the instrumentation.
Finally, once the design had been established, the effect of the asymmetry of the cold sink were evaluated. Noticeably, in every point of the sample holder the temperature does not rise more than 10 K with respect to the temperature of the copper stage. The assumption used for the numerical evaluations, that is a fixed cold temperature at the target boundary, seems to be validated also by COMSOL.

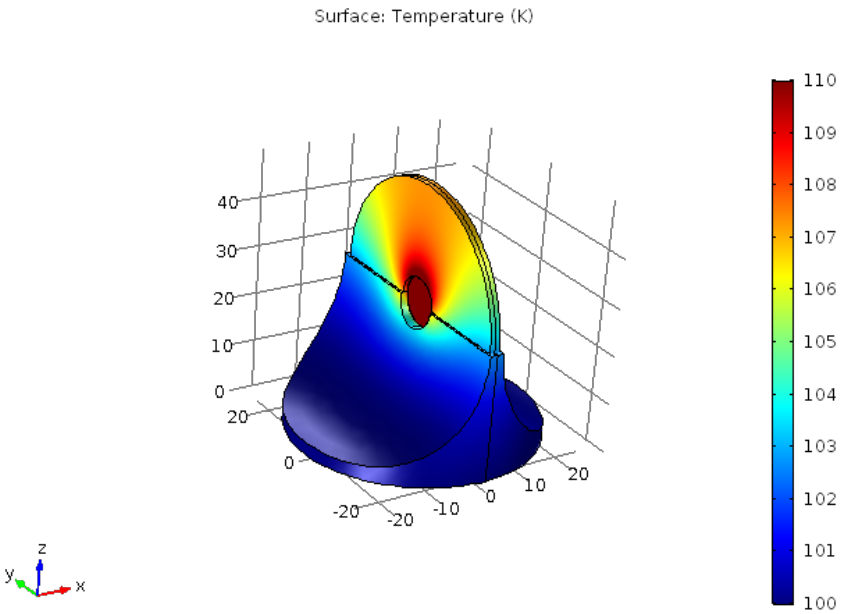

Figure 48: *Temperature of sample holder during irradiation with a* 50 μA ^{18}O *beam. The portion farther from the cold stage is slightly hotter with respect to the rest; the temperature excess, however, is just* 10 *K and does not influence the working efficiency of the system.*

The analysis performed on the design of several parameters allowed to determine the sample holder shape which best fits the requirements and the

constrains. So, using the definitive design, the same study was performed on the other targets, to obtain something similarly to the initial comparison (figure 43).
In figure 49 is showed a comparison between a MatLab-like geometry and a full cooling system for a Ge target.

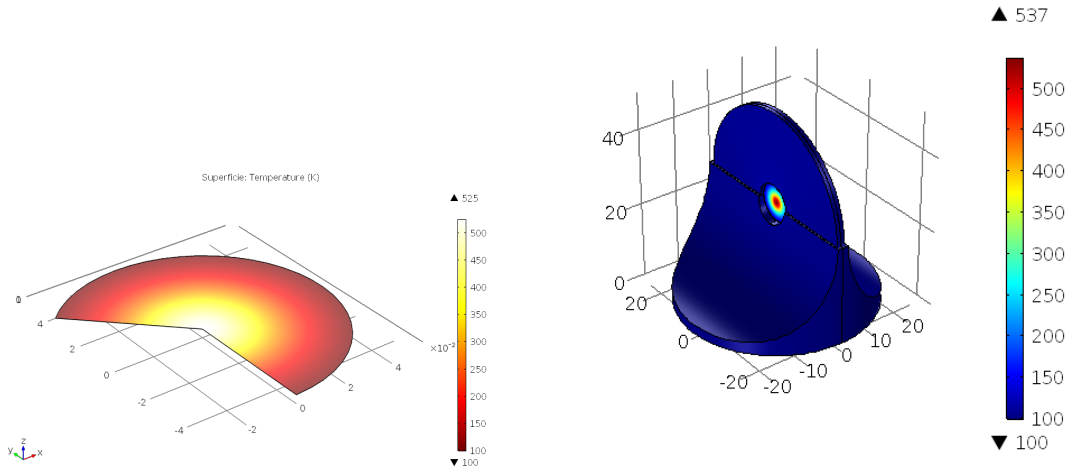

(a) *Stationary state of a Ge target for a MatLab-like geometry.*

(b) *Stationary state of a Ge target encased in the copper sample holder.*

Figure 49: *A comparison between a system in which the boundary fixed temperature is set at the target limit (fig. a) and one in which the cold sink is supposed in the cryocooler copper stage (fig. b). The copper sample holder efficiently dissipate the heat, accounting for only* 12 *K more in the beam spot region.*

The influence of the copper sample holder for each target is reported in figure 50; it is quantified in about $9 - 12$ K on the final temperature.

The results obtained with COMSOL are mostly compatible with the numerical code results; in particular, COMSOL tends to underestimate the outcome, with respect to the numerical code, if the target material has a poor thermal conductivity, like Te and Se. In the latter material, which has an extremely low thermal conductivity, the discrepancy exceeds 400 K. Regardless the differences in the final temperatures, COMSOL major contribution remains the capability to evaluate the influence of copper sample holder. The asymmetric design of the cold sink does not pose any particular issues, while the graphite is kept basically at the cold sink temperature. The presented results are computed for a cold temperature of 100 K, but cryocoolers are able to reach far lower temperatures. The final temperature directly depends on the cold sink

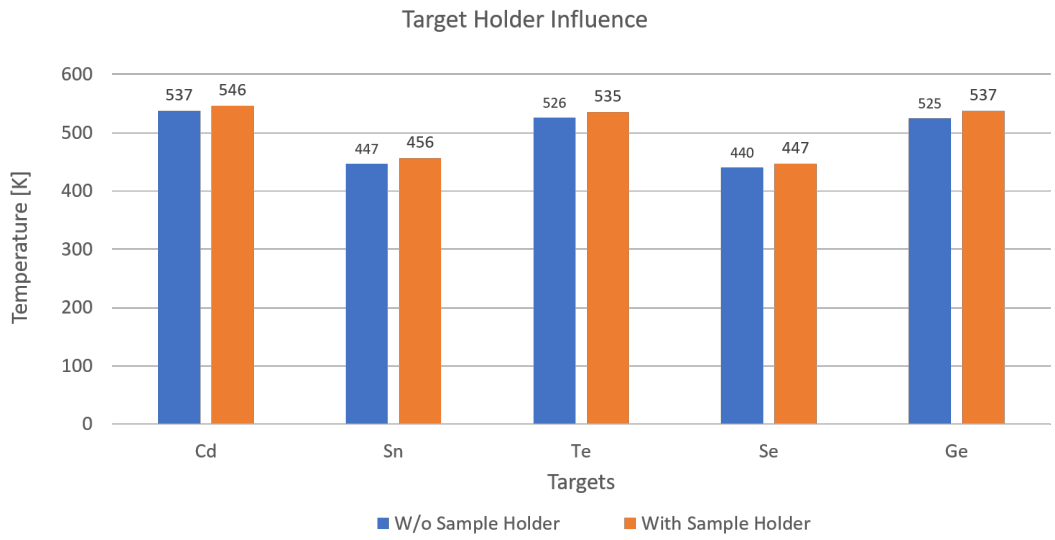

Figure 50: *As can be appreciated in the plot, the sample holder accounts for an increase in the final temperature of just few K.*

temperature T_{cold}; assuming that the thermal properties of copper and graphite do not change with the temperature, lowering the T_{cold} of a certain quantity ΔT would also lower the beam spot temperature of the same quantity.

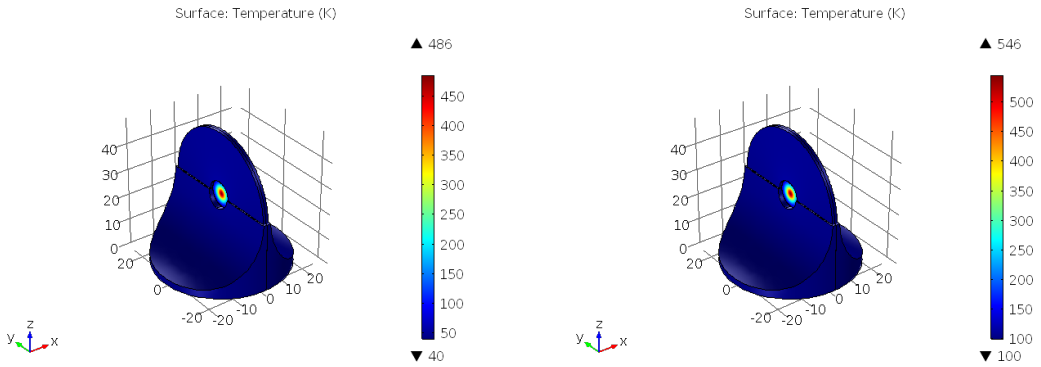

(a) *Cadmium target simulation with* $T_{cold} =$ 40 *K.*

(b) *Cadmium target simulation with* $T_{cold} =$ 100 *K.*

Figure 51: *Supposing temperature-independent thermal properties, reducing the base temperature of the cold stage lowers of the same quantity the maximum reached temperature.*

In reality, the thermal properties of copper and graphite are temperature dependent [53, 54]. Both of the materials thermal conductivity increase in the considered temperature range; HOPG can double its in-plane thermal conductivity at about 100 K. At 30 K, highly pure copper thermal conductivity reaches 3000 $Wm^{-1}K^{-1}$. Most likely, since the involved materials are enhanced by the low temperature, accounting for the real thermal properties would led to better results; however, a study on the HOPG and the copper which will be used is yet to be done. Also, the graphite properties will be different in the beam spot and under the copper, complicating a rightful evaluation. Using standard values for the calculation is likely more cautious.

6

PRODUCTION AND CHARACTERIZATION OF TIN AND TELLURIUM TARGETS

Soon after the positive outcome of the first numerical calculations, the experimental activity started. Graphite is not an usual substrate for deposition, as suggested by the poor existing literature on the argument. Moreover, the targets used in NUMEN must be made of pure isotopes, some of which are particularly costly and rare [55]. Those two characteristics alone prevent the usage of certain common deposition techniques, such as plasma sputtering; the available quantity of material can be as low as few mg, preventing the realization of a sputtering target, which cost would be impractical. Considering the scarceness, the peculiarity and the demands for the target uniformity, Electron Beam Deposition (EBD) was chosen for the target production.
The core of an EBD system is the electron source, a sort of box which hosts the electron gun, the magnets, the crucible and the cooling system. The electron gun is the electron emitter, which usually works for thermionic emission from a filament; the electrons are afterward bent by a permanent magnet or an electromagnet; after a 270° turn, the electron beam impinges into the hearth in which the material is contained; finally, a cooling system prevents the hearth melting.

The amount of material to be evaporated can be extremely small, depending on the crucible size; this feature proves to be extremely handy if rare isotopes must be evaporated. Theoretically, any element can be evaporated with an electron beam, which deposits huge amounts of energy in the beam spot. Even high melting point material, such as Mo, can be easily evaporated. Depending, not solely, on the instrument, an EBD system can achieve a film uniformity of $\pm 5\%$, with an excellent efficiency in the deposition target usage.
As already mentioned, HOPG is poorly suited as substrate; this special kind of graphite is in fact composed by highly aligned graphene flakes, which make the surface both chemically inert and atomically flat. These characteristics require additional care in obtaining a flat and uniform deposited target.
Two materials were chosen to start the study: tin and tellurium.

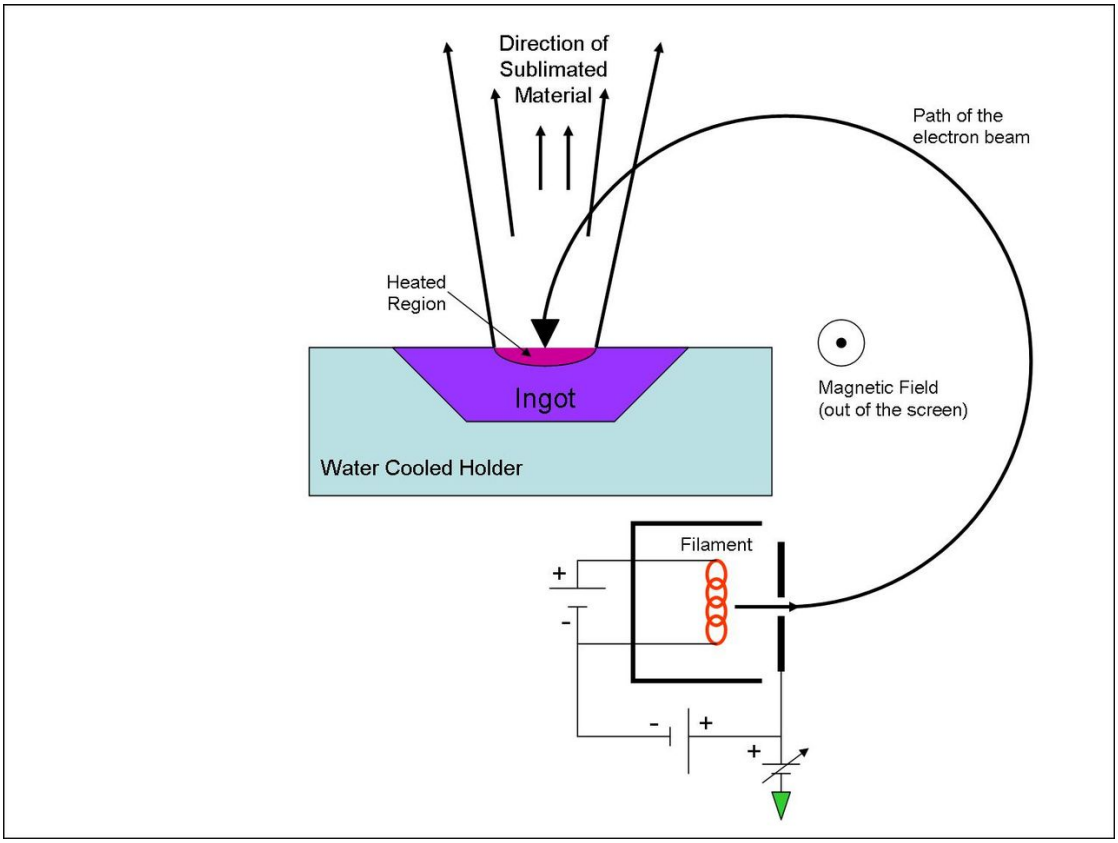

Figure 52: *General scheme of an EBD electron source [56].*

6.1 TIN TARGET DEPOSITION

Tin is a quite tricky material to deposit; if the deposited film is less than 1 μm thick, it tends to form spherical droplets. Increasing the thickness, the droplets coalesce in bigger islands and this behavior can be observed both on SiO_2 substrate [57] and on graphite [58]. Tin is in fact used as a Scanning Electron Microscope calibrating sample thanks to its characteristic spherical grains on graphite.

As it can be easily deduced, the way a tin film grows impedes the formation of a smooth target. To obtain such a target, a careful study was carried out. The key parameters, which were initially explored, were the substrate temperature during the deposition and the post-deposition annealing temperature.
In the production of samples, the 10 μm HOPG graphite was chosen over a thinner one for cost reasons. Panasonic 10 μm HOPG is rather inexpensive

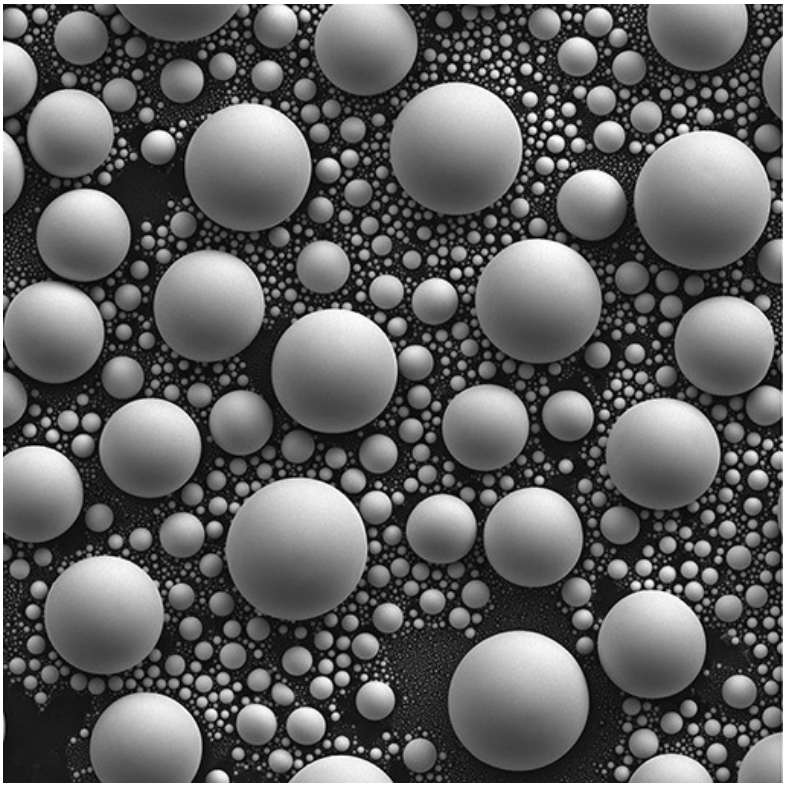

Figure 53: *Tin spheres used as calibration sample for SEM [58].*

and can be used in the production of many expendable samples; moreover, the physical characteristics are very similar to those of thinner and more expensive HOPG sheets. However, the 10 μm thick graphite is quite tricky to handle, because of the thickness and the presence of an adhesive on the back. For this reason, the initial deposition tests were done using a thicker graphite, 65 μm, which is adhesive free. The first deposition was performed at room temperature; the sample was subsequently analyzed with a Field Emission Scanning Electron Microscope (FESEM), which allows to obtain a quick feedback on the produced film. The FESEM, hosted in the laboratories of the Department of Applied Science and Technology of the Polytechnic of Turin, is a Zeiss Merlin [59]; the instrument is able to magnify an object up to one million times and has a resolution of 0.8 nm. An Energy Dispersive X-ray Spectrometer (EDS) is embedded in the same instrument, allowing non destructive elemental analysis.

6.1.1 *The 65 μm Graphite Substrate*

The deposition at room temperature served as a starting point, to have a first idea of how the material would respond to the graphite substrate. The top image of the sample, reported in figure 54, highlights the growth of numerous grains some μm in size, which coalesce into a complex network. Albeit the nominal thickness was set to 500 nm, the side picture in figure 55 reveals that the height of the grains far exceeds this value. The film is highly porous and non homogeneous, due to the fusion of big crystals.
Given the growth mechanism, one option to obtain a more uniform film is to grow bigger grains, in order to reduce the number of coalescence points and the underlying channels. To this end, for the following samples, the deposition rate was kept low and the substrate was heated during the deposition. Providing energy through substrate heating favors the mobility onto the substrate of impinging particles, promoting the accretion of already existing grains. However, grains can be enlarged also by post deposition heat treatment, such as annealing. The annealing process consists in heating the sample for a certain time to allow minor rearrangement of the film structure. Before producing another sample, the first batch was annealed at 175 C for 24h, 48h and 72h. FESEM images of the samples, reported in figures 56, 57 and 58, show little improvement in grain size, while the uniformity did not change appreciably.

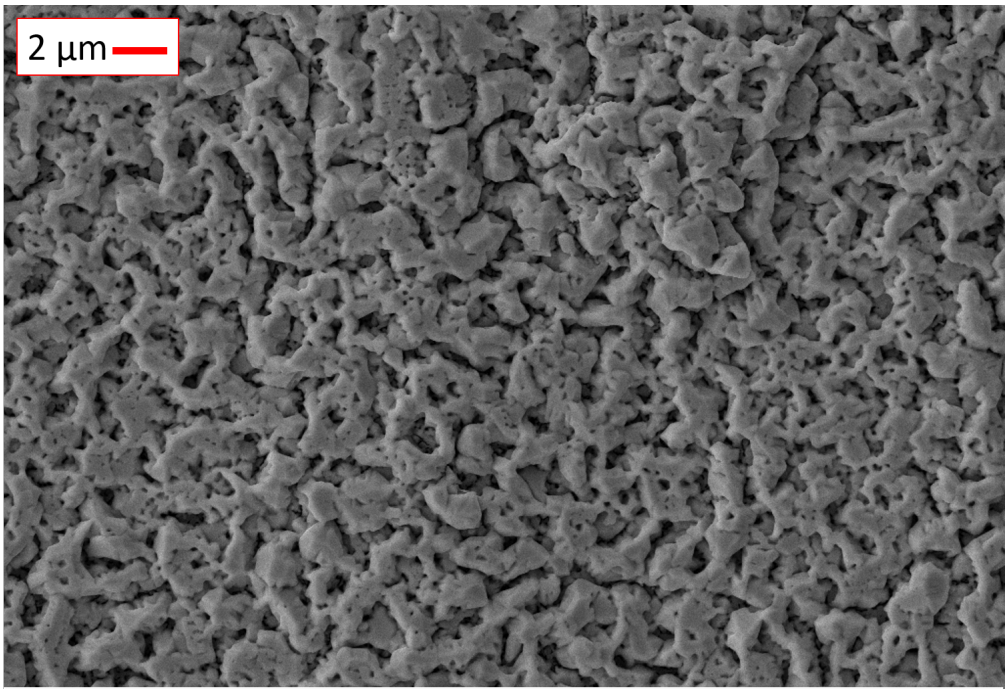

Figure 54: *Top view of a Sn sample, nominal thickness of* 500 *nm, deposited at room temperature.*

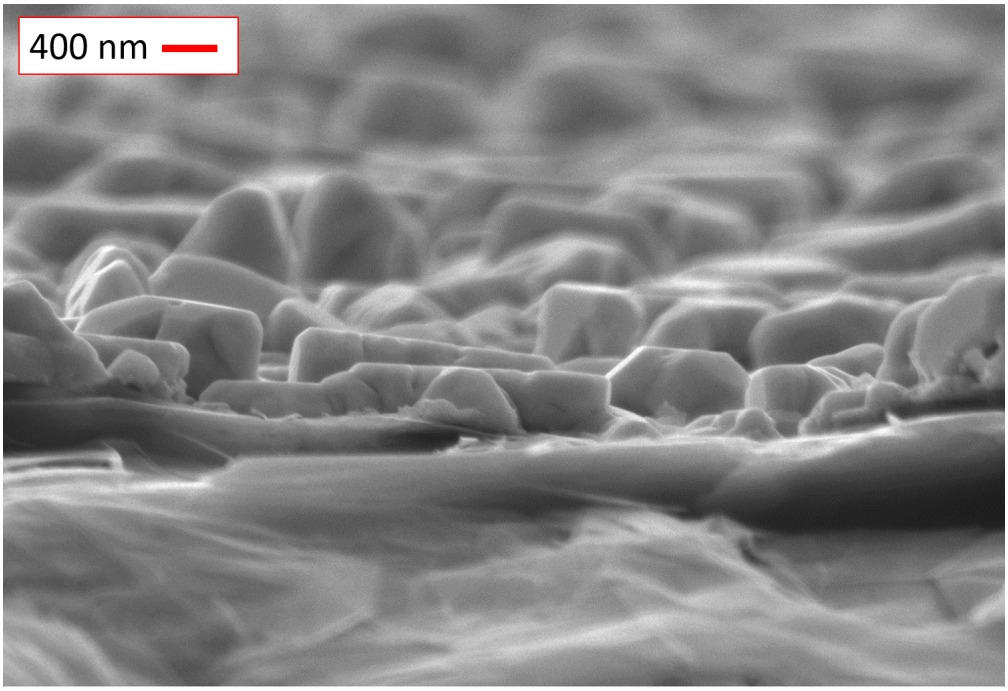

Figure 55: *Side view of a Sn sample, nominal thickness of* 500 *nm, deposited at room temperature. The flat, unstructured lower region is the graphite substrate, peeled by the cut necessary for side imaging.*

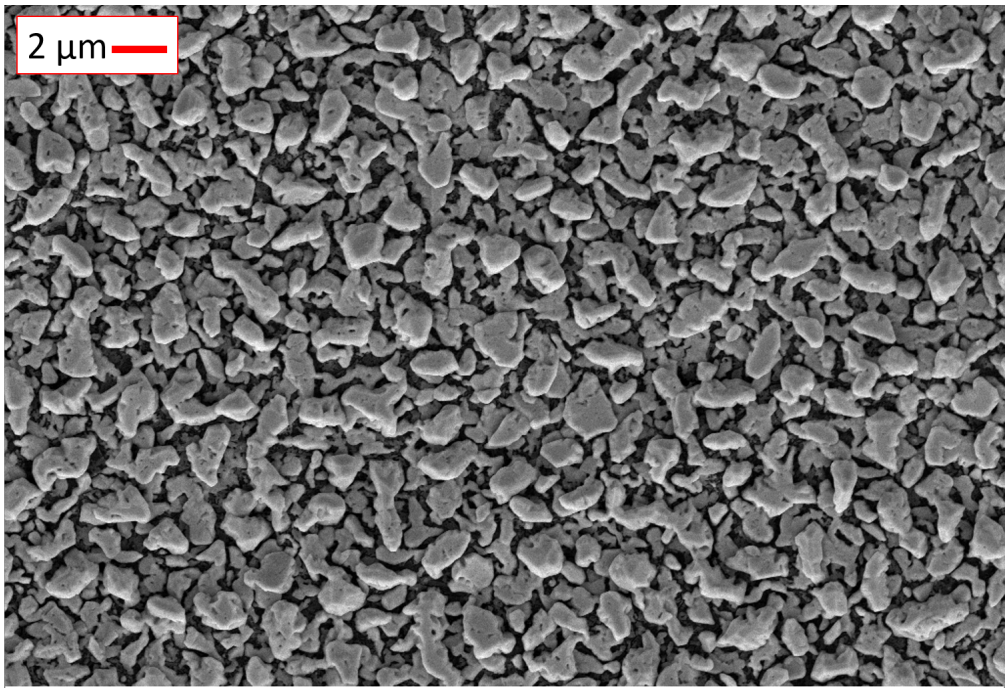

Figure 56: *Tin sample deposited at room temperature after 24h annealing at* 175 *C.*

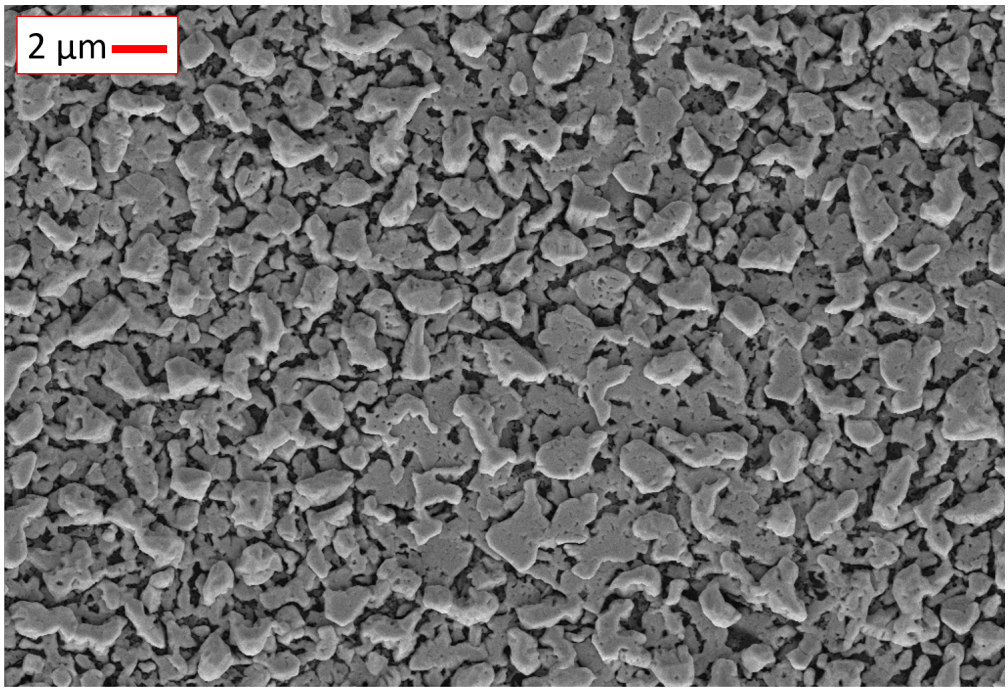

Figure 57: *Tin sample deposited at room temperature after 48h annealing at* 175 *C.*

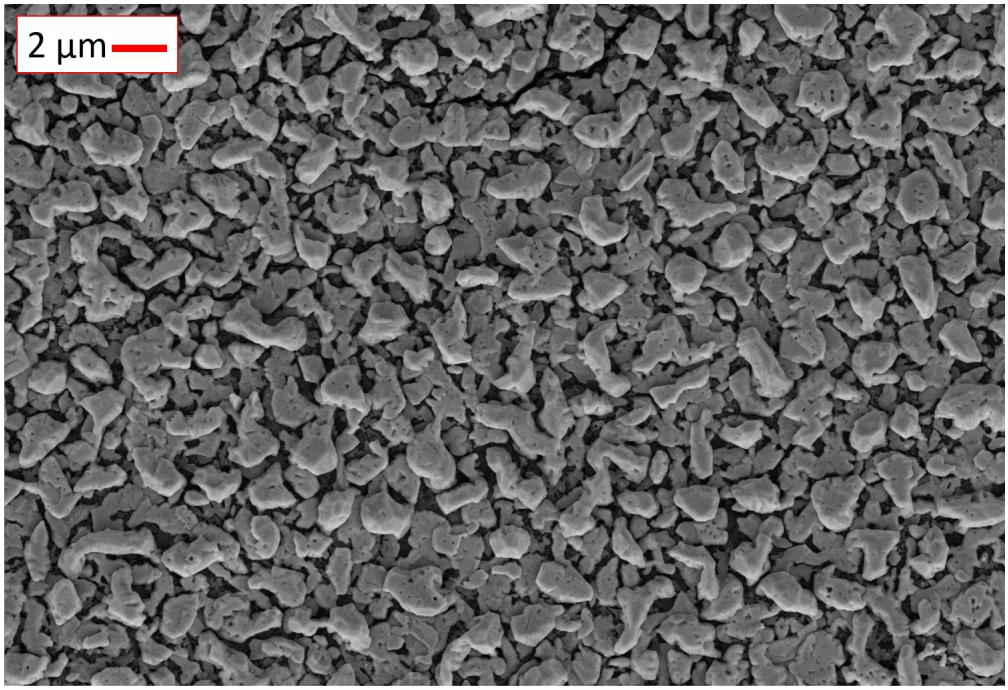

Figure 58: *Tin sample deposited at room temperature after 72h annealing at* 175 *C.*

The next sample was then deposited at 150 C. Compared to the previous one, this sample, showed in figure 59, appears much smoother. The grains seem to have grown bigger and more compact, the presence of pores and cavities being strongly reduced. Although the single crystals are more tightly joined, the space between disjointed groups are quite large and deep. Side imaging of the sample revealed that also the uniformity in height improved noticeably. The effective thickness appears greater than the nominal one, which is again 500 nm. The precise evaluation is prevented by the partial coverage of the substrate boundary. Figure 60 has been taken at the limit of the sample to avoid to cut it, a procedure which is particularly complicated and destructive if it involves a flexible graphite substrate.
This sample underwent a series of annealing treatments similar to those used for the room temperature sample, i.e. annealed at 175 C for 24h, 48h and 72h. The benefits coming from such treatment seem to be negligible, with no appreciable changes among the different time steps (figures 61, 62, 63). The same procedure were repeated, for a second batch, at a slightly higher temperature, 185 C, for the same time steps. The results were, once again, of negligible importance.

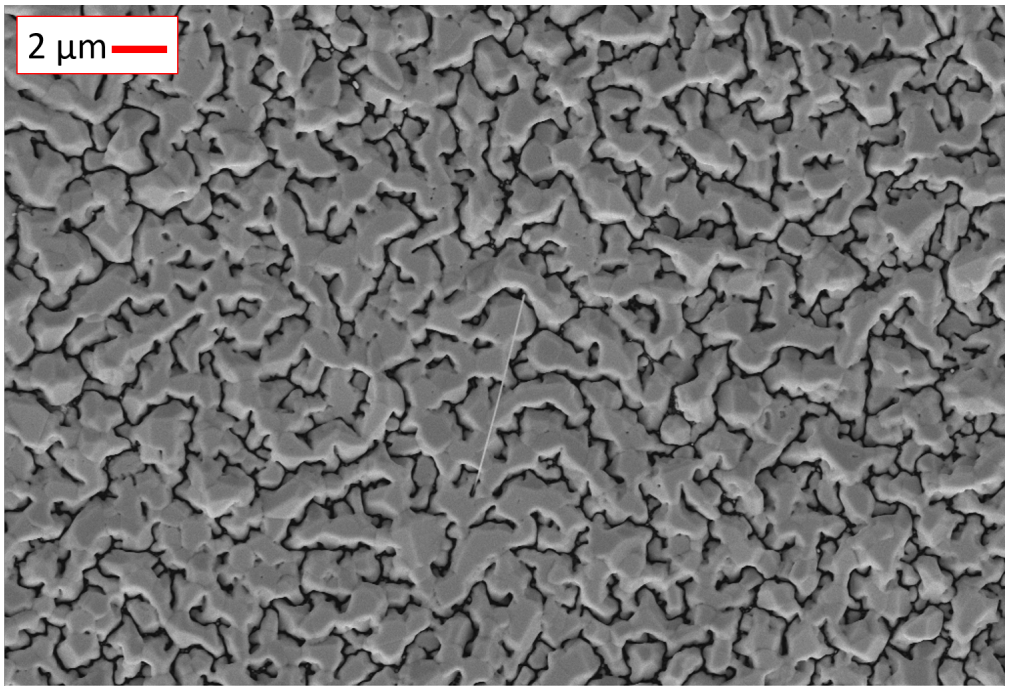

Figure 59: *Top view of a Sn sample, nominal thickness of* 500 *nm, deposited at* 150 *C.*

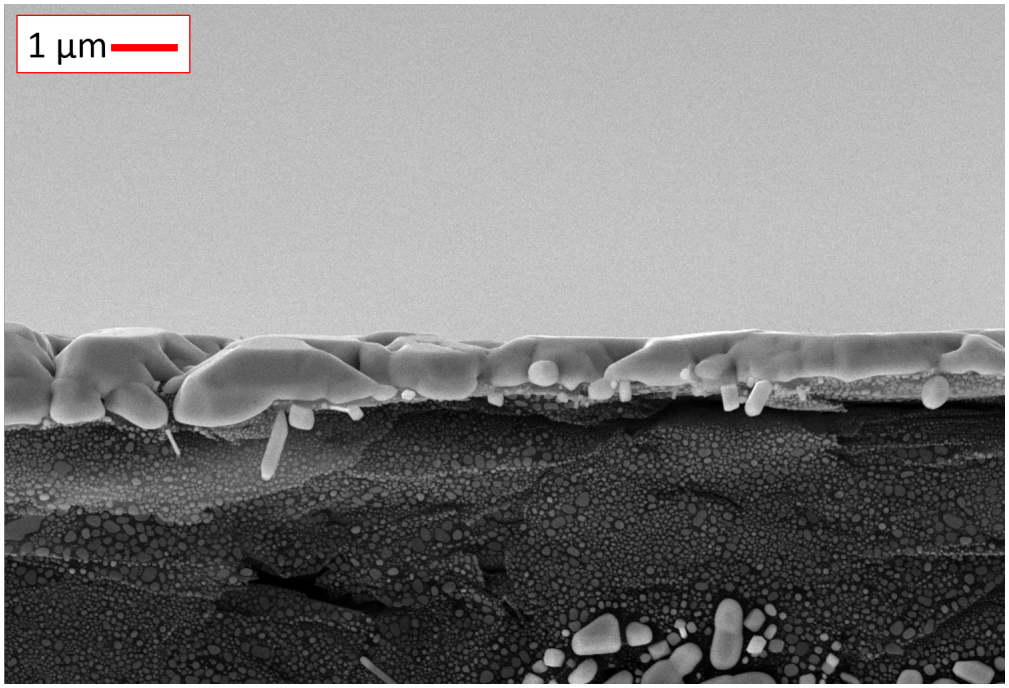

Figure 60: *Side view of a Sn sample, nominal thickness of* 500 *nm, deposited at* 150 *C. The surface appears much smoother with respect to the sample deposited at room temperature. The tin seems to spill over because the picture was taken at the boundary of the sample, in order to avoid damages due to cutting.*

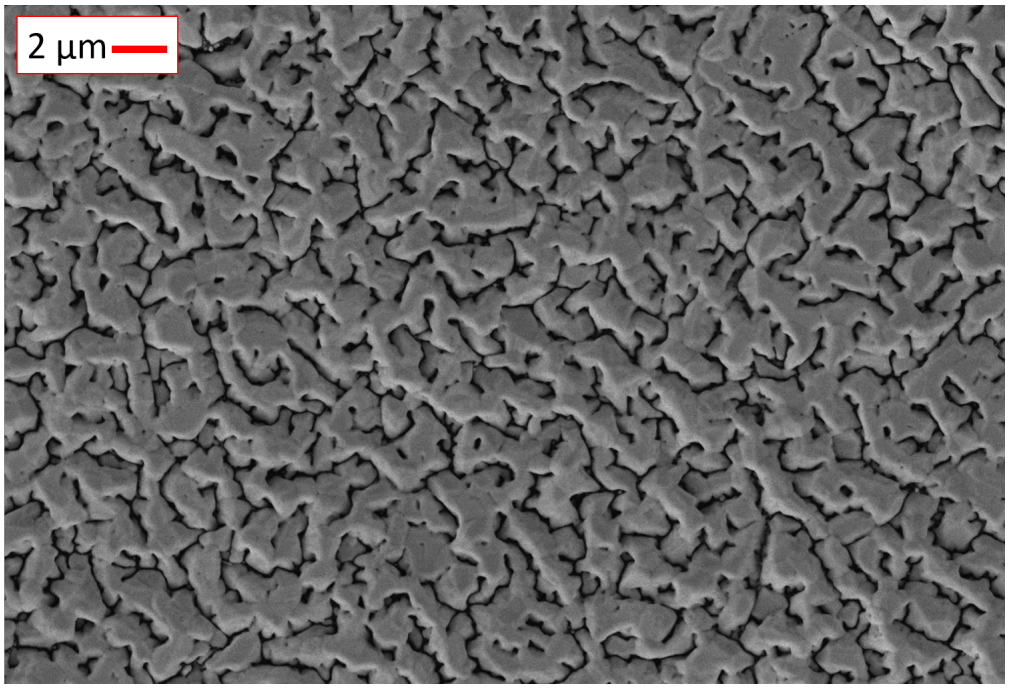

Figure 61: *Tin sample deposited at* 150 *C after 24h annealing at* 175 *C.*

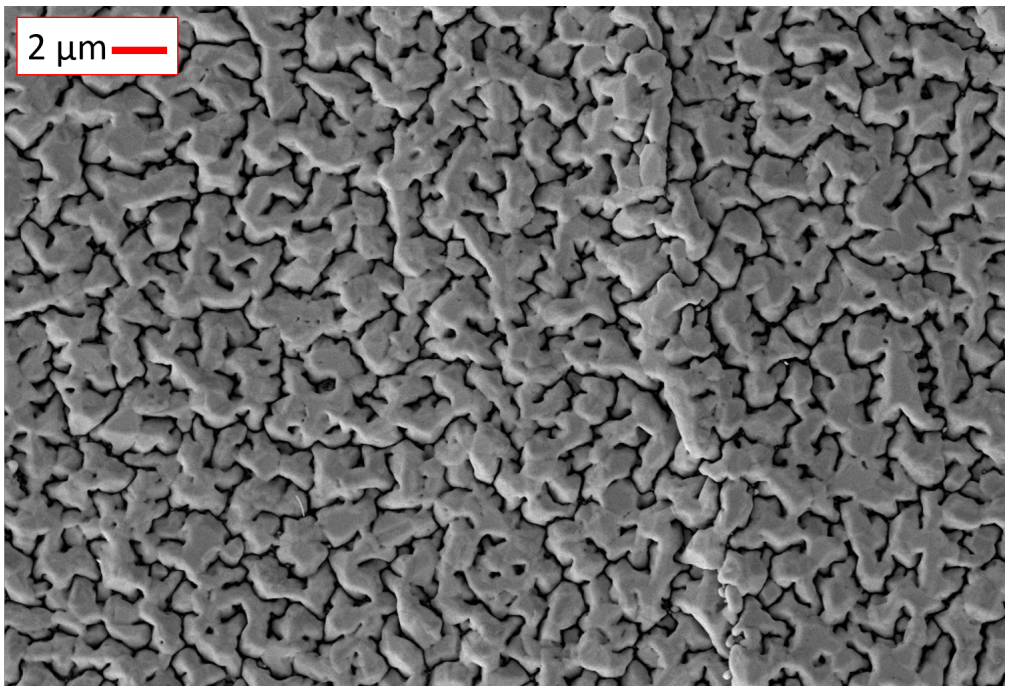

Figure 62: *Tin sample deposited at* 150 *C after 48h annealing at* 175 *C.*

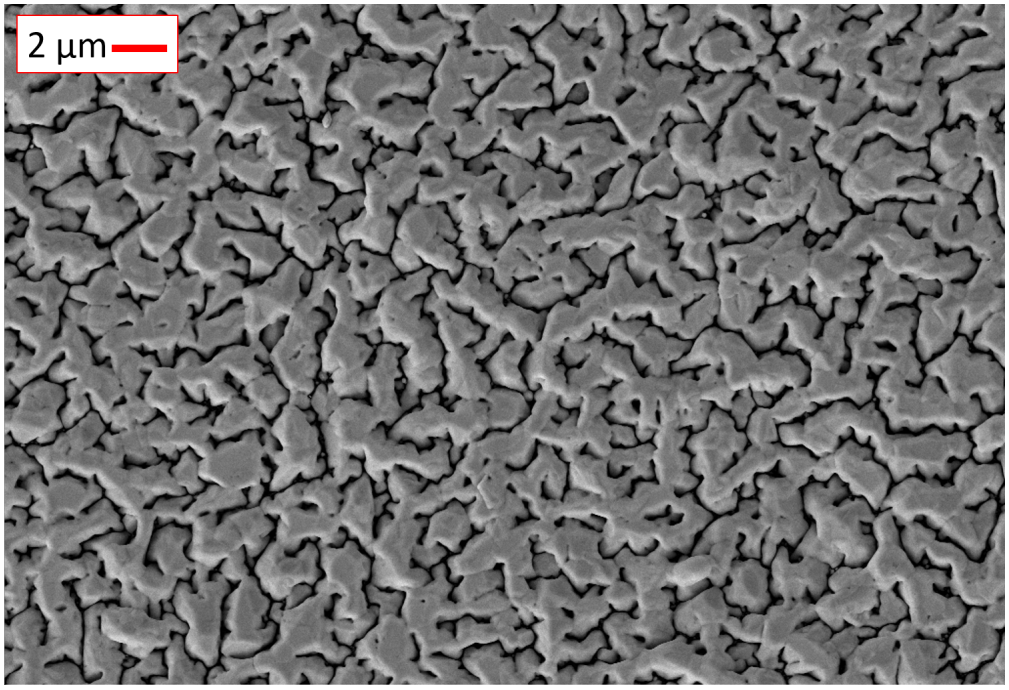

Figure 63: *Tin sample deposited at* 150 *C after 72h annealing at* 175 *C.*

The net improvement obtained by heating up the substrate pointed the direction for having a smoother target. The deposition temperature was increased to 175 C to try to further improve the results obtained at 150 C. In this batch was also explored the influence of the thickness, producing some samples with a tin layer of 400 nm (figure 64) and some others with a tin layer of 500 nm (figure 65). The two samples appear quite different: while the 400 nm thick one seems an improvement with respect to the previous batches, the 500 nm one is a firm backward step. The thinner sample (figure 64) shows a very good grain merging, with thinner inter space between disjointed parts and some sparse smaller grains. The overall aspect is flat and compact.

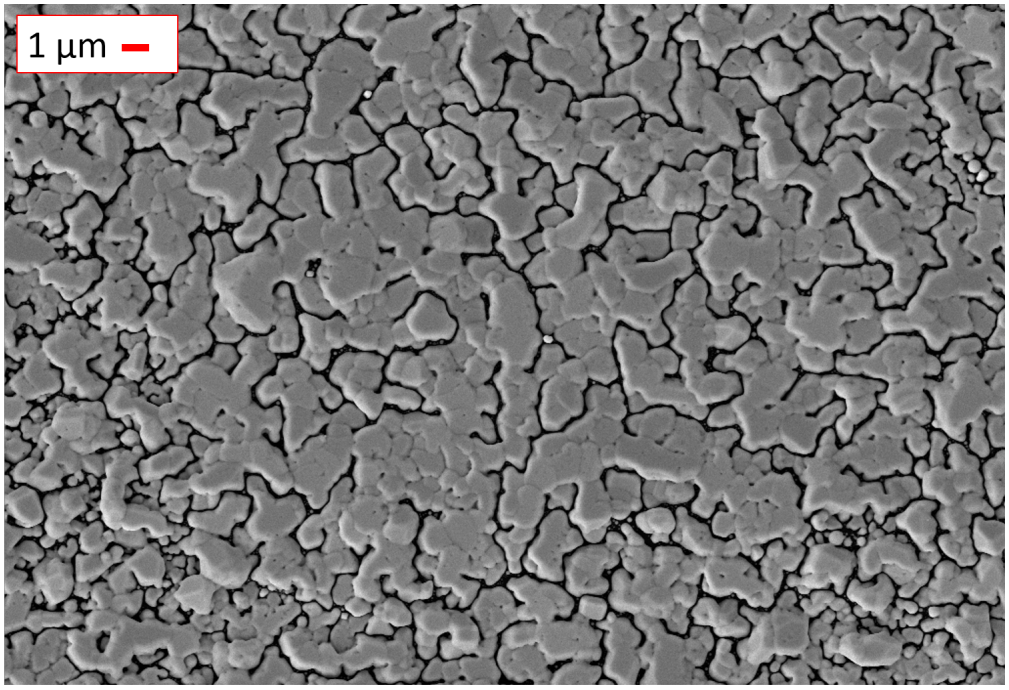

Figure 64: *Top view of a Sn sample, nominal thickness of* 400 *nm, deposited at* 175 *C.*

The situation differs in the second sample (65); the 500 nm thick layer seems formed by two phases: a compact background, formed by closely packed small grains, onto which bigger and sparse structures grew. An appearance which seems to be reproduced by the following annealing treatment (figure 66); given the scarce influence of the procedure for temperature up to 175 C from 24h to 72h, both of the samples were annealed at 195 C. This time, the annealing process worsened the film quality, making the 400 nm thick sample to resemble the thicker one (figures 67 and 68). The grains of the annealed 500 nm thick

sample seem more interconnected, but the film as a whole appears strongly non homogeneous.

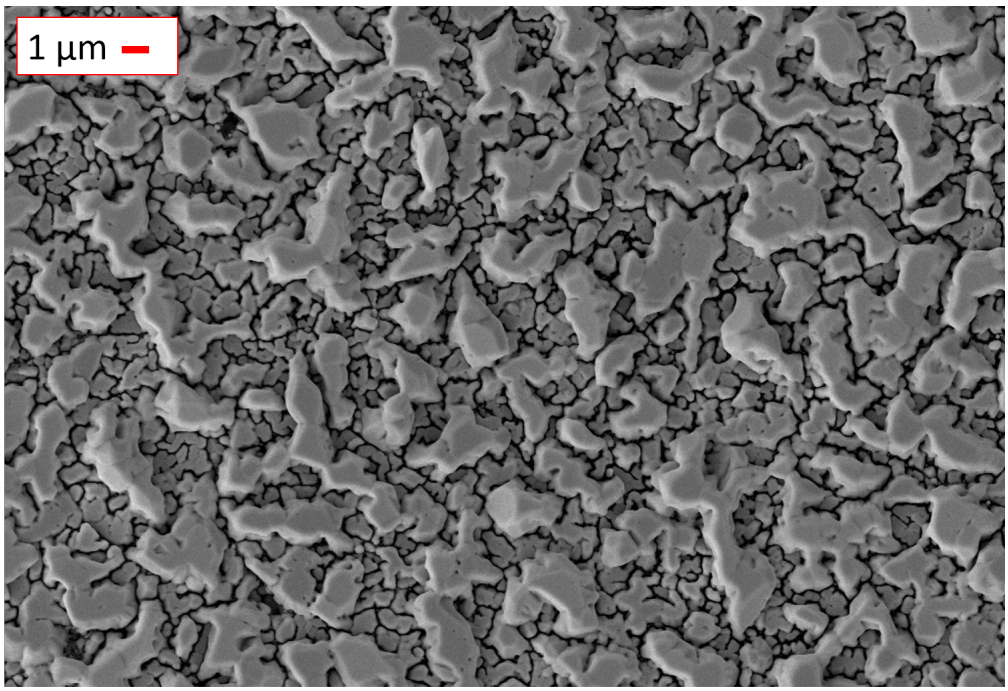

Figure 65: *Top view of a Sn sample, nominal thickness of* 500 *nm, deposited at* 175 *C.*

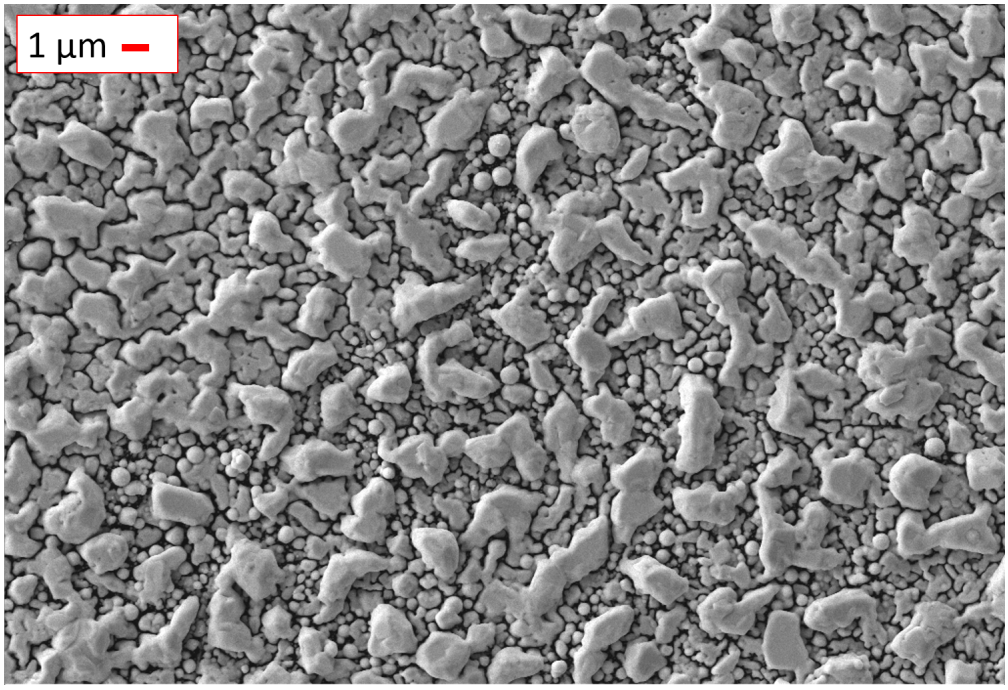

Figure 66: *400 nm thick tin sample deposited at* 175 *C after 24h annealing at 195 C.*

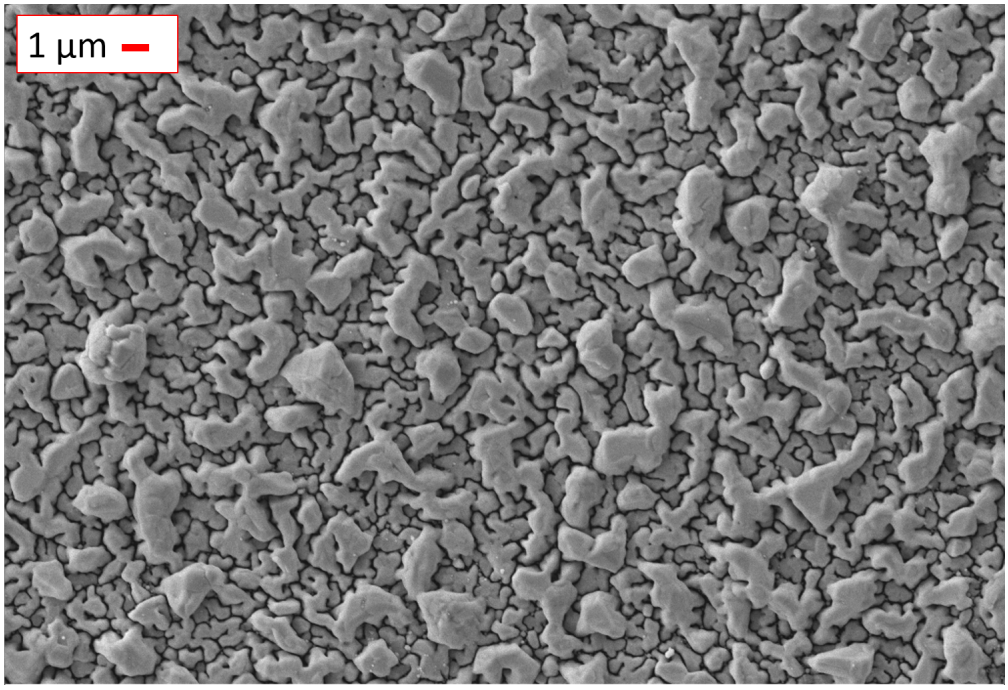

Figure 67: *500 nm thick tin sample deposited at* 175 *C after 24h annealing at 195 C.*

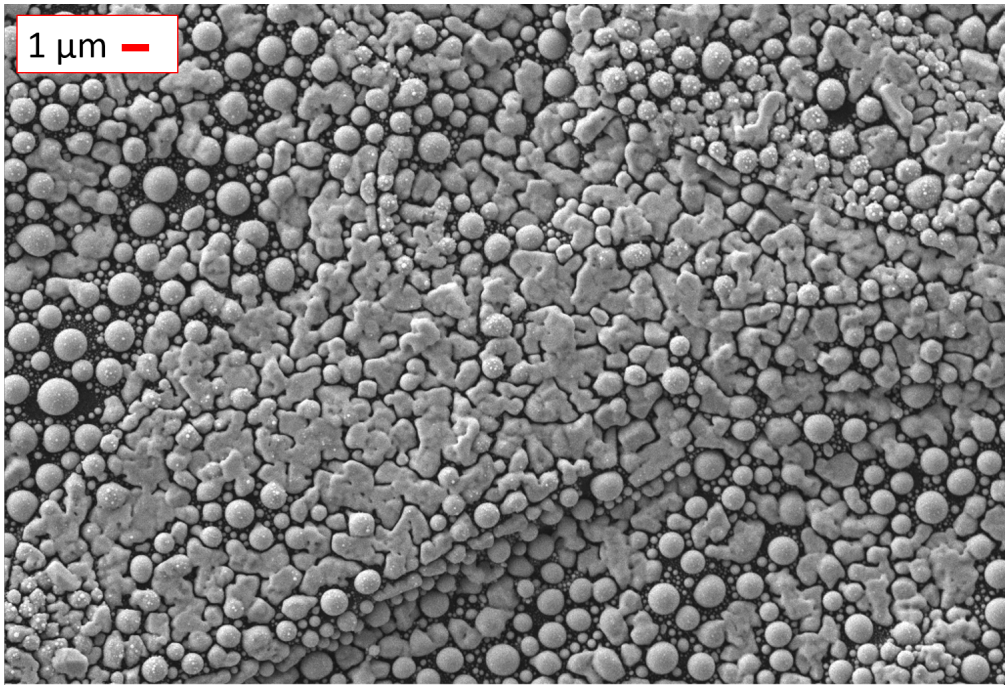

Figure 68: *Tin sample,* 400 *nm thick, deposited at* 200 *C.*

A final attempt was made heating the substrate at 200 C, to see the film structure if deposited at a temperature too close to the melting point (figure 68). While in some regions the grains are well merged, tin droplets cover the major part of the substrate, which is exposed in several spots. The exposure of the graphite can be due marginally to a partial re-evaporation of the tin, but mainly to the droplets formation, which deplete the surrounding area. The formation of the spheres can be a clear signal of reaching an excessive temperature during the deposition.

The batch of samples produced using a thicker graphite served to understand the processes and the techniques useful for depositing a smooth film of tin on graphite. After a fair number of trials, the results obtained for a 400 nm thick sample, deposited at 175 C, were satisfying from the point of view of homogeneity and compactness. The annealing treatment resulted to be superfluous, being at best irrelevant, at worst counterproductive. Henceforth, it was abandoned. The experimental procedure was then transposed to the production of samples on 10 μm thick graphite substrates.

6.1.2 *The* 10 μ*m Graphite Substrate*

The physical characteristics of the 65 μm thick graphite are similar to those of the thinner 10 μm one, but not the same. They differ slightly in density, thermal conductivity, mechanical resistance and other characteristics. One could then expect a similar behavior when used as substrate. The first attempt with the thin graphite was made at 175 C, which was the temperature which gave the best results in the previous batch.
The results in this case were quite different; instead of a compact film, the tin layer is here composed by small, irregular drops smaller than 1 μm; the substrate is clearly visible in the surroundings of the droplets. The film showed in figure 69 resembles somewhat the one deposited at 200 degrees with the thicker graphite (figure 68). If, as it seems, the surface of the thinner graphite is more inert with respect to the 65 μm thick one, the optimal deposition temperature could be shifted downward. The second sample was then deposited at 150 C, but again the obtained film was not uniform (figure 70). Even though the film is still composed by drops, in this case they are much more regular, being almost perfectly spherical. Their size ranges between few hundreds of nm up to 1 μm.

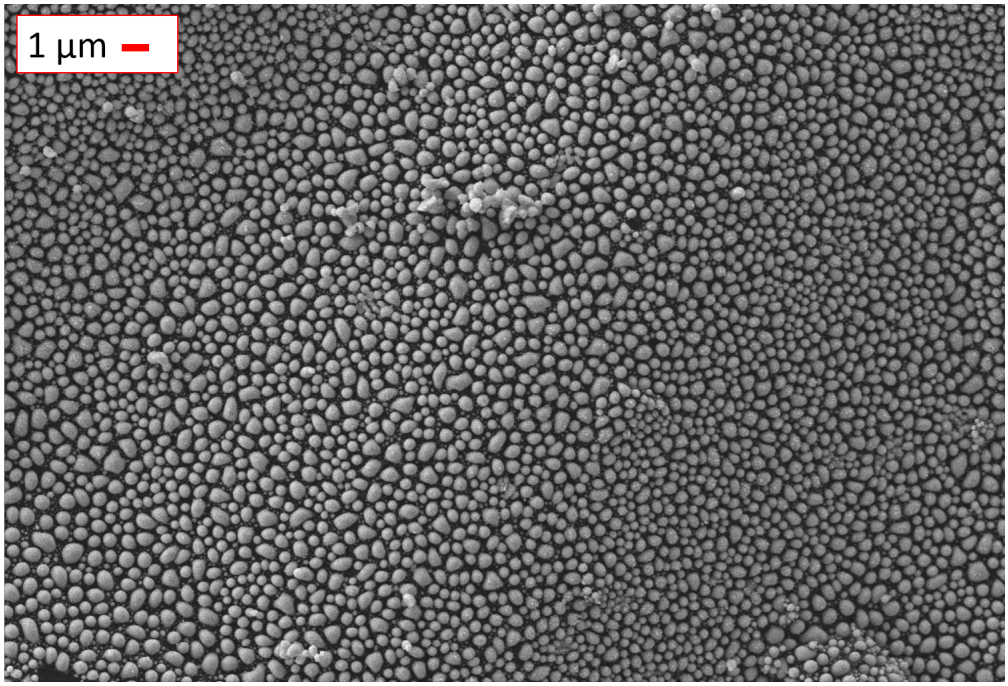

Figure 69: *Top view of a Sn sample, nominal thickness of* 400 *nm, deposited at* 175 *C on a* 10 *µm graphite substrate.*

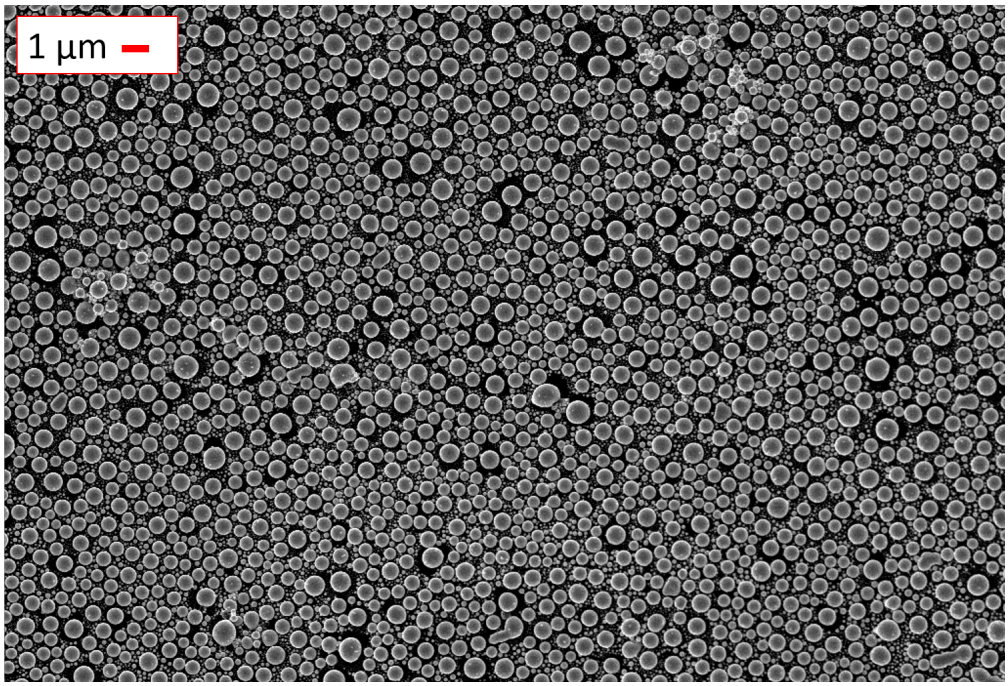

Figure 70: *Top view of a Sn sample, nominal thickness of* 400 *nm, deposited at* 150 *C on a* 10 *µm graphite substrate.*

Albeit formed by spheres, their distribution is regular and constant, without the coexistence of contiguous and interrupted regions which could be observed in figure 68. This sample closely resemble the typical SEM calibrating sample showed previously in figure 53. A side image of the sample could be extremely useful to provide some more information about the deposition. In fact, in the magnified image reported in figure 71, it is possible to observe that the tin drops are indeed almost perfect spheres. A part from being aesthetically pleasant, this fact underlines the poor interaction between substrate and film. More than half of the sphere emerges from the substrate, indicating a contact angle lower than 90◦. Such angle is identified between the substrate plane and the tangent to the drop surface; the more its value is closer to 0◦ the less the substrate is wet by the material. In this case, the graphite is quite refractory to the tin, so merely adjusting the deposition temperature may not be sufficient to obtain a good film. More tests at different temperatures were performed anyway. A significant change in the structure was in fact obtained with the substrate at 140 C; the tin spheres disappeared and a more complex film was created instead.

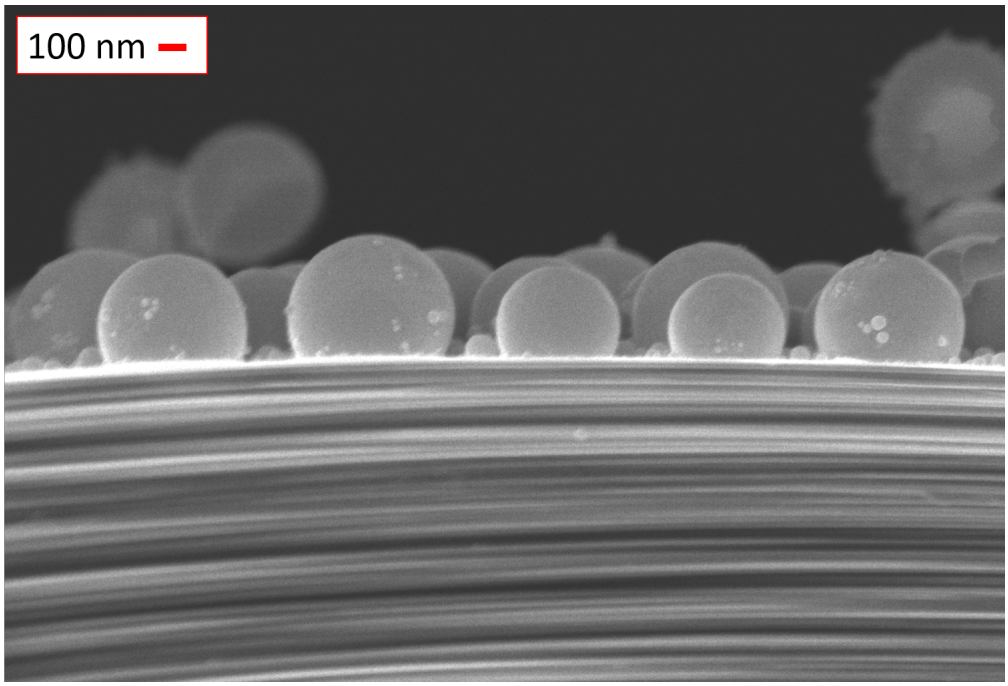

Figure 71: *Side view of a Sn sample, nominal thickness of* 400 *nm, deposited at* 150 *C on a* 10 *µm graphite substrate.*

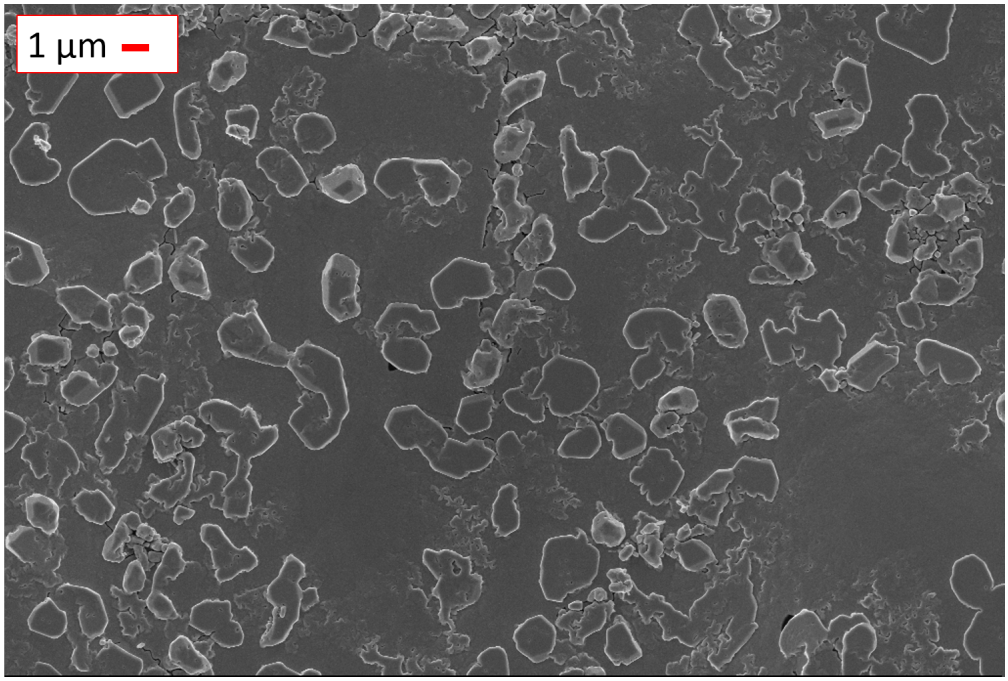

Figure 72: *Top view of a Sn sample, nominal thickness of* 400 *nm, deposited at* 140 *C on a* 10 *µm graphite substrate.*

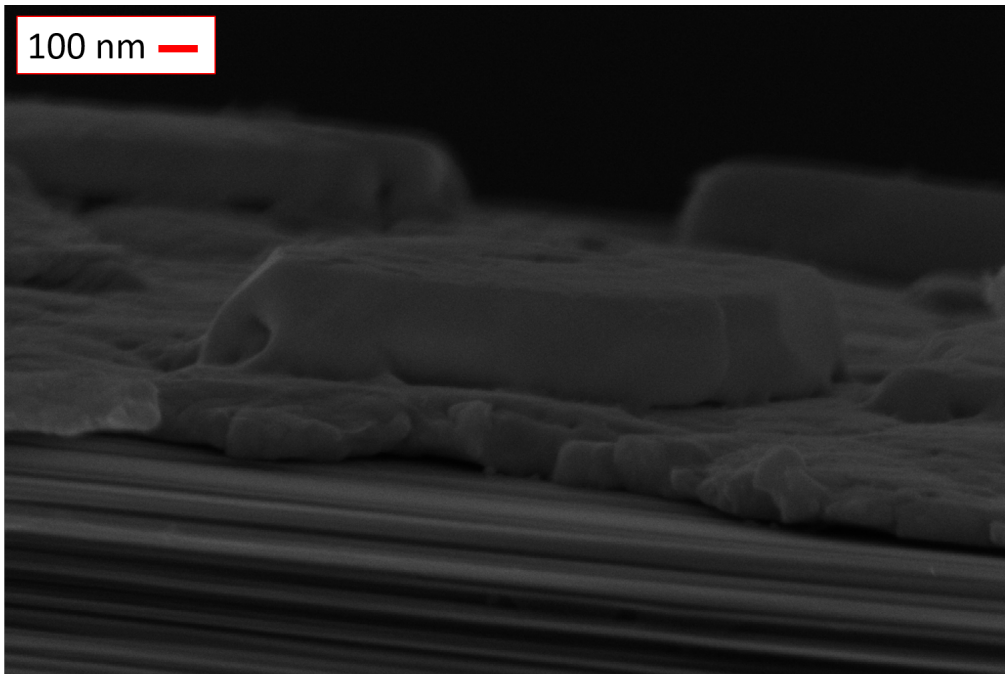

Figure 73: *Side view of a Sn sample, nominal thickness of* 400 *nm, deposited at* 140 *C on a* 10 *µm graphite substrate.*

The deposition seems divided into two phases: a compact and thin background layer, which covers uniformly the substrate, and some high and flat structures which protrude from it. This large tridimensional grains can reach several μm in size and about 300 nm in height, as can be appreciated in figures 72 and 73. The background layer appears very flat and compact, but it is just 100 nm thick; the sticking out grains are also very uniform, having a flat top and a constant height of 300 nm. However, even if the substrate is well covered and two distinct phases exist, this condition is extremely unfavorable if used in NUMEN data taking. The existence of two distinct thicknesses would give two values of the average energy loss, each of which would suffer straggling and dispersion. The combination of the two peaks would result in an excessive error in the data analysis.
A further decrease in the deposition temperature caused the growth of irregular structures on top of the plateaus observed in the previous sample. Moreover, very small crystals speckle the whole surface (figure 74). The increased irregularity can be noticed in the side image reported in figure 75: the plateaus are about 300 nm higher than the background, but the irregular structures are up to 1 μm high.

6.1.3 *The* 10 *μm Graphite Substrate with Chromium Buffer*

The best result achieved with the 10 μm graphite, which can be identified in the sample deposited at 140 C (figure 72), is far from being an optimal result. Tin and graphite interact too weakly to obtain a uniform deposition, hence the solution can reside in using a buffer material. Buffer materials are used as an interface to favor the adhesion of a film with the substrate; such material, which can be chromium or bismuth, easily bind with mostly any other material. In this case, a chromium buffer of 10 nm was used to ease the tin deposition.
The first sample of the batch was deposited at a temperature of 140 C, which in the previous batch allowed to obtain flat structures, although with two distinct thicknesses. Images 76 and 77 show the influence of the buffer: in the film is possible to distinguish the droplet-like structures, which in some cases merge together. For some aspects this is similar to previous samples, but here the grains are much more closely packed. The graphite is exposed only in few spots and the average thickness of the film seems to match the nominal thickness of 400 nm.

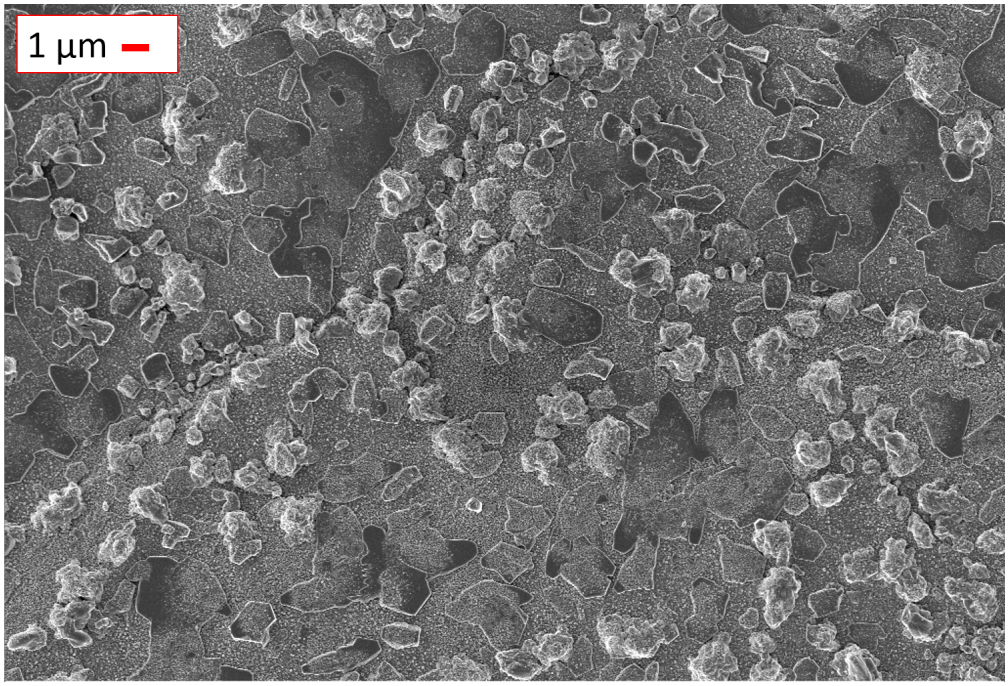

Figure 74: *Top view of a Sn sample, nominal thickness of* 400 *nm, deposited at* 130 *C on a* 10 *µm graphite substrate.*

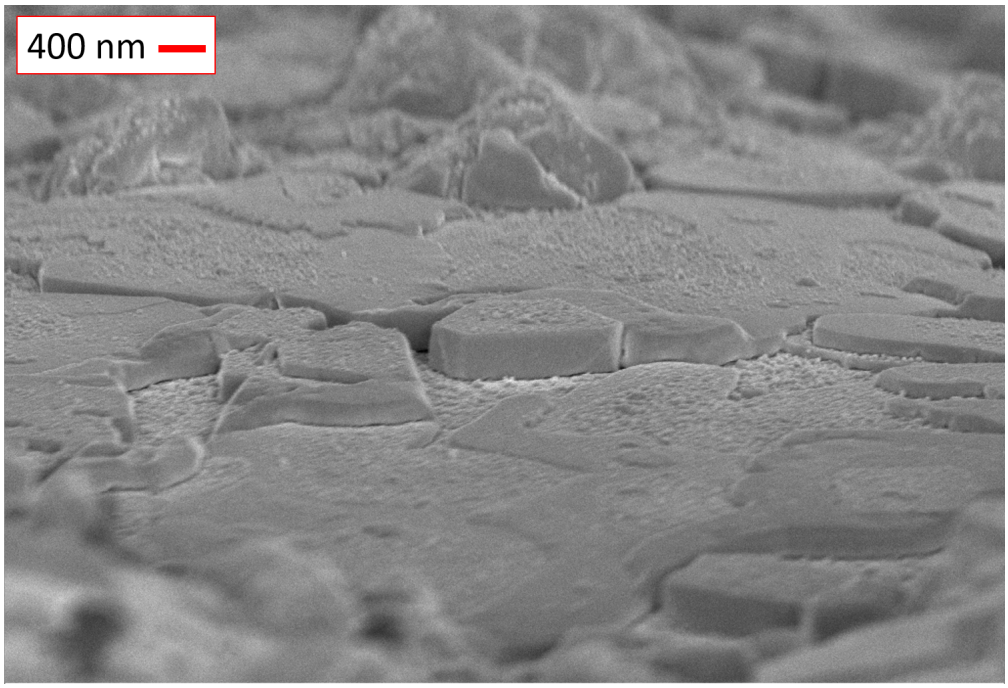

Figure 75: *Side view of a Sn sample, nominal thickness of* 400 *nm, deposited at* 130 *C on a* 10 *µm graphite substrate.*

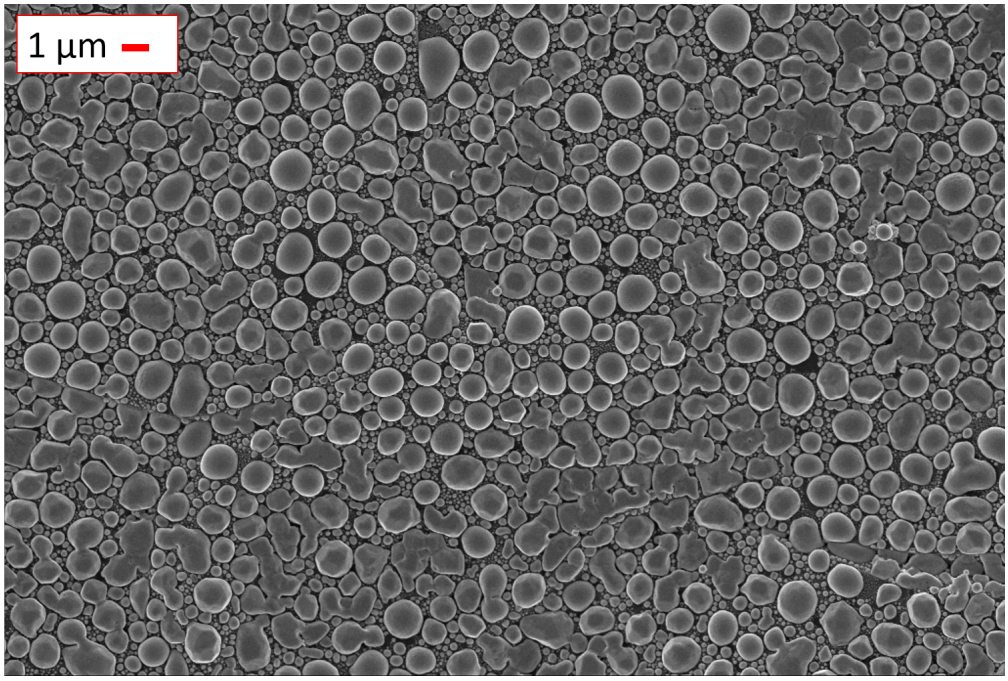

Figure 76: *Top view of a Sn sample, nominal thickness of* 400 *nm, deposited at* 140 *C. A* 10 *nm thick Cr buffer is previously deposited on the* 10 *µm graphite substrate.*

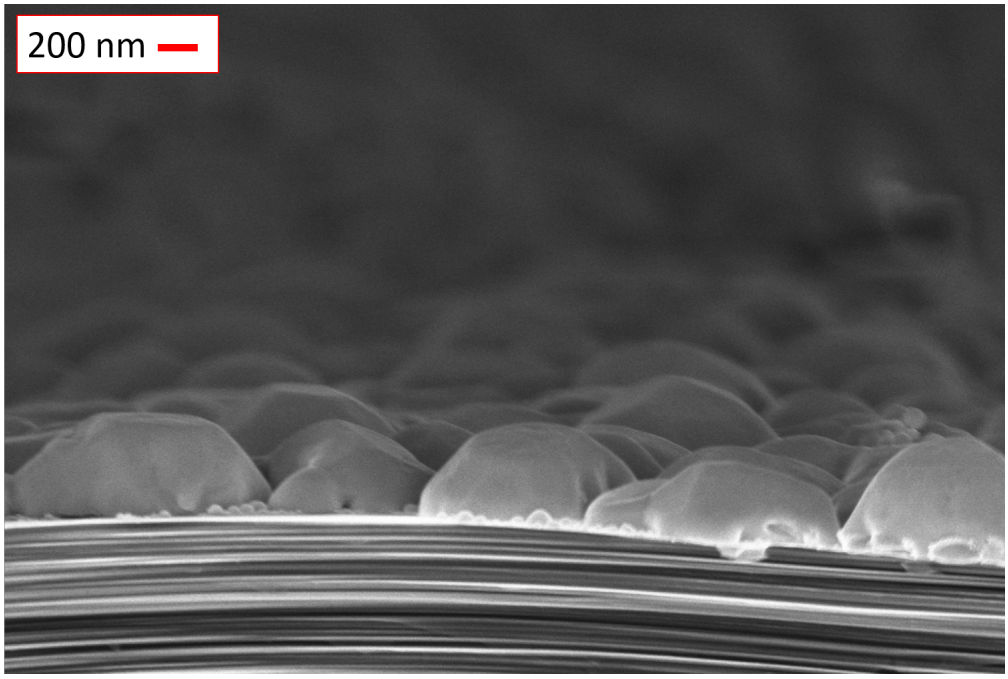

Figure 77: *Side view of a Sn sample, nominal thickness of* 400 *nm, deposited at* 140 *C. A* 10 *nm thick Cr buffer is previously deposited on the* 10 *µm graphite substrate.*

Considering the previous samples, the presence of droplets can be associated to an excessive deposition temperature; hence, the latter was diminished in the following trials. As expected, the sample deposited at 130 C, showed in figures 78 and 79, presents fewer droplets and more merged grains. For large patches of several μm, the graphite substrate is perfectly covered and no channels neither cracks can be observed. The film is not perfectly flat, as the droplets seem to protrude from the average thickness, but the degree of uniformity is satisfactory. Side images confirm it, showing a flat layer with some structure emerging from it. The flat and compact layer seems however thinner than the nominal value of 400 nm.
A last sample was deposited with these conditions, but at a lower temperature of 120 C (figures 80 and 81).
In this final sample the film appears compact and mostly smooth, but high irregular grains several μm big grew on the background layer. Side image reported in figure 81 resemble the previous sample morphology (figure 79), but shows a higher presence of superficial grains.

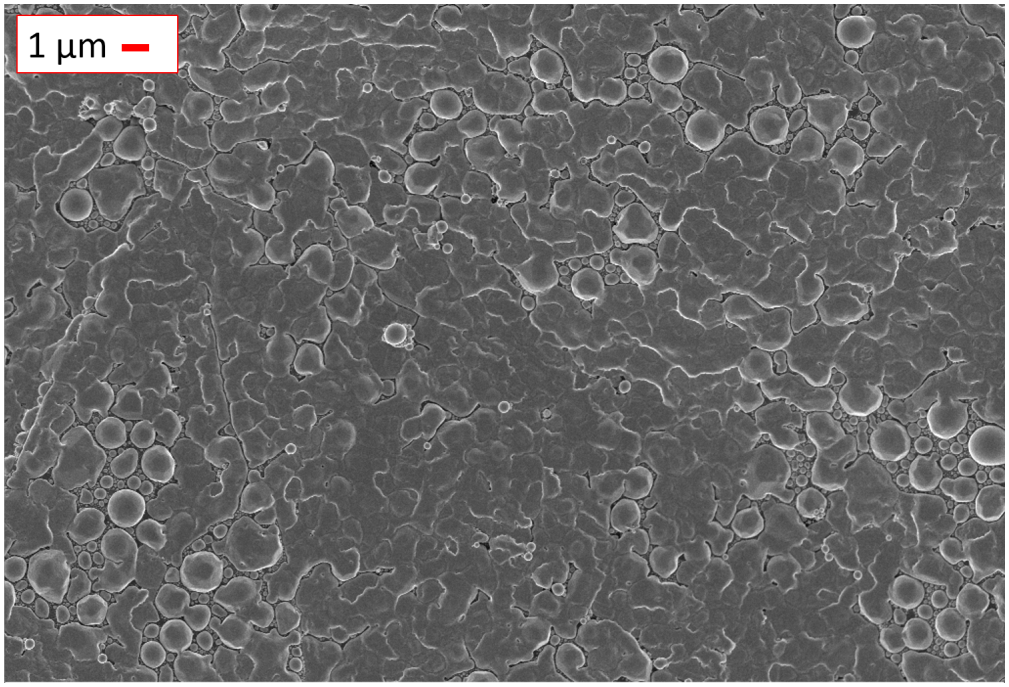

Figure 78: *Top view of a Sn sample, nominal thickness of* 400 *nm, deposited at* 130 *C. A* 10 *nm thick Cr buffer is previously deposited on the* 10 *µm graphite substrate.*

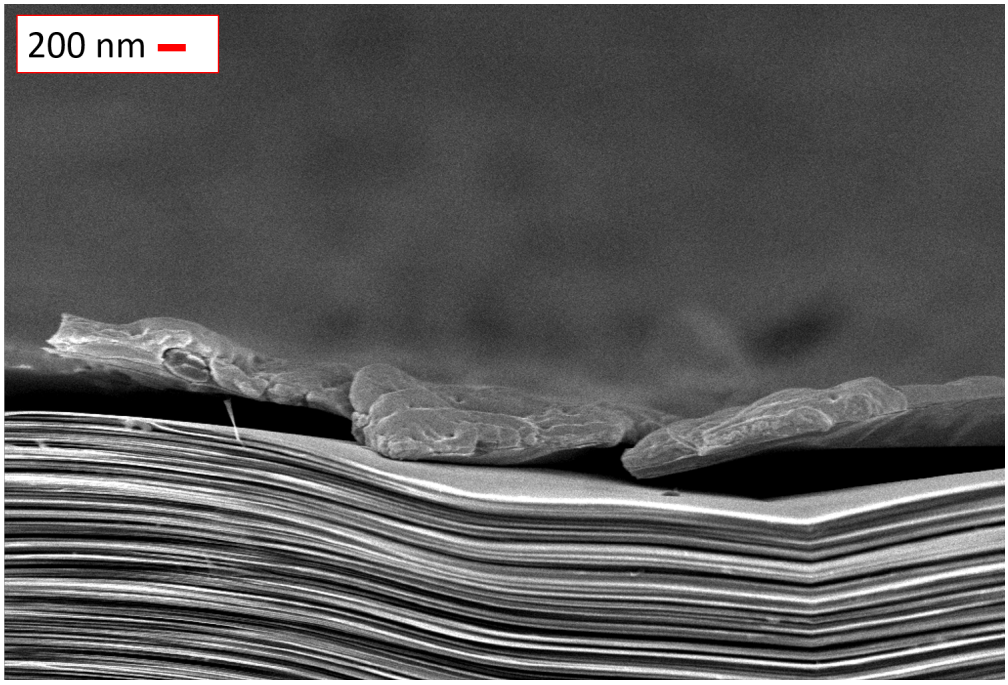

Figure 79: *Side view of a Sn sample, nominal thickness of* 400 *nm, deposited at* 130 *C. A* 10 *nm thick Cr buffer is previously deposited on the* 10 *µm graphite substrate.*

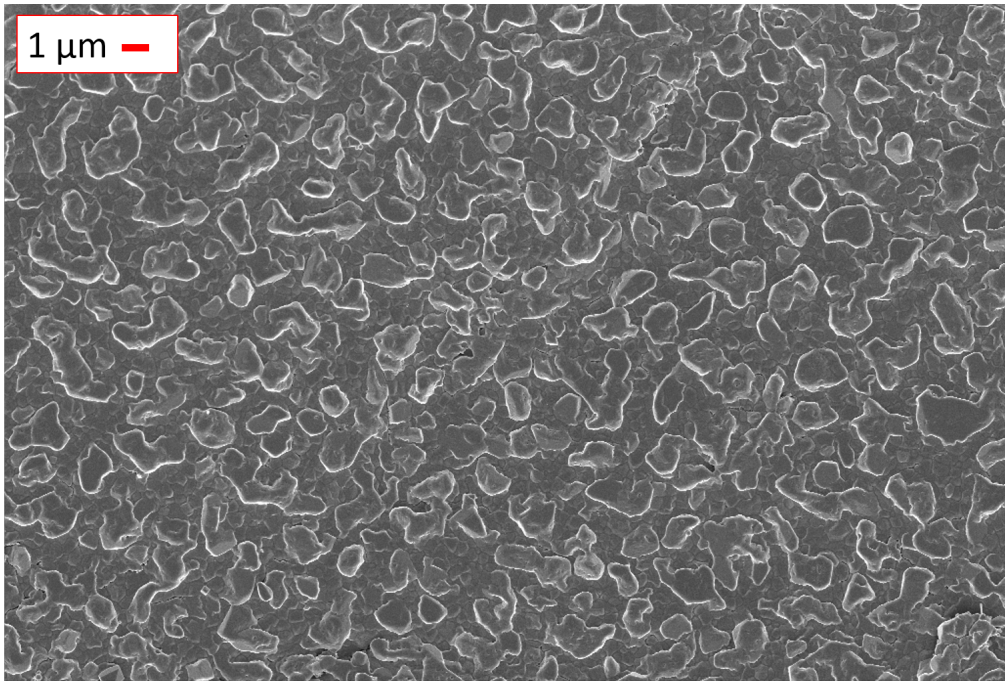

Figure 80: *Top view of a Sn sample, nominal thickness of* 400 *nm, deposited at* 120 *C. A* 10 *nm thick Cr buffer is previously deposited on the* 10 *µm graphite substrate.*

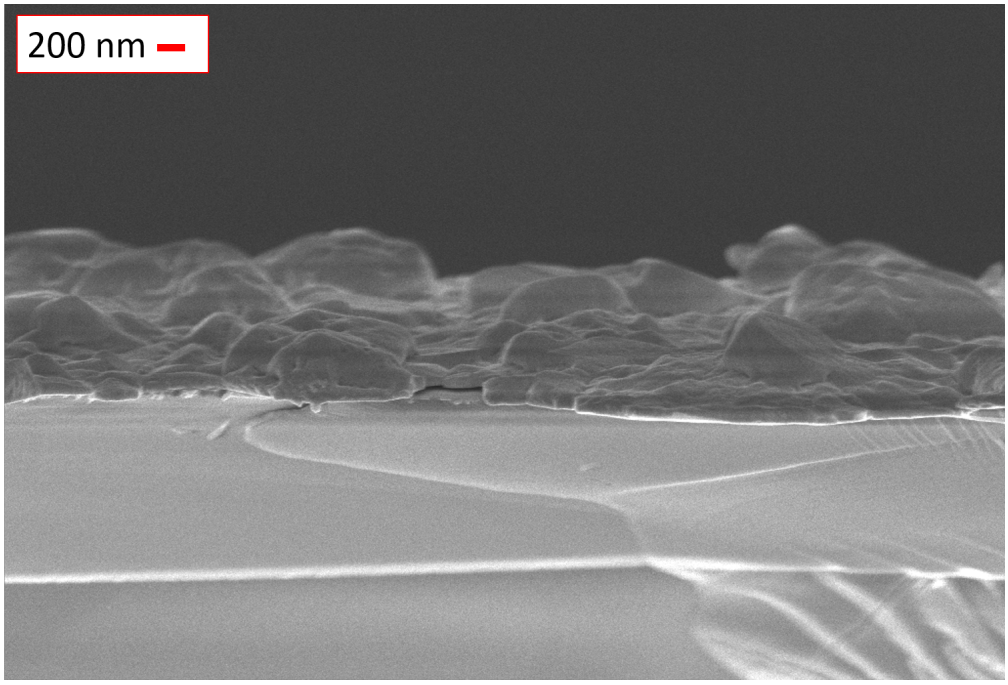

Figure 81: *Side view of a Sn sample, nominal thickness of* 400 *nm, deposited at* 120 *C. A* 10 *nm thick Cr buffer is previously deposited on the* 10 *µm graphite substrate.*

The growth mechanism observed in this latter sample (figures 80 and 81) can be seen in every sample which has been deposited at a too low temperature, as much as the droplets appear if the deposition temperature is instead too high. This extended study showed that for Sn the morphology is strongly dependent on the deposition temperature, the optimal one depends on the substrate. There exists a narrow temperature band that allows to obtain a flat and compact film; using a deposition temperature above such band would create a layer made of droplets, while depositing below such value would create a two phases film. When the bare 10 μm graphite was used as substrate, the film morphology changed from the spheres obtained at 150 C to the two-phases film obtained at 140 C; the temperature band at which a uniform film can be achieved lies somewhere in between those two values. Adding a Cr buffer slightly increase the width of such band, the transition between a droplet-made film and a two-phases one being smoother.

6.2 TELLURIUM TARGET DEPOSITION

Simultaneously to the study on the Sn targets, tellurium targets were also explored; the first batch was produced in the target laboratory of the INFN-LNS facility, using thin carbon films some hundreds nm thick as substrate. Tellurium film can grow either as a compact layer or as a needle tangle, depending again on the deposition conditions, method and substrate [60]. To explore the general behavior of a Te film deposited on carbon by EBD, in this batch a number of different conditions were tried. Films were deposited at room temperature and at 100 C, some of them undergoing a successive annealing.

6.2.1 *LNS Tellurium Samples*

The analysis of the sample deposited at room temperature, which nominal thickness is 350 nm, showed a rather flat layer (figures 82 and 83); no high structure can be observed, a part from superficial contamination. A magnified image, reported in figure 83, shows that the speckles that can be seen in figure 82 are small Te crystals. In this deposition conditions tellurium grows in small lamellas stacks about 100 nm in size, which however are mostly parallel to the plane. The film as a whole appears compact, uniformly covering the carbon substrate.
A sample deposited in the same conditions underwent an annealing treatment at 200 C for 1 hour (figures 84 and 85). Again the film appears flat, compact and uniform, with fewer crystal with respect to the previous one. A deeper insight, figure 85, shows that the stacks of lamellas disappeared; rounded small grains, few tens of nm in size, took their place, making the film appear smoother.
These first trials underline the big difference between Te and Sn films. At room temperature, the latter grows in big and complex crystal structures, with channel and pores; on the other hands, the former appears flat and uniform, with small crystal aligned to the plane. If the annealing procedure is mostly superfluous for Sn, in the Te film contributes to smooth the surface, reducing the crystal size and sharpness. Also increasing the deposition temperature gives different results in the two cases: for Sn it can facilitate the formation of a more uniform film, while for Te it strongly promotes the growth of large crystals.

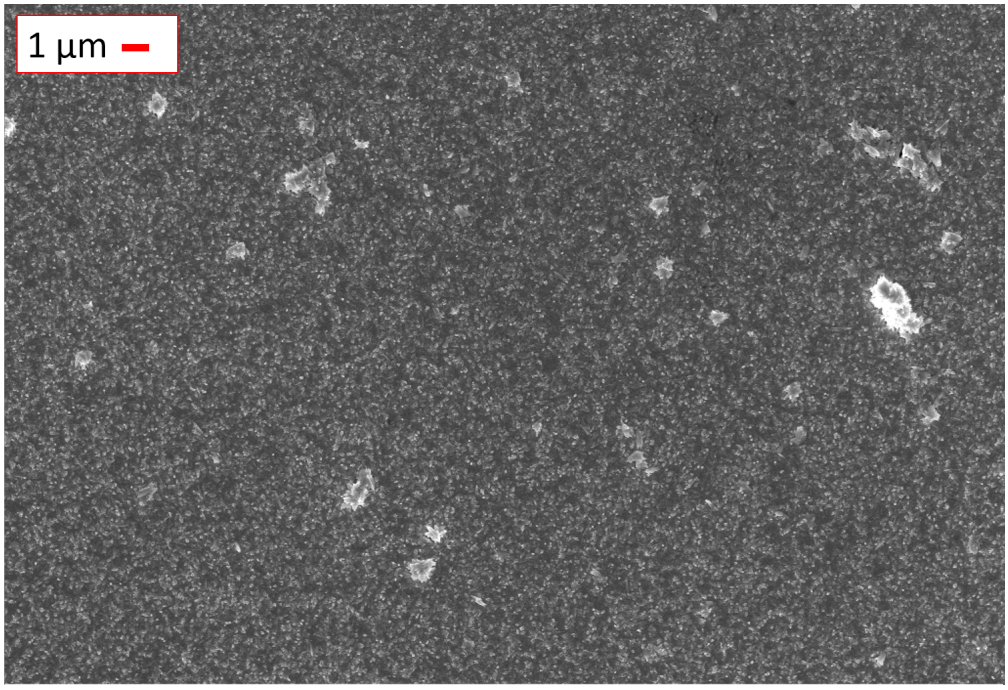

Figure 82: *Top view of Te sample, deposited on a C substrate at room temperature. The nominal thickness is 350 nm.*

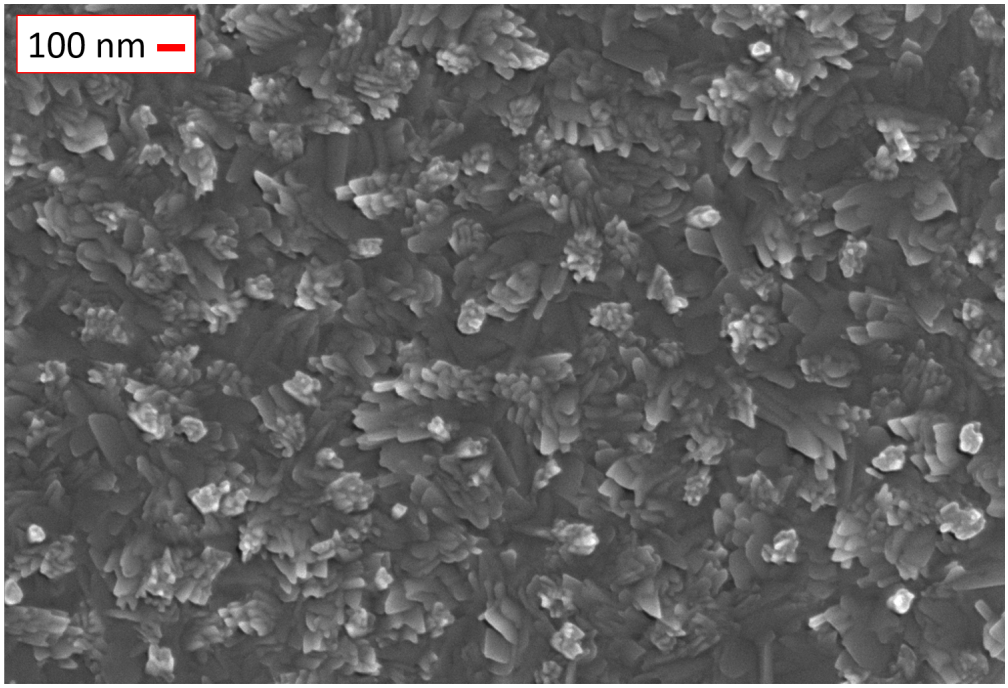

Figure 83: *Detail of the sample showed in figure 82.*

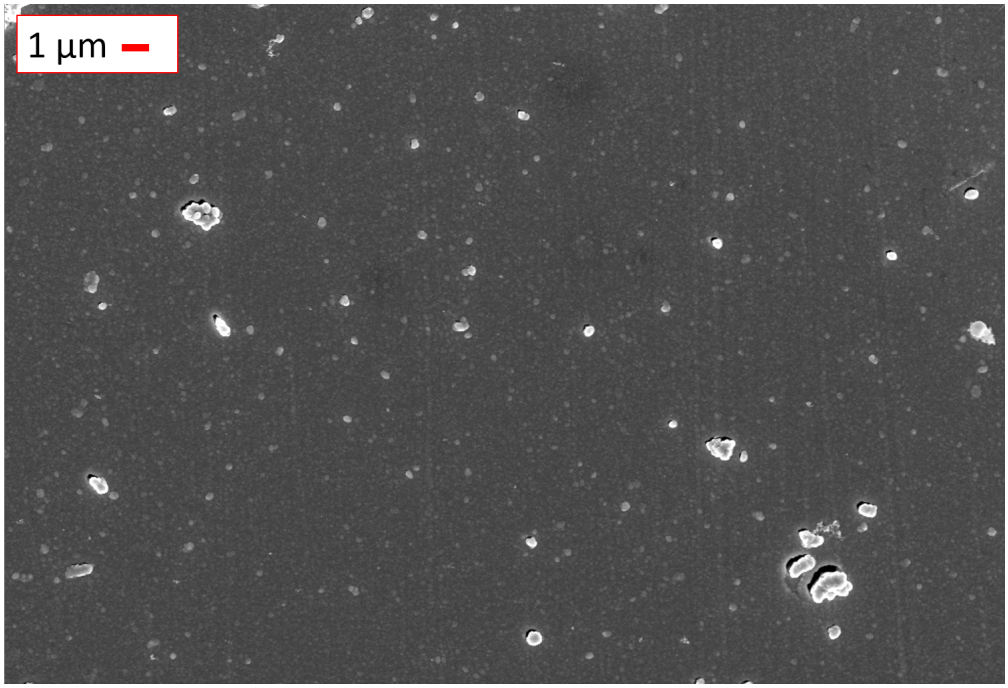

Figure 84: *Top view of Te sample, deposited on a C substrate at room temperature and annealed at* 200 *C for* 1 *hour. The nominal thickness is* 300 *nm.*

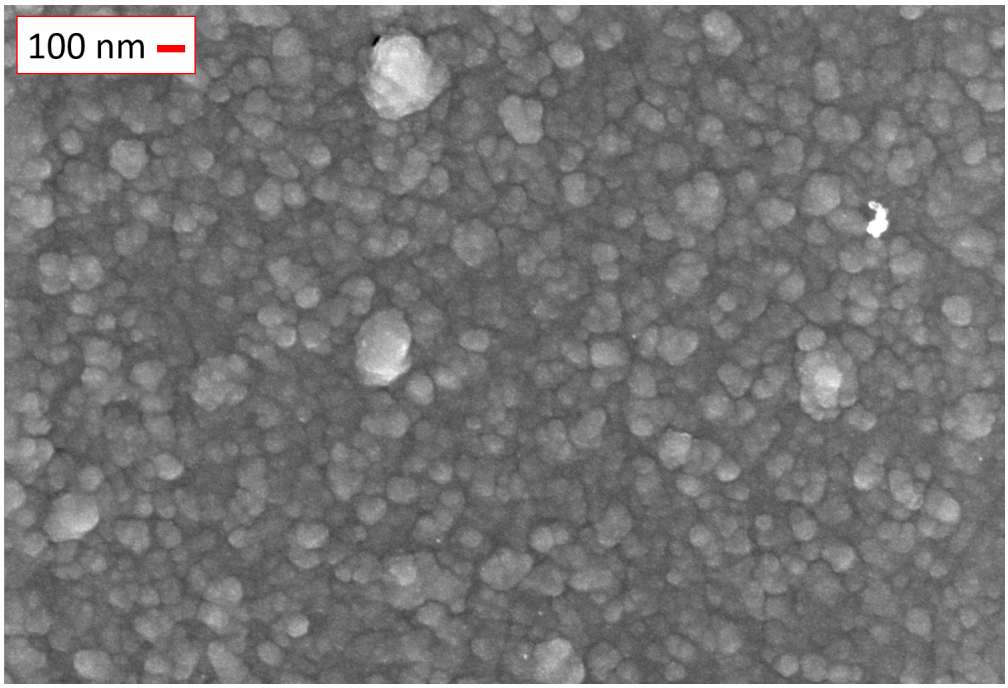

Figure 85: *Detail of the sample showed in figure 84.*

Setting the deposition temperature at 100 C favors excessively the formation of crystals, producing a structure resembling a needle tangle (figures 86 and 87). Te crystals appear thin but several μm long, forming a complex network and a highly structured film. The detailed view of the film structure better shows the crystal dimension, but also reveals the disorder of the film. Without a measurement dedicated to establish the thickness, it is difficult to even estimate the real thickness of the sample; such value is probably more than the nominal value, due to the low density caused by the big, nested crystals.
A similar sample, deposited at 100 C, was successively annealed at 200 C. The effects of the post-deposition treatment on the film appearance was noticeable (figures 88 and 89). Te crystals decreased their size, forming a much denser layer with reduced interstitial space. The average size of the crystals decreased to less than 1 μm, as can be clearly seen in figure 89. Even though this film appears denser than the non-annealed one, the uniformity in thickness is not optimal.

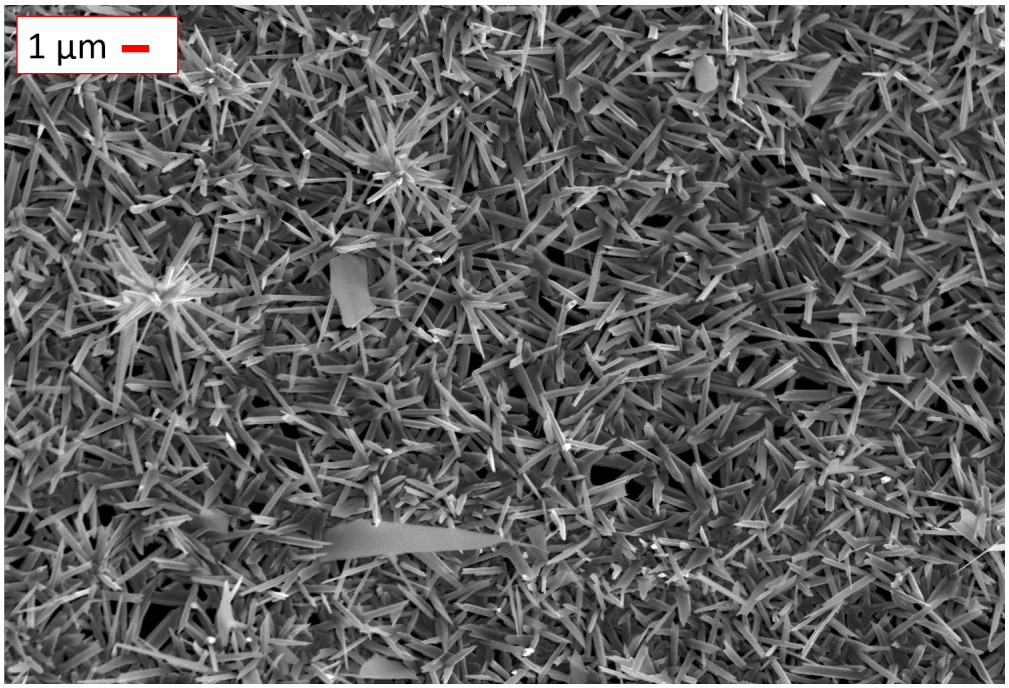

Figure 86: *Top view of Te sample, deposited on a C substrate at* 100 *C. The nominal thickness is* 350 *nm.*

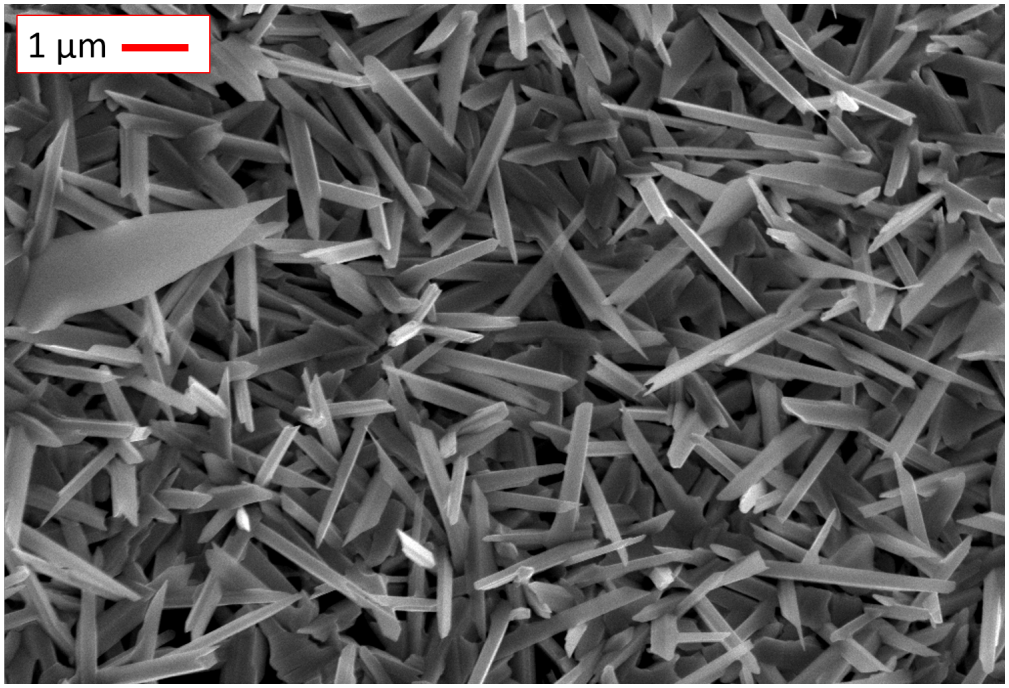

Figure 87: *Detail of the sample showed in figure 86.*

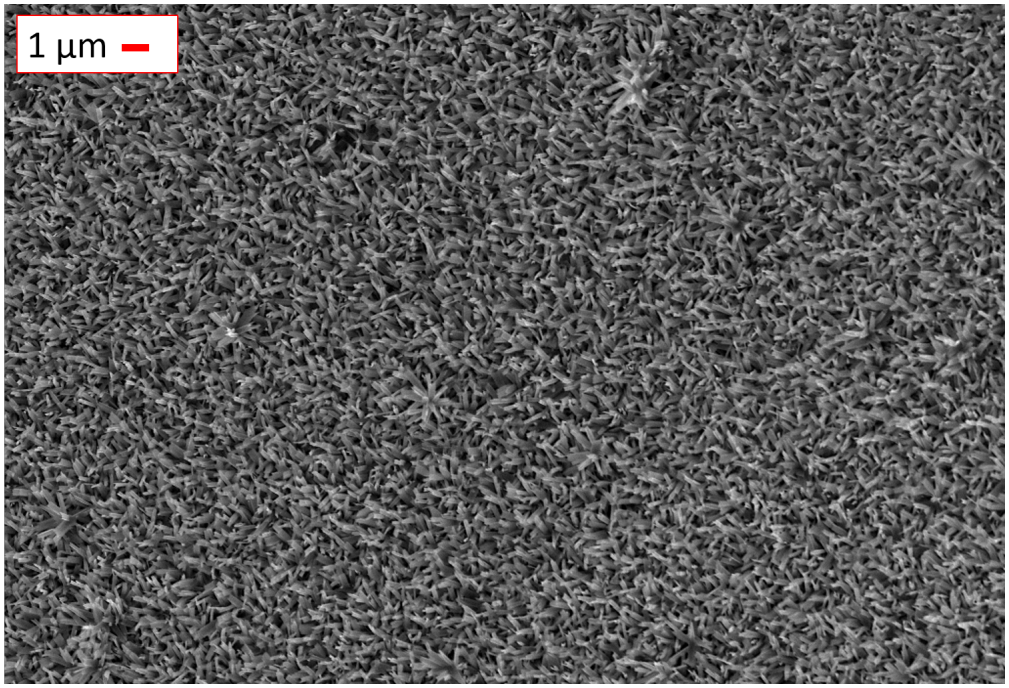

Figure 88: *Top view of Te sample, deposited on a C substrate at* 100 *C and annealed at* 200 *C. The nominal thickness is* 350 *nm.*

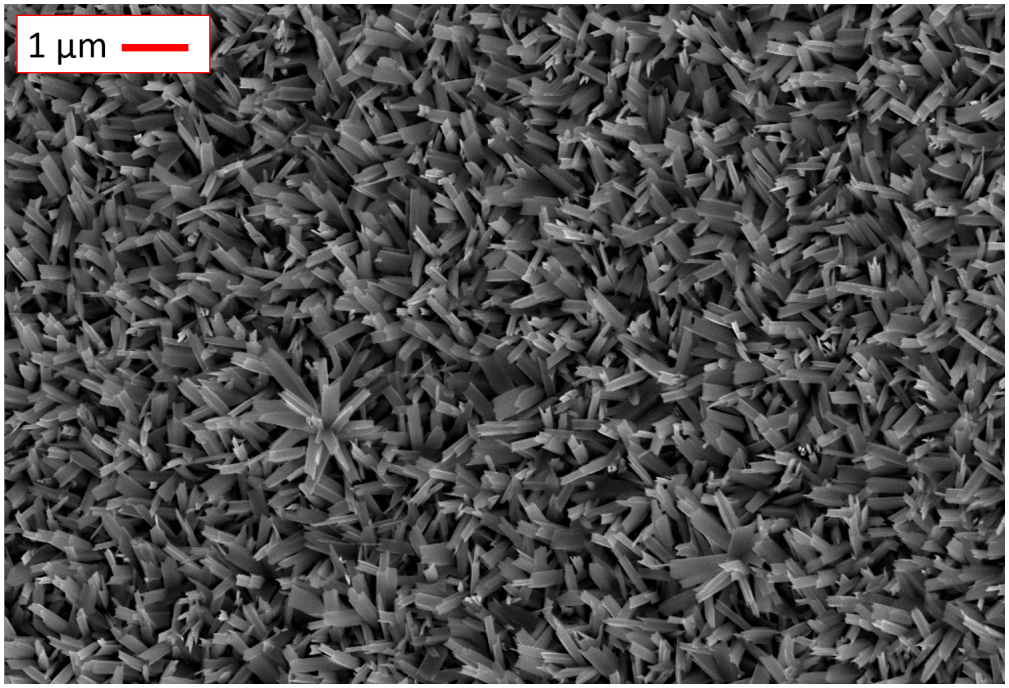

Figure 89: *Detail of the sample showed in figure 88.*

6.2.2 *The Te deposition on the* 10 *µm Graphite Substrate*

Considering the first batch of samples deposited on a carbon substrate, it seems that room temperature deposition, with or without annealing, provides a film of very good quality. Conversely, depositing at the moderate temperature of 100 C excessively promotes the crystal growth. Given the nature of the used substrate, it would be appropriate to explore the effects of these conditions on a 10 μm thick HOPG substrate. In this case, also side images could be provided.
The first sample was deposited on HOPG at room temperature, with a nominal thickness of 400 nm (figures 90 and 91). SEM images of the film reveal a uniform coverage of the substrate and a pretty smooth deposition, with some structures above the surface. Such structures are Te crystals grown above the average thickness. Their structure recalls the one of the film, which seems composed by randomly oriented bundles of needles/lamellas. The crystals seem to grow vertically, feature that can be better observed in the side image reported in figure 91.

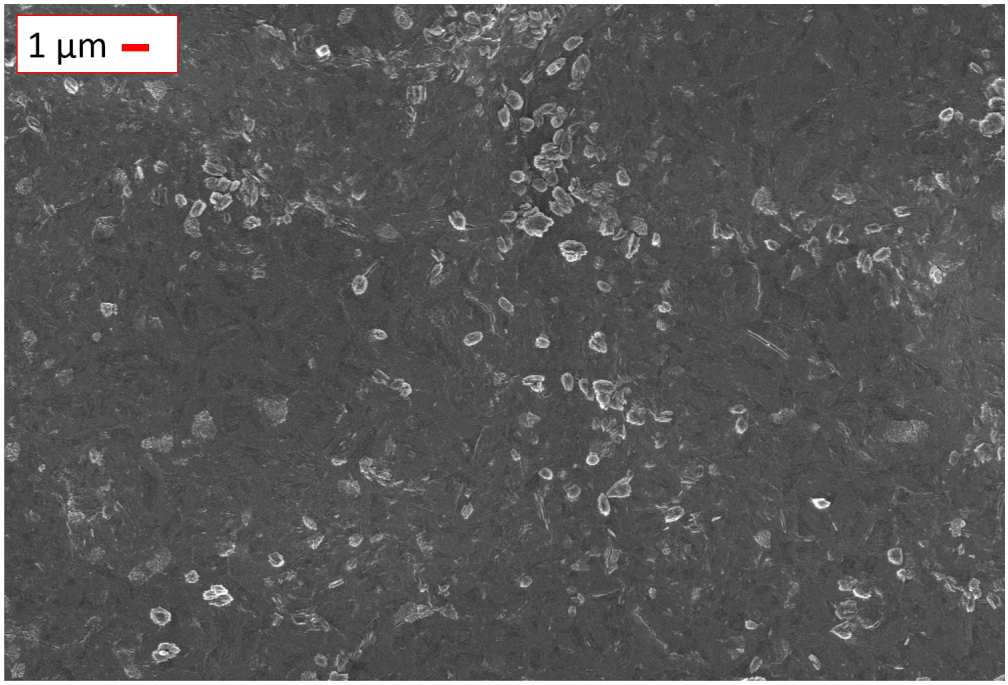

Figure 90: *Top view of a Te sample, nominal thickness of* 400 *nm, deposited at room temperature on a* 10 *µm thick HOPG substrate.*

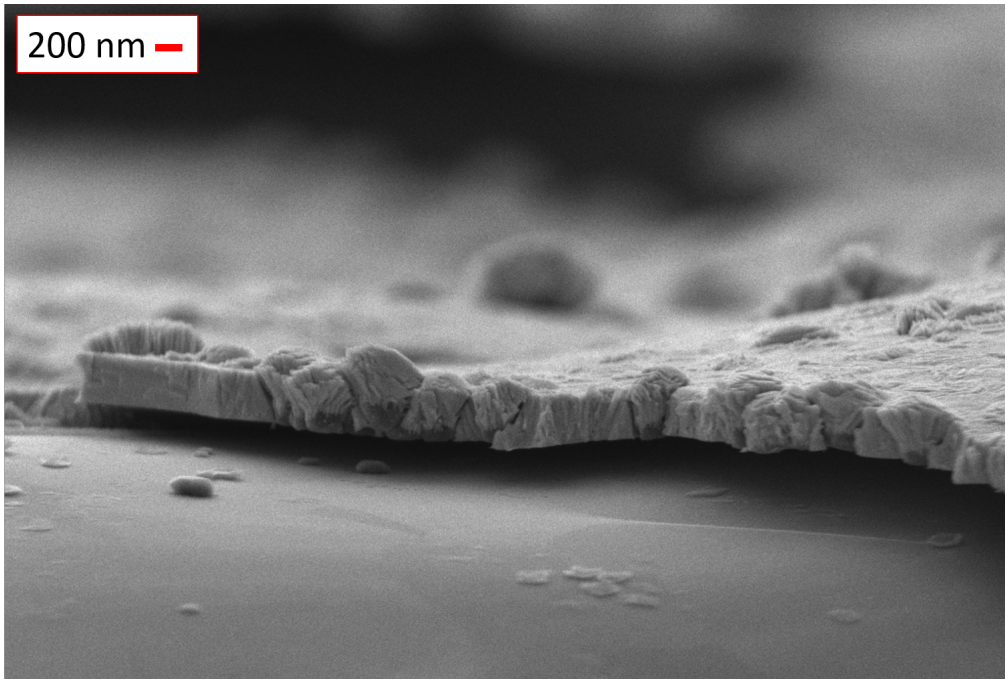

Figure 91: *Side view of a Te sample, nominal thickness of* 400 *nm, deposited at room temperature on a* 10 *µm thick HOPG substrate.*

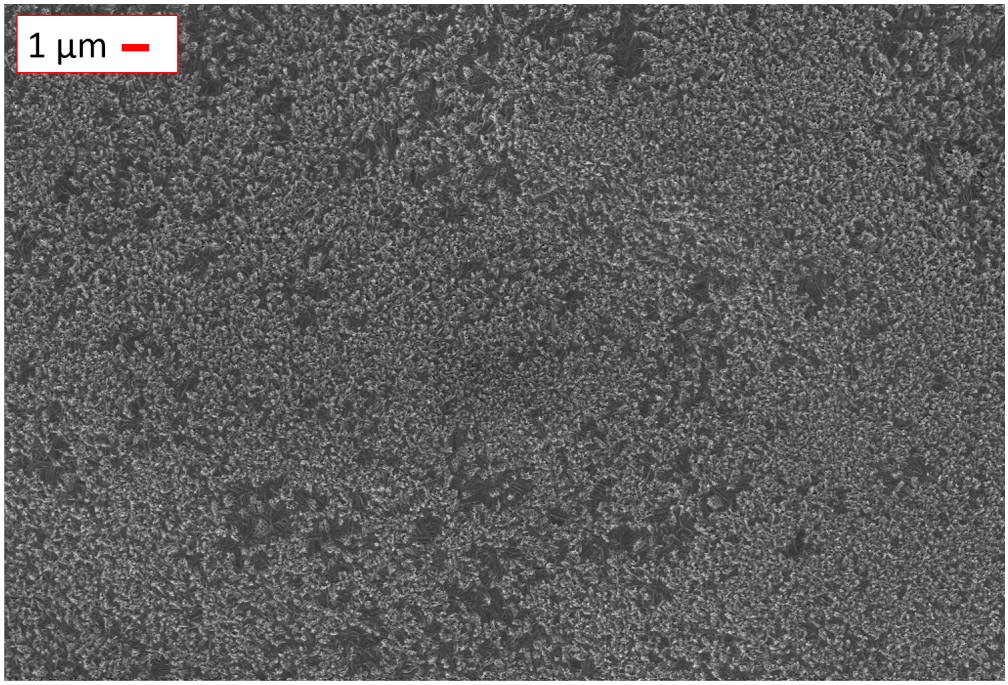

Figure 92: *Top view of a Te sample, nominal thickness of* 400 *nm, deposited at* 100 *C on a* 10 *µm thick HOPG substrate.*

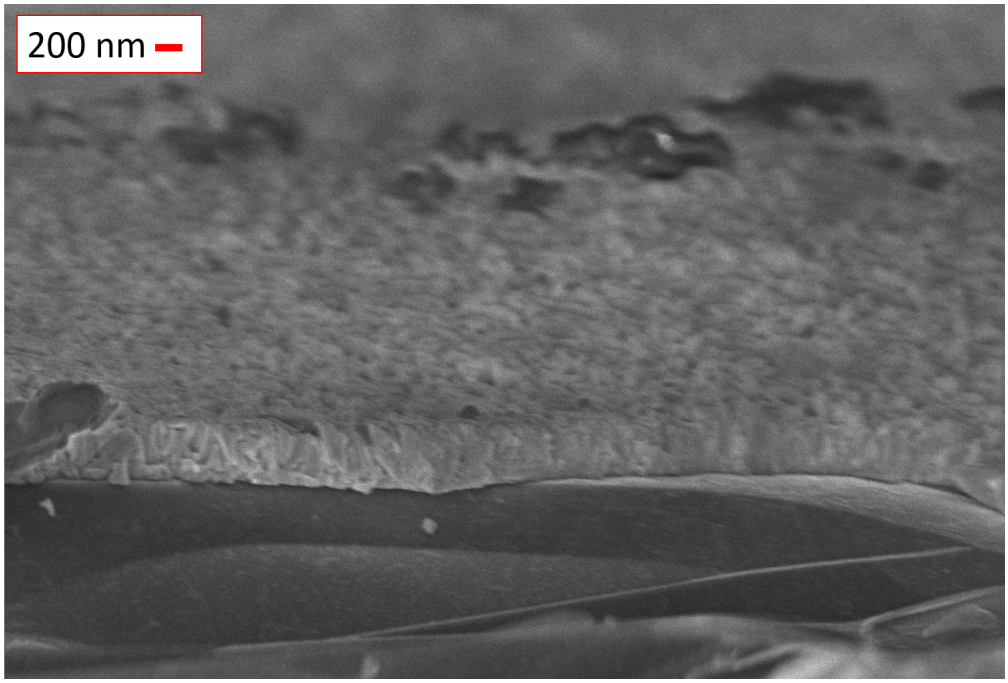

Figure 93: *Side view of a Te sample, nominal thickness of* 400 *nm, deposited at* 100 *C on a* 10 *µm thick HOPG substrate.*

A substantial difference with the previous batch was found in the production of samples at 100 C (figures 92 and 93). The network of needles which grew on the carbon substrate did not form with the new substrate; very small, nm sized crystals grew on top of a compact and flat background layer, with no high features or structures. Similarly to the room temperature grown film, side images show a compact film with vertically aligned crystals. The thickness seems close to the nominal value of 400 nm.
In the production of tellurium films on HOPG substrates, good results were achieved both depositing the material at room temperature and at 100 C. In both cases the film appears compact and flat, with very few structures above the surface; the surface of the latter sample seems rougher than the room temperature one, but such roughness is only few nm in size.

6.2.3 *The* 10 *μm Graphite Substrate with Chromium Buffer*

Even if good results were obtained with a simple HOPG substrate, some trials were made using a Cr buffer. As before, two kind of samples were produced: one deposited at room temperature and the other at 100 C. The nominal thickness, for all of them, was again 400 nm for the Te film and 10 nm for the Cr buffer.
Top images of the first sample of this series, deposited at room temperature, showed a film similar to the one deposited in the same conditions but without buffer. Both this sample (figure 94) and the no-buffered version (figure 90) uniformly cover the substrate, presenting the same bundle-appearance. Some crystals few hundreds of nm big can be spotted on the surface of the samples. One difference can be noticed in the side images: the Cr buffer seems to enhance the alignment of the crystals, which in figure 95 appear mostly vertical.
The situation differs in the sample deposited at 100 C: the film, albeit appearing planar and compact, presents a sort of polygonal design, with the boundary of such polygons covered in sharp crystals. This curious arrangement can be clearly observed in top view (figure 96), but can be hardly spotted in side imaging (figure 97). Side images, however, reveal that this sample as well presents a lamellar/needle like structure, with crystal well aligned along the vertical direction. The dis-homogeneity of the film seems to be within few tens of nm, which is well below the experimental limits for the dispersion error.

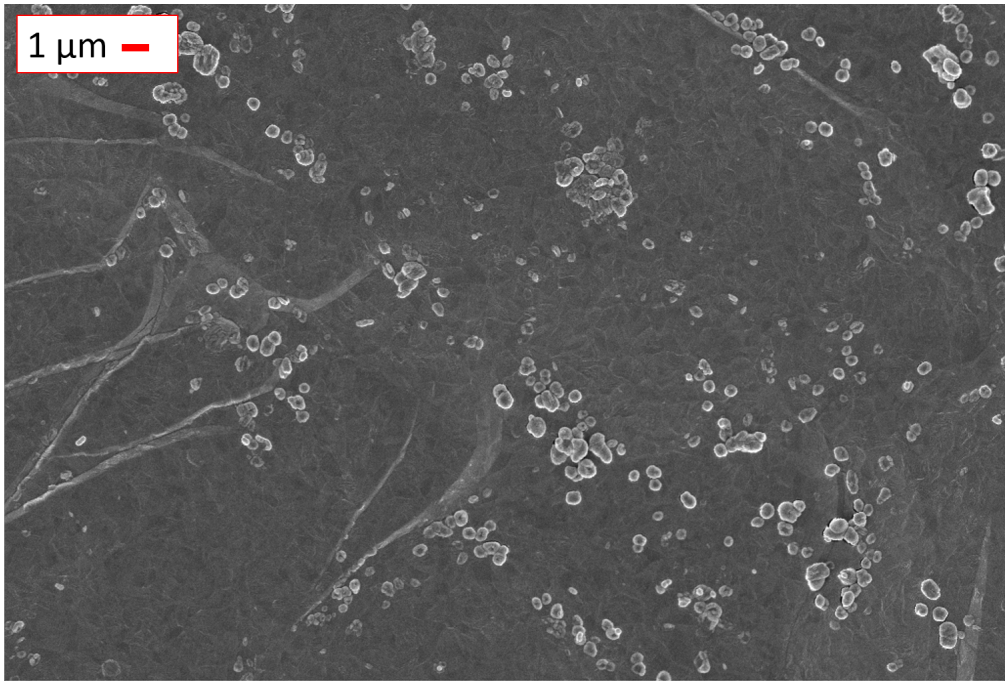

Figure 94: *Top view of a Te sample, nominal thickness of* 400 *nm, deposited at room temperature on a* 10 *µm thick HOPG substrate, using a* 10 *nm thick chromium buffer.*

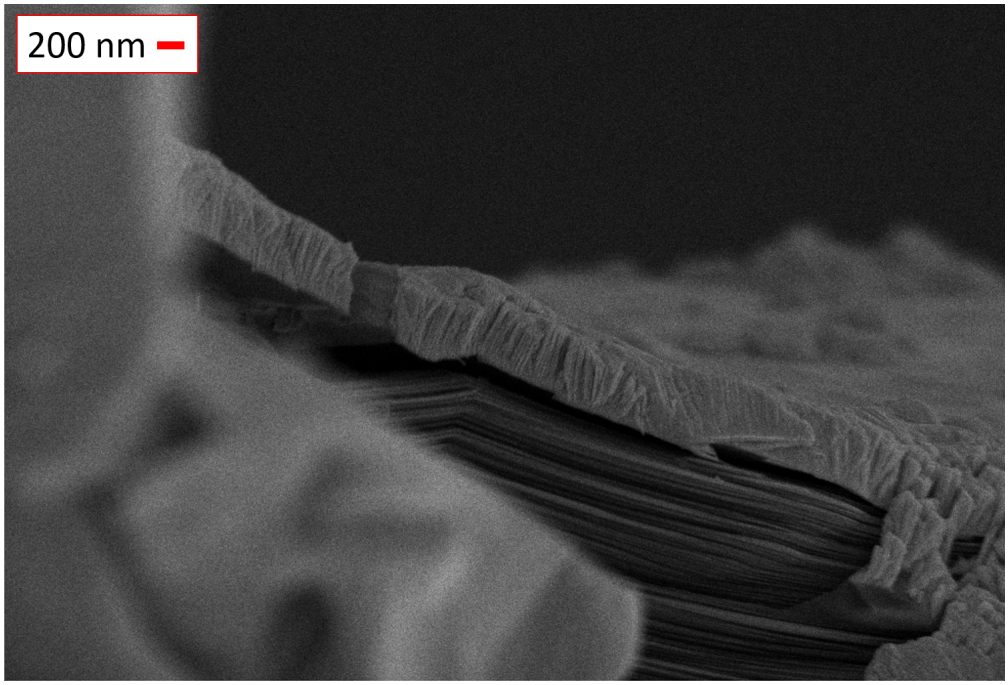

Figure 95: *Side view of a Te sample, nominal thickness of* 400 *nm, deposited at room temperature on a* 10 *µm thick HOPG substrate.*

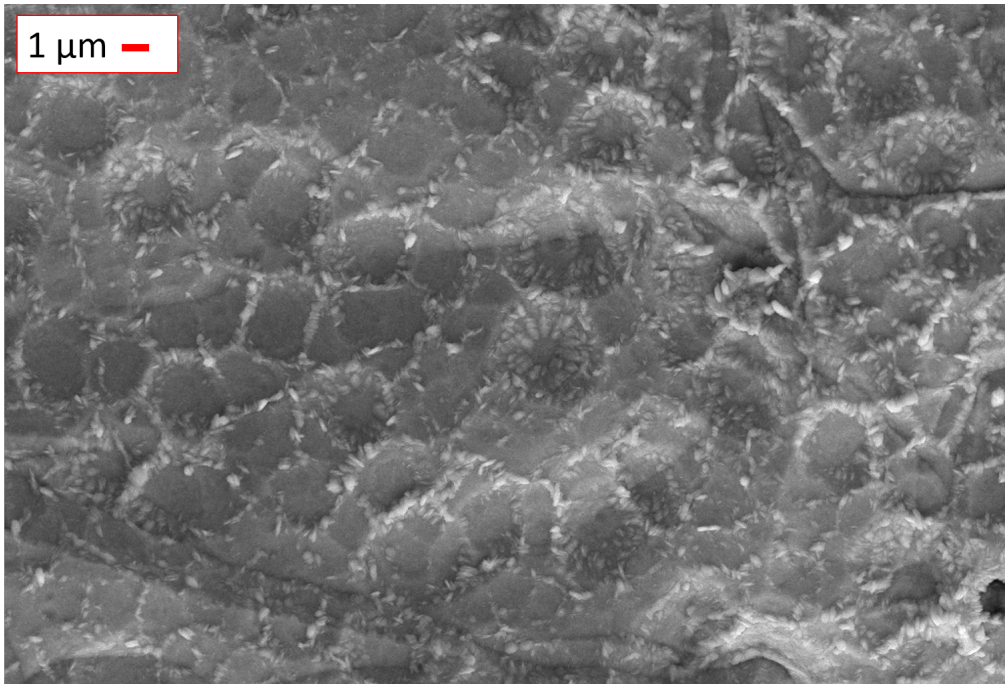

Figure 96: *Top view of a Te sample, nominal thickness of* 400 *nm, deposited at* 100 *C on a* 10 *µm thick HOPG substrate.*

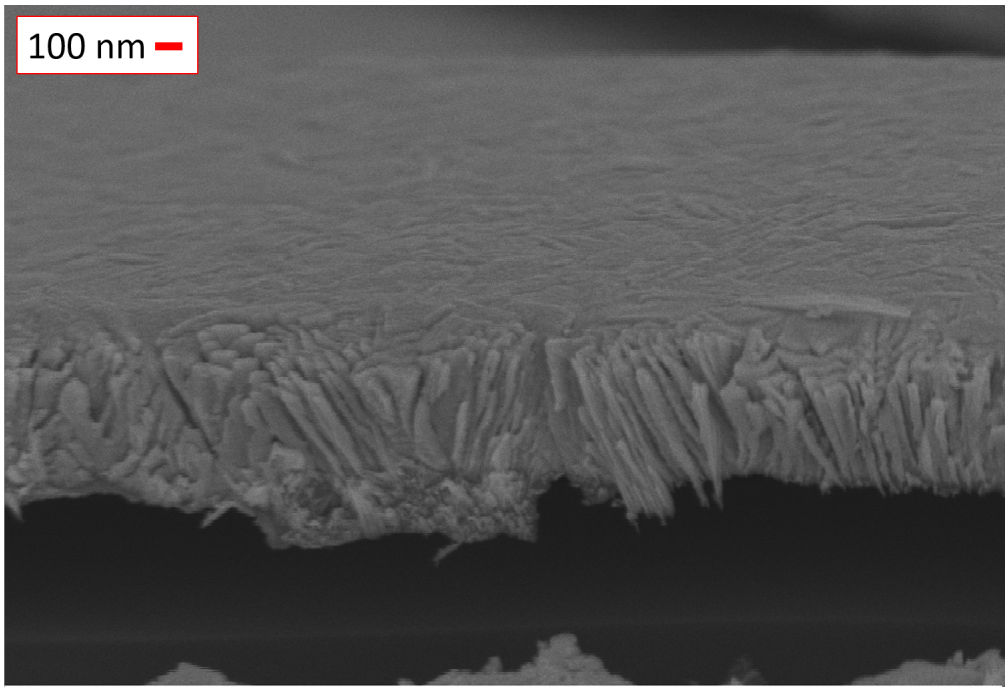

Figure 97: *Side view of a Te sample, nominal thickness of* 400 *nm, deposited at* 100 *C on a* 10 *µm thick HOPG substrate.*

7

EXPERIMENTAL TESTS

After the positive outcome of theoretical calculations, two tests were arranged to obtain some information about the actual behavior of the cooling system. The setup used in the first test was rather simple, consisting mainly of an IR-LASER as heat source and a thermal camera to measure the temperature; the test was designed to provide just a rough estimate of the target/graphite system thermal behavior. The second test had a higher degree of complexity, since it involved the usage of a cooling system, several detectors and an ion beam. The purpose of this latter test was to evaluate the impact of adding a sample holder/heat sink in the dissipation chain.

7.1 LASER TEST

As aforementioned, the first test was mostly aimed to estimate the dissipating capabilities of the target-graphite system alone, without any copper sample holder. To this end, the first Sn target produced on the 10 μm thick HOPG was irradiated with an infrared LASER having a wavelength of 808 nm and 20 W of maximum output power. The conditions in which this test had been run may seem distant from the actual experimental conditions. While this is partially true, the information which can be gathered could be quite useful. There exist moreover, some limits related to the complexity of running a test with a full operating cooling system in an ion beam facility. For example, the difficulty of finding a suitable facility, with an ion beam of sufficient intensity and a scattering chamber big and versatile enough to host the LN_2 based sample holder and cooling circuit. It is clear that the implementation of such an experimental setup would be much richer in gained information, but would also require a much longer time for preparation.
With a much simpler apparatus, it would be possible to probe a fundamental parameter: the adhesion and the heat transfer between the target and the substrate, which in the calculation is supposed perfect. A LASER is in this case even better than an ion beam, since it would be fully absorbed in the most superficial part of the Sn layer. Also, it does not require a vacuum system and chamber to operate: an optical table with a suitable alignment system in a at-

mosphere controlled lab would suffice. As already said, the used Sn target is the one deposited at 175 C on HOPG, whose SEM image is reported in figure 69. This sample, the first deposited on 10 μm thick HOPG, pointed out the difference in surface properties with respect to the thicker substrate and the necessity to find again the best deposition parameters. The Sn droplets form a discontinuous film partially exposing the underlying graphite substrate. Despite this fact, the droplets cover the major part of the substrate. The discontinuity along the plane is not a major issue, since the heat conduction along the target plane is not that important to the dissipating mechanism. The great part of the heat is, in fact, supposed to quickly pass in the graphite.

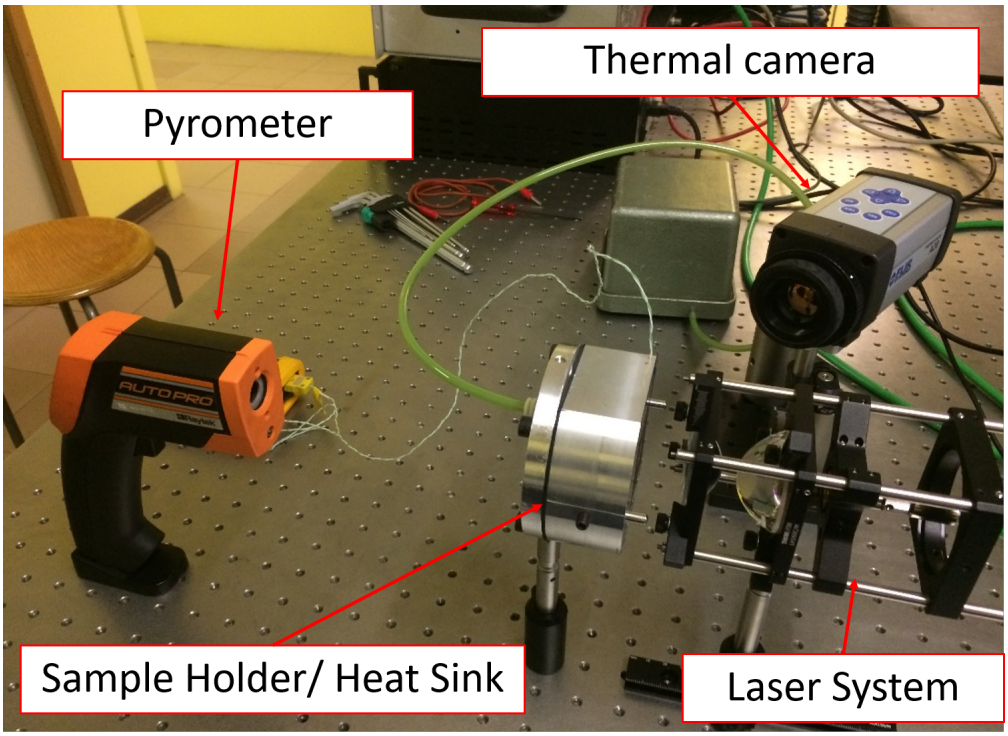

Figure 98: *Setup of the LASER test, showing the position of various instruments. The target, not visible, faces the LASER system; the aluminum sample holder has a channel* 1 *cm large in the center, to allow measurements in the back part of the graphite.*

The experimental setup is shown in figure 98. The aluminum sample holder is hollow inside, with a flat face pierced by numerous small holes. Connecting a vacuum pump to it, it is possible to fix the graphite substrate to it by suction. In figure 99 is shown the target and the holes can be seen as well. Tape has

been used to further fix the sample and to seal the remaining holes.
The IR LASER is brought close to the target by a focusing system, which prevents the spreading of the beam spot. A thermal camera had been placed diagonally with respect to the LASER direction; the camera allowed to collect thermal maps of the tin target, recording images and videos of the sample thermal profile. Behind the target, a 1 cm large channel in the aluminum sample holder allows to use a pyrometer to keep track of the temperature also on the back of the sample. Finally, a thermocouple was placed on the aluminum sample holder in order to monitor its temperature, which will influence the final temperature of the target.

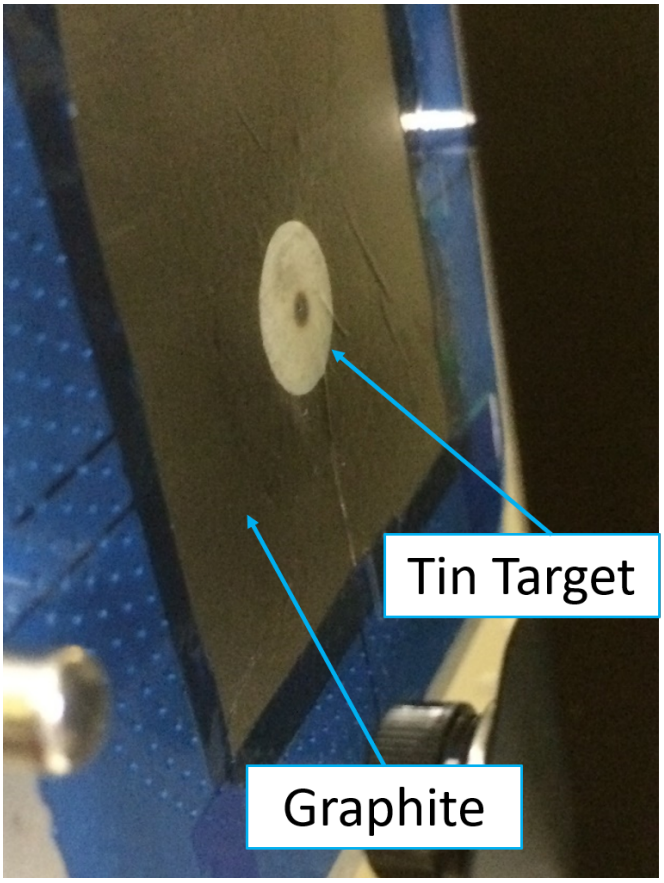

Figure 99: *Sn sample used in the test. The holes used for keeping the sample in position can be spot below the tape. The picture was taken after the irradiation.*

The maximum output power of the LASER is 20 W, which is about the power a 35 μA ion beam would deposit. However, the test had been performed without a cooling system, hence such power would had been excessive. The

Figure 100: *Frame of a video of the heating test performed with an output power of* 12 *W. The frame is taken after* 1 *second of irradiation.*

irradiation was performed by steps to keep the target in a safe range; the maximum reached power was of 12 W, which correspond to a 21 μA ion beam current. Such value does not correspond to the actual absorbed power, which depends on a number of factors. In fact, a drawback of using a LASER instead of an ion beam is the presence of light related issues, like reflection, which has a non negligible influence on the effective absorbed power. For bulk tin, reflection is evaluated in about 80% of the incoming radiation [61], so that only about 3 W of the total output of 12 W would be absorbed. Evaluating the precise amount of absorbed energy for the sample used in the test is not an easy task, due to the film structure and the partial exposure of the substrate; since the final temperature depends mainly on the absorbed power, its effective value could be estimated fitting the data with numerical evaluations.
The sample was irradiated at several values of the output power: 3 W, 6 W,

9 W and 12 W; each irradiation step lasted for several minutes, although the stationary state is reached in less than a second.

The temperature was measured both on the target, with the thermal camera, and on the graphite, using the pyrometer. A typical temperature map obtained with the thermal camera is reported in figure 100, which shows a target irradiated with a LASER power of 12 W. The measurement was performed to verify the thermal uniformity along the direction perpendicular to the plane, along which the graphite possesses a poor thermal conductivity. The agreement between the two instruments was very good, as shown in figure 101.

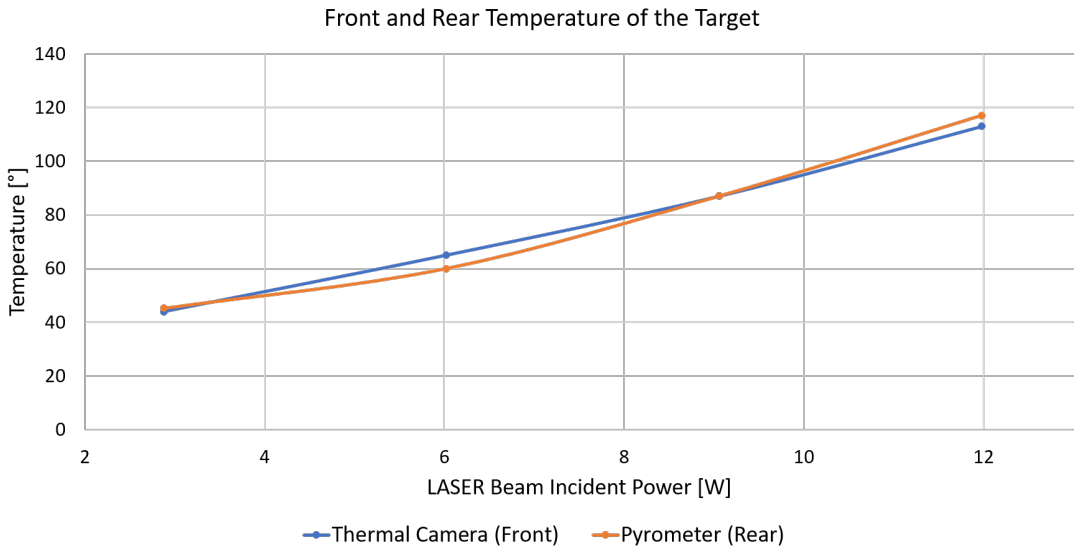

Figure 101: *Comparison between the temperature measured on the target (thermal camera) and on the rear side of the graphite (pyrometer).*

The rise in temperature is linearly proportional to the absorbed power: the steeper the slope, the higher the absorbed power. However, as mentioned above, for this particular target the precise evaluation of the reflected and absorbed power is not trivial. The experimental data were hence fitted with theoretical data, evaluated with the numerical code of section 4.1. The best fit with the collected data at 3 W, 6 W, 9 W and 12 W was found for ion beam currents of 2.5 μA, 5 μA, 7.5 μA and 10 μA, respectively. The comparison is reported in figure 102. The temperature increase provoked by the power deposited by such beams is close the the measured ones, within a 10% error; this is a reasonable value, considering the thermal camera error, the partial coverage, the air, ect. Thus, the effective absorbed power is estimated to be roughly 50% of

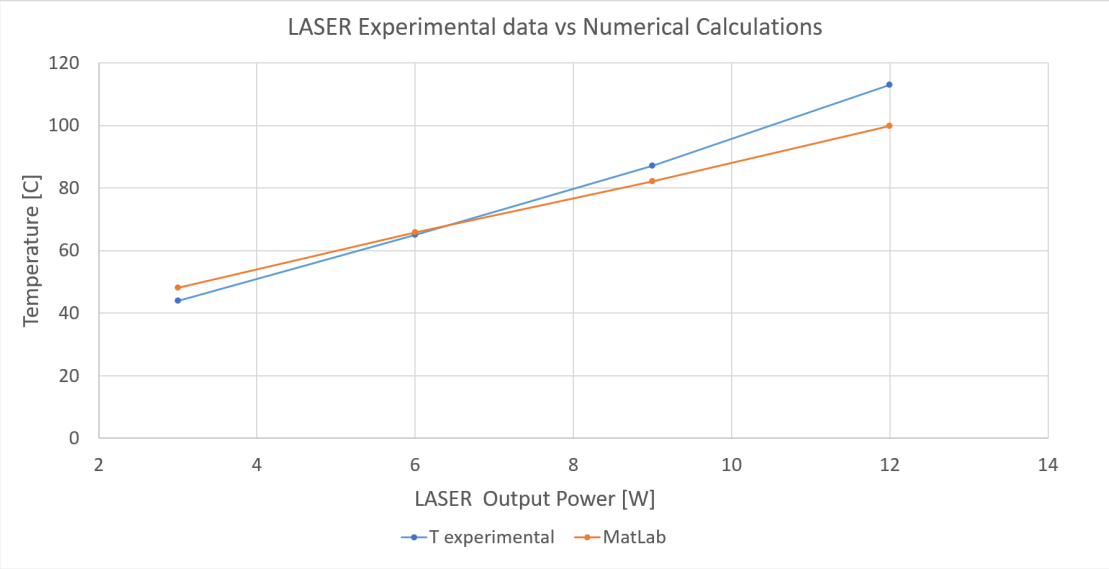

Figure 102: *Comparison between the measured temperature at several nominal LASER output energies (blue line) and the numerical calculation (orange line), performed at* 2.5 *µA,* 5 *µA,* 7.5 *µA and* 10 *µA, respectively.*

the incoming radiation. The slope of the two data-set is slightly different, but their trend is similar: both of them are linear, meaning that the heat diffusion mechanism is the one supposed in the calculations.
The described test was designed to give only qualitative information about the target/graphite system thermal behavior, yet, considering the experimental conditions, the agreement between theory and experimental data is certainly satisfying.
After the irradiation a black spot appeared where the LASER impinged, as it can be seen in figure 99. At first it could seem that the film was evaporated, but FESEM images proved that the film is still present. The darker appearance is given by small structural damages suffered by the droplets, shown in figure 103, which probably split due to the sudden strong heating.

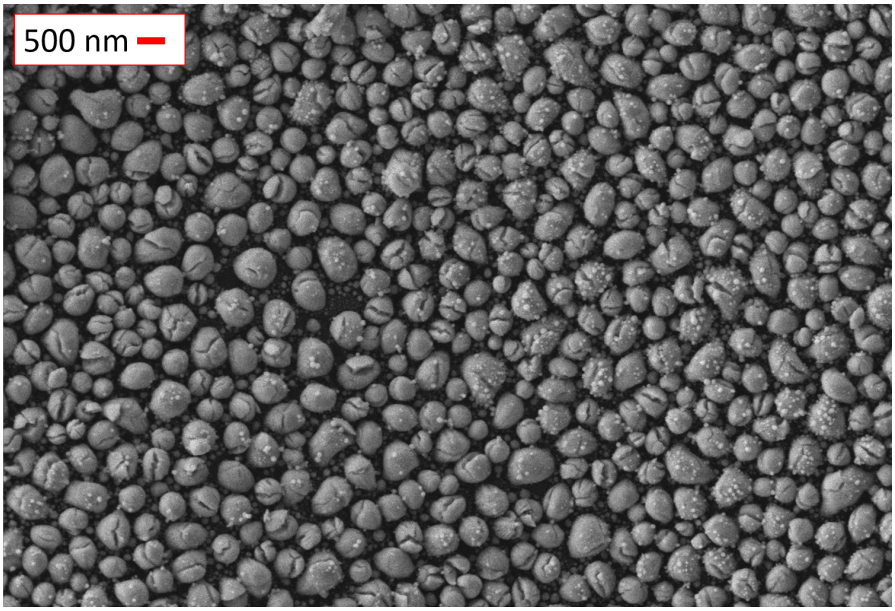

Figure 103: *Top view of the Sn target region irradiated with a LASER. The strong sudden absorbed power caused the fracture of the tin droplets, which cause the dark appearance. However, the material did not evaporate.*

7.2 BEAM TEST AT UNAM

The scope of the second test was more ambitious with respect to the first one. The greatest difference lies in the type of heat source, which now is an ion beam. The beam is composed by ^{12}C ions with charge state 3+, at the fixed energy of 3 MeV. The maximum intensity can reach up to 50 μA before the collimator, an aperture which shrinks the beam diameter to 3 mm, losing about 50% of the initial beam intensity. For a C ion, 3 MeV is too low of an energy for passing through the target/graphite; the beam fully stops inside the target, making the evaluation of the total deposited energy rather simple. Supposing a beam current of 1 μA, the number of ions is $\approx 2 \cdot 10^{12}$ ion/s; if each one of them deposits 3 MeV, then a 1 μA beam releases about 1 W of power in the target.
The used sample holder was a prototype of the design described in section 5.1. The material of choice was copper, due to its high conductivity and considerable thermal capacity. The two halves which compose the sample holder are shown disassembled in figure 104.

When the two pieces are joined together, they clamp tightly the graphite substrate; a hollow channel in correspondence with the target allows the passage of the beam. The liquid nitrogen can enter the circuit thanks to a pass-through flange; the inlets make the coolant enter the sample holder from the bottom, the outlets are instead placed on the top. This configuration, shown in figure 105, reduces the possibilities of forming bubbles in the circuit, which would hamper a smooth flow and, consequently, the cooling efficiency.

The scattering chamber, a picture of which is reported in figure 106, featured several detectors, namely a X-rays detector, Rutherford Backscattering Detector and a Faraday cup. The Faraday cup was placed right behind the target; it has been used to measure the effective intensity of the beam current and to check the integrity of the target itself. The temperature of the target was monitored with a thermal camera, placed outside the vacuum chamber, thanks to an IR-transparent Ge window 2 mm^2 large. Measurements were performed on graphite and Sn targets, at different beam intensities, while a Te target was used in another facility for different purposes (see section 7.2.3).

7.2.1 *Graphite target*

The graphite target was used to test the setup without using the liquid nitrogen circuit. The test on the functionality of the apparatus was performed

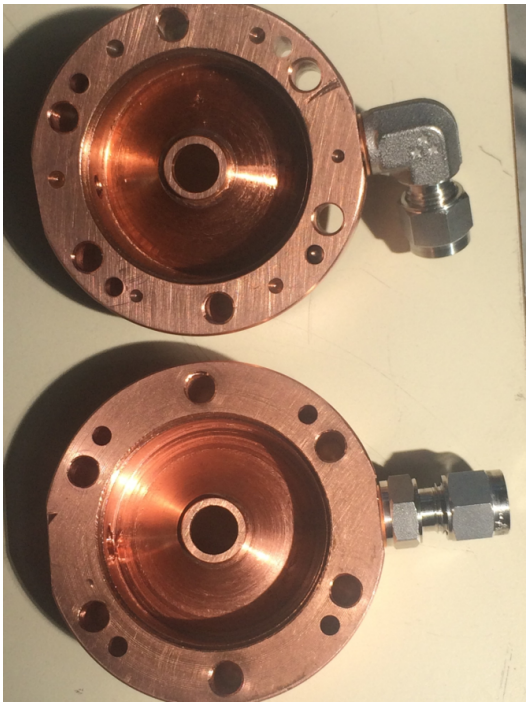

(a) *View of the sample holder chambers, in which LN_2 flows.*

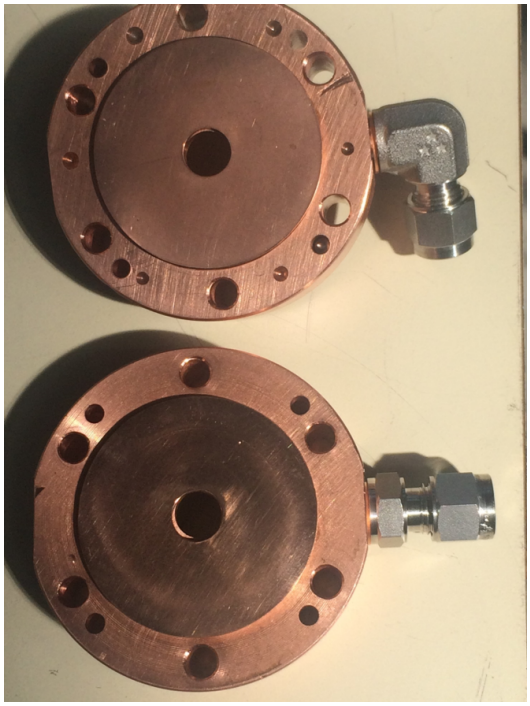

(b) *Actual appearance of the disassembled object. The two chambers are sealed by soldering a disk shaped cap.*

Figure 104: *Prototype of the LN_2 cooled sample holder. The two halves are joined by six screws; the inlets are clearly visible on the right-hand side of both of the images, the outlets are diametrically opposed to them. Most of the graphite surface is clamped and only the target is exposed.*

using beams of 3 μA and 5 μA, taking several measurements for each intensity. Some of these measurements were heavily affected by IR reflections and by the smallness of the IR window, resulting in not-coherent data: the final measured temperature was in fact the same even doubling the beam current. A better positioning and focusing of the thermal camera allowed to collect more reliable experimental data.

Although for just two different values of input power, the agreement between the expected and measured values is positive. The setup proved to work properly, so an actual target was used for the subsequent measurements.

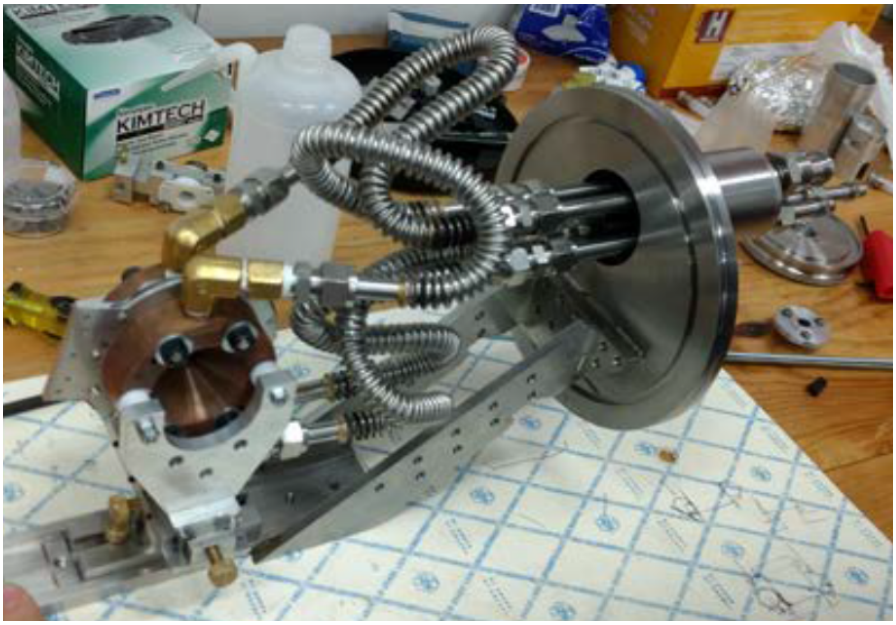

Figure 105: *A complete cooling setup. The target is clamped by the sample holder, which is fixed to the pass-through flange by a metal slab. Liquid nitrogen enters from the inlets placed at the bottom of the sample holder and exit from the upward outlets.*

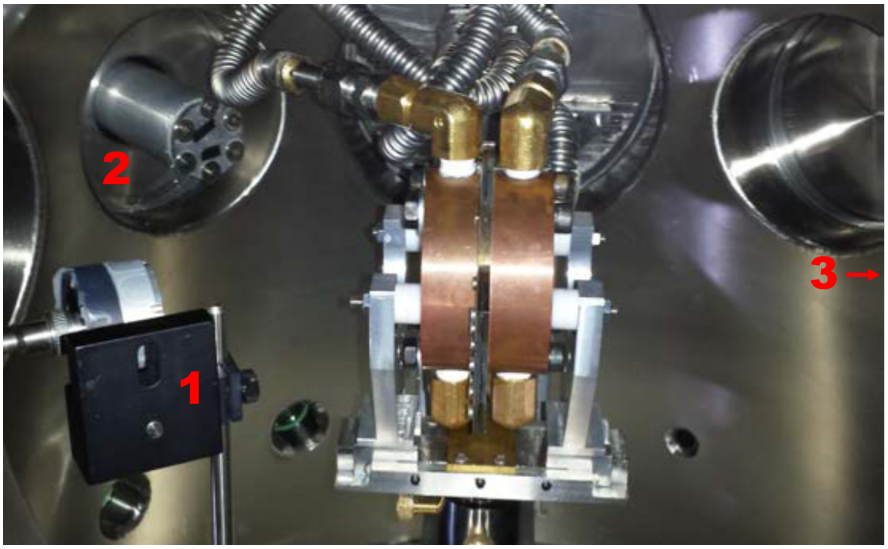

Figure 106: *A view of the inside of the vacuum chamber. Following the labels order, the detectors are: 1) Rutherford Backscattering Detector, 2) X-ray detector, 3) Faraday Cup (not shown).*

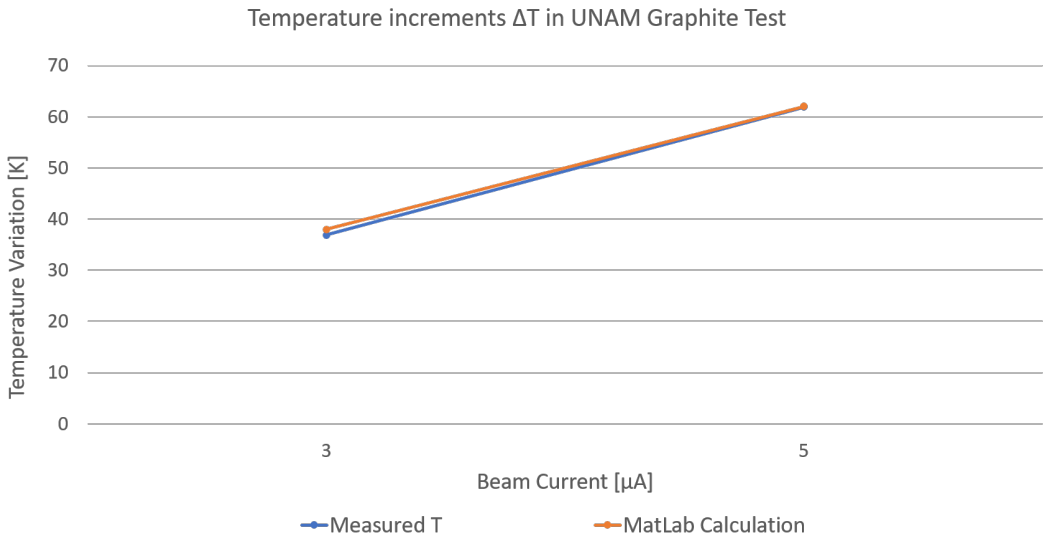

Figure 107: *Temperature increments measured at 3 μA and 5 μA of C ion beam, charged 3+, compared with numerical results obtained for the same input powers.*

7.2.2 *Tin target*

In this test, liquid nitrogen was used to cool down the target. It took about half an hour to bring the circuit to the LN_2 temperature, event which was signaled by the spilling of liquid nitrogen from the outlets. A reservoir of LN_2 was placed higher up with respect to the vacuum chamber, so that the fluid could flow into the circuit by gravity. A problem that could have been arisen concerns the structural changes which tin undergoes when cooled below 13.2 °C: it passes from the so-called β phase to the α phase, which has a lower density and higher brittleness [62]. The transition, commonly referred as 'tin pest' for its destructive effects, could cause the detachment from the substrate, thus compromising the target. However, a number of factors must concur to make the transition to happen, and such transition was not observed.
The thermal camera lower limit is $-40°$, therefore it cannot measure the lowest temperature reached by the system. Unfortunately, reflections and noise coming from the objects surrounding the sample hampered accurate measurements even when the target was close to be at room temperature. The target was in fact irradiated at several beam intensities, but for currents below 5 μA was not possible to collect any data. Only using a beam current of 5 μA and 7 μA the temperature rose enough to be measured. The measured values of the

Sn temperature are reported as a function of the beam current in figure 108, together with the numerical calculations.

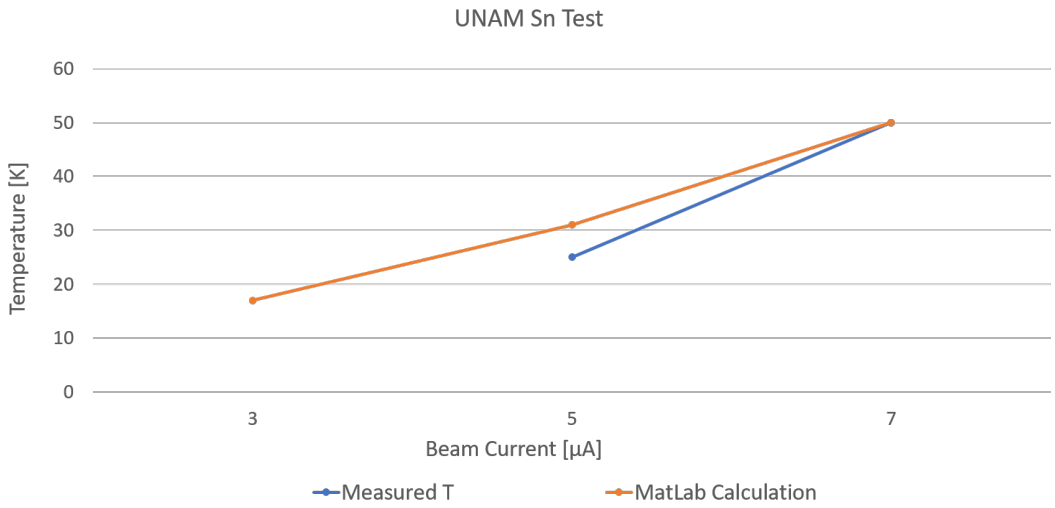

Figure 108: *Maximum temperatures measured at 5 μA and 7 μA of C ion beam, charged 3+, compared with numerical results obtained for the same input powers. For beam currents below 5 μA no data were collected, due to the low S/N ratio (low temperature of the target surrounded by warm objects).*

Like the previous test on graphite, the experimental values are in good agreement with the expected values. The experimental conditions at UNAM were closer to the actual NUMEN experiment than the ones of the first test, performed with a LASER in air; however, the beam had a too low energy to pass through the target, depositing its energy in the outer layers of the target. Despite the profile of the deposited energy differed from the one used in numerical evaluations, the data collected both with Sn and graphite target agreed satisfactorily with the expected ones.

7.2.3 *RBS at ININ*

A second C beam was also available in another facility, the Instituto Nacional de Investigaciones Nucleares (ININ). Here, the beam was much less intense with respect to UNAM, the maximum current peaking at 1 μA, but it had a higher energy, equal to 17 MeV and sufficient to pass through the target/-graphite system. The beam intensity was too low to perform a thermal stress

test, therefore this beam was used to perform a RBS measurement on a Te target.
The target was hosted in a simple sample holder made of two Cu disks, screwed together and connected to a heat sink (figure 109). In fact, even if the beam intensity was rather low, just 800 nA, the deposited power was around 4 W. The temperature, monitored with a thermal camera, did not changed from room temperature.

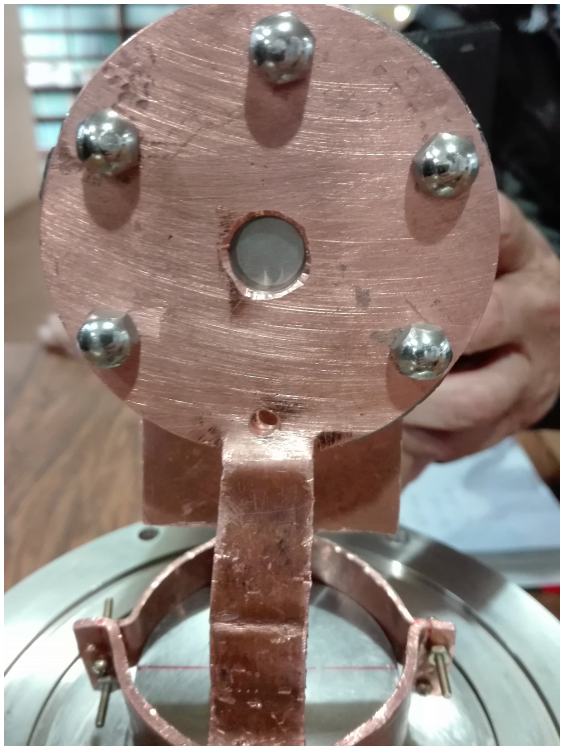

Figure 109: *Sample holder used at ININ to perform RBS measurements. The heat generated by the beam was dissipated in a cold sink.*

The measurement lasted for 20 minutes with an average of 400 particles collected per second on the Si detector. The detector was placed at $158,3°$ with respect to the beam axis. The thickness of the Te film was estimated using the software SIMNRA, resulting to be 612 nm, higher than the nominal value of 400 nm. The collected data and the simulated spectrum are shown in figure 110.

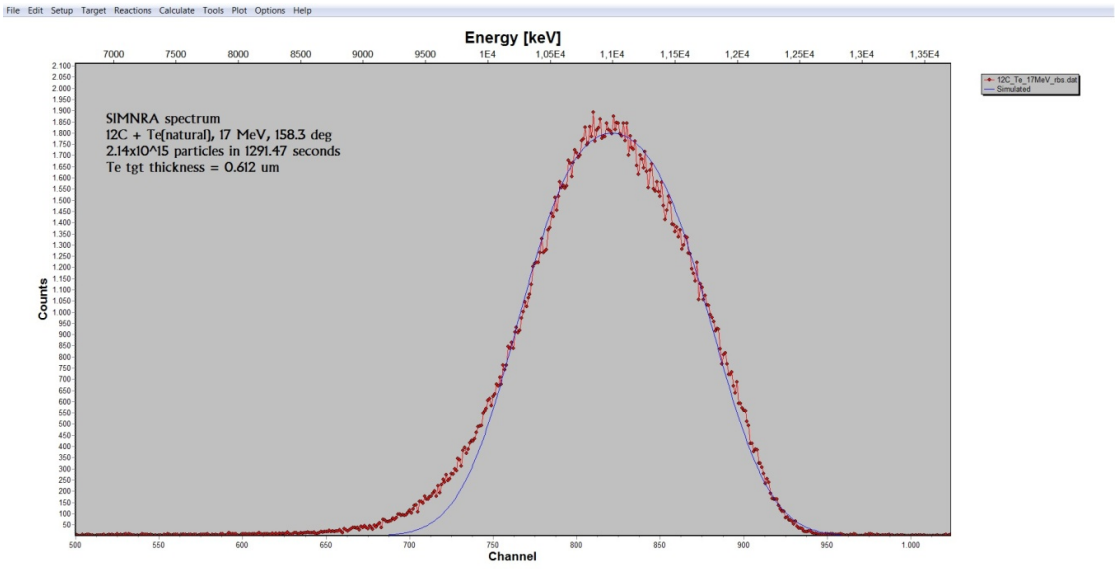

Figure 110: *RBS spectrum of a Te sample. The measured thickness was found to be* 612 *nm, higher than the nominal value of* 400 *nm. The thickness was calculated using the software SIMNRA.*

8

CONCLUSIONS

The NUMEN project aims to measure the cross section of a strong process, the Double Charge Exchange (DCE). The acquired information will be used to evaluate the Nuclear Matrix Elements (NME) of Neutrinoless Double β-Decay ($0\nu\beta\beta$), a process which involves weak mechanisms. Most of the isotopes studied in NUMEN are in fact used also in experiments searching for $0\nu\beta\beta$.
To collect a statistically significant amount of data, NUMEN will use high intensity ^{18}O and ^{20}Ne ion beams, up to a current of 50 μA. In order to preserve the resolution of the measurements, the thickness of the targets is limited to few hundreds of nm; the targets, however, must endure the high power densities deposited by the beam, that are on the order of $5 \cdot 10^5$ W/cm^2. Calculation showed that just clamping those target with a cold frame would not have been sufficient to dissipate the inlet power; to avoid overheating the target, it had been decided to use a highly conductive substrate made of Highly Oriented Pyrolytic Graphite (HOPG). This material, an allotrope form of carbon composed by stacks of graphene layers, possesses a thermal conductivity comparable to that of diamond ($\approx$2000 W/m·K) and is just 10 μm thick. Numerical calculations, performed with a code written in MatLab language, showed that targets made of Sn, Cd, Te and Ge are theoretically able to tolerate beam currents of 50 μA; a target of Se would be able to safely withstand 35 μA.
Numerical calculation was followed by the design of a sample holder effectively capable of dissipating the heat received by the graphite. The first designed cooling system is based on liquid nitrogen and has a very simple design, but it is more suited for testing than for the actual experiment; this is mainly due to the mechanical constraints on hosting and moving the LN_2 system inside the scattering chamber.
A second sample holder made of copper was designed to fit the cold finger of a cryocooler, a compact cooler able to maintain the sample stage at 40 K. This cooling system leaves more degrees of freedom in the positioning of the target inside the scattering chamber and allows to maintain the copper holder at a much lower cooling temperature. The temperature gap between the cryocooler cold finger (at 40 K) and the copper holder has been evaluated using the software COMSOL. Thanks to this software, the shape of the holder has been optimized and the gap has been calculated of the order of $\approx$ 10 K, showing a

good improvement with respect to the LN_2 system. Afterward, the production of Sn and Te target started, using Electron Beam Deposition (EBD) as deposition technique. A thorough study was performed to find the best deposition parameters, given the lack of literature and the peculiarity of the challenging substrate. For Sn films, heating the substrate during the deposition allows to obtain a flatter film; a further improvement in uniformity is given by the usage of a chromium buffer, which enhances the adhesion between the substrate and the film. A flat and uniform Te film was easier to achieve: in fact, whether deposited at room temperature or 100 °C, with or without a Cr buffer, results were satisfying. All of the produced samples were characterized using a FESEM microscope, to check the uniformity in the substrate coverage and thickness.

Finally, two experiments were performed to have some experimental comparison with the numerical calculations. The first one was aimed to test the heat conduction between a Sn target and the graphite substrate, which is fundamental for a good efficiency of the cooling system. A LASER, with a output power of several W, was used to heat the center of the target held by an Al sample holder. The test was performed in air with no cooling and several different LASER output powers. The agreement with theoretical calculations resulted to be very good, suggesting a proper functioning of the graphite substrate.

The second test was performed at UNAM, Mexico City, using a low energy, high intensity carbon ion beam. The test was performed in a vacuum chamber equipped with a number of detectors (RBS, X-ray, Faraday cup,...) and the temperature of the used graphite and Sn targets was monitored with a thermal camera. A liquid nitrogen cooled substrate was used to cool down the targets during irradiation. Again, the measured temperatures agreed quite good with the numerical calculations, validating the positive impact of the graphite substrate on the target heat resistance.

In a second facility, ININ, a low intensity C beam has been used to measure the effective thickness of a Te sample. The measured thickness resulted to be 612 nm, higher than the nominal value of 400 nm. No cooling was provided, yet the target temperature did not rise appreciably even if the beam was depositing 4 W of power during the RBS characterization.

Appendices

APPENDIX A

A.1 NUMERICAL SOLUTION OF THE HEAT EQUATION

The main function of the code is called *launcher.m*. Here, it is possible to choose the target material, the energy of the beam and its intensity; other parameters can be modified quite freely: graphite thickness, mesh density, cold temperature, etc. The heat generated inside the target and the HOPG substrate is calculated in the function *bethe_bloch*. Given a certain energy step dE, the function calculates the corresponding space interval dx using the Bethe-Bloch formula. The material physical and nuclear characteristics (density, specific heat, thermal conductivity, atomic and mass number) and the nuclear quantities of the ion beam (binding energy, atomic and mass number) are given by the functions *materials.m* and *ionbeam.m*, respectively.
After having selected the input parameters, a matrix called *dummyTemp* is created; it serves to calculate the derivatives of the temperature and, to this end, it has 2 extra mesh points along the r- and z-axis with respect to the actual temperature matrix dimension. The extra points are necessary to compute the second derivatives in the boundary points; in fact such derivatives, for the i^{th} point, need the $i-1^{th}$ and $i+1^{th}$ points. The temperature of the extra cells is later set equal to the boundary of the actual temperature matrix, in order to have no impact on the derivatives.
Lastly, two *for* loops contain the function designated for the calculation of the temperature equation, called *temp_function.m*. Such function is solved 10 times for each order of magnitude in time.

Listing A.1: *launcher.m is the main function of the code.*

```
1 %%%%% ——— Script for thermal analysis ——— %%%%
2
3 format long
4 clc
5
6 %%%—— Set ''target_name'' equal to: 116Sn, 116Cd, 76Se, 76Ge or 130
     Te ——%%%
7
```

```
target_name='116Sn';
Z_t=0.4e-3;          %[mm]

%%-- Substrate

Z_g=5e-3;            % graphite thickness [mm]

%%-- Set ''beam_type'' equal to: 18O, 18Ne, 20Ne, 20O, 12C, 28Si

beam_type='18O';
ion_energy= 15;  %[MeV/u]
current=50;      %[uA]
charge_state=8;

%%-- Select the parameters --%%

[G_heat, T_heat,rho_t,c_t,k_t]=bethe_bloch(target_name, ion_energy,
    current,beam_type, charge_state, Z_t, Z_g);

%%-- Parameters --%%

R_b=1;               % beam radius
R_t=5;               % target radius

Nr_in=R_b*10;           % integer number of elements in r, under
    beam
Nr_out=(R_t-R_b)*10;    % integer number of elements in r, outside
    beam
Nz_t=2;                % integer number of elements in z, target
Nz_g=23;               % integer number of elements in z, graphite
Nr_tot=Nr_out+Nr_in;
Nz_tot=Nz_t+Nz_g;
Tc=100;     % cold temperature [K]

dummyTemp=ones(Nr_tot+2, Nz_tot+2)*Tc;     % matrix of temperatures.
    The 2 extra cells per vector serve to allow the calculation of
    the second derivatives

```

```
%%% choose either to continue an old calculation or to start a new one
%[ dummyTemp ] = load_data( dummyTemp );

%%%-- Evaluate the Temperature
for N_time= 1e1
    for tenths=1:10

        [ Temp, dummyTemp ] =temp_function(T_heat,G_heat,
           target_name, beam_type, ion_energy, current, rho_t, c_t,
           k_t, Z_t, N_time,tenths,dummyTemp,R_b, R_t, Z_g, Nr_in,
           Nr_out, Nz_t, Nz_g, Nr_tot, Nz_tot, Tc);

    end
end

for N_time= [ 1e2 1e3 1e4 1e5 1e6 1e7 1e8  1e9]
    for tenths=2:10

        [ Temp, dummyTemp ] =temp_function(T_heat,G_heat,
           target_name, beam_type, ion_energy, current, rho_t, c_t,
           k_t, Z_t, N_time,tenths,dummyTemp,R_b, R_t, Z_g, Nr_in,
           Nr_out, Nz_t, Nz_g, Nr_tot, Nz_tot, Tc);

    end
end
```

Listing A.2: *bethe_bloch.m calculates the heat generated inside the target and the HOPG substrate.*

```
function[G_heat, T_heat,rho_t,c_t,k_t]=bethe_bloch(target_name, Ek_u, current, beam_type,  charge_state, Z_t, thick_g)

    %%%  space          ------> [mm]
    %%%  energy, mass   ------> [MeV]

    %%%--------- Constants----------%%%
    p_mass=938.271998;      % MeV
    n_mass=939.565413;      % MeV
```

```
9     m_e=0.511;              % MeV
10    e=1.60217662e-19;
11    Na=6.022e23;
12    c=29979245800;
13
14    %%%--- Medium Material ---%%%
15
16    [rho_t,c_t,k_t,A,Z]=materials(target_name);
17
18    %%%--- use these variables if using a different target than
          NUMEN ones
19    % rho= ; % g/cm^3
20    % A= ;
21    % Z= ;
22
23    %%%--- Substrate ---%%%
24
25    rho_g=2130e-9;
26    A_g=12;
27    Z_g=6;
28
29    %%%--- Projectile ---%%%
30
31    [a,z,n,E_b]=ionbeam(beam_type);
32
33    %%%--- use these variables if using a different projectiles than
          NUMEN ones
34    % E_b=92.161751;      % MeV       http://barwinski.net/isotopes/
          query_select.php
35    % z=6;
36    % a=12;
37    % n=a-z;
38
39    mass=z*p_mass+n*n_mass-E_b;      % MeV
40    Ek_tot=Ek_u*a;
41
42    %%%%% BEAM INTENSITY %%%%%%%%%%%
43
44    particles=current*1e-6/(charge_state*e);
```

```
45
46      %%%--------- Constants in Bethe-Bloch ----------%%%
47      K=0.307075e5; % 4*pi*Na*r_e^2*me
48      bc_t=K*rho_t*z^2*Z/A; % bethe bloch first factors for target
49      bc_g=K*rho_g*z^2*Z_g/A_g; % bethe bloch first factors for
           substrate
50      dE=0.00001; % MeV
51      I=0.000016*Z^0.9; % MeV
52      I_g=0.000016*Z_g^0.9; % MeV
53
54      %%%--------- Inizializing vectors ----------%%%
55      x=0;
56      i=1;
57
58      while x(i,1)<Z_t
59          E_tot(i,1)=Ek_tot(i,1)+mass;        % total energy of the
               projectile
60          beta(i,1)=sqrt(E_tot(i,1)^2-mass^2)/E_tot(i,1);
61          gamma(i,1)=sqrt(1/(1-beta(i,1)^2));
62          eta(i,1)=1-1.85*exp(-2*137*beta(i,1)/z^(2/3));
63          Tmax(i,1)=(gamma(i,1).*beta(i,1))^2/(1/(2*m_e)+gamma(i,1)/
               mass+m_e/(2*mass^2));
64          dEdx(i,1)=eta(i,1)*bc_t./beta(i,1)^2*(0.5*log(beta(i,1)^2*
               gamma(i,1)^2*Tmax(i,1)/I^2)-beta(i,1)^2);
65          dx=dE./dEdx(i,1);
66          i=i+1;
67          Ek_tot(i,1)=Ek_tot(i-1)-dE;
68          x(i,1)=x(i-1)+dx;
69      end
70
71      N_target=i-1; % functions points from 0 to N_target are within
           the target
72
73      while (x(i,1))<thick_g+Z_t
74          E_tot(i,1)=Ek_tot(i,1)+mass;
               % total energy of the projectile
75          beta(i,1)=sqrt(E_tot(i,1)^2-mass^2)/E_tot(i,1);
76          gamma(i,1)=sqrt(1/(1-beta(i,1)^2));
77          eta(i,1)=1-1.85*exp(-2*137*beta(i,1)/z^(2/3));
```

```
78          Tmax(i,1)=(gamma(i,1).*beta(i,1))^2/(1/(2*m_e)+gamma(i,1)/
                mass+m_e/(2*mass^2));
79          dEdx(i,1)=bc_g./beta(i,1)^2*(0.5*log(beta(i,1)^2*gamma(i,1)
                ^2*Tmax(i,1)/I_g^2)-beta(i,1)^2);
80          dx_gra=dE./dEdx(i,1);
81          i=i+1;
82          Ek_tot(i,1)=Ek_tot(i-1)-dE;
83          x(i,1)=x(i-1)+dx_gra;
84      end
85
86      N_tot=i-1;
87      N_gra=i-N_target;
88      Eloss_target=dE*(N_target);       % MeV lost by a single ion in
            target
89      Eloss_gra=dE*(N_gra);             % MeV lost by a single ion in
            graphite
90
91      T_heat=Eloss_target*e*1e6*particles;
92      G_heat=Eloss_gra*e*1e6*particles;
93      W_tot=G_heat+T_heat;
94
95  end
```

Listing A.3: *materials.m loads the material density, specific heat, thermal conductivity, atomic and mass number.*

```
1
2   function [rho,A,Z,E_b_tar]=materials( target_name )
3
4       if strcmp( target_name,'116Sn')==1
5
6           rho=7.310;          % target density [g/cm^3]
7           A=116;
8           Z=50;
9           E_b_tar=989;
10
11      elseif strcmp( target_name,'116Cd')==1
12
13          rho=8.650;          % target density [g/cm^3]
```

```
        A=116;
        Z=48;
        E_b_tar=987;

    elseif strcmp( target_name,'76Se')==1

        rho=4.819;          % target density [g/cm^3]
        A=76;
        Z=34;
        E_b_tar=662.0721;

    elseif strcmp( target_name,'76Ge')==1

        rho=5.323;          % target density [g/cm^3]
        A=76;
        Z=32;
        E_b_tar=661.5981;

    elseif strcmp( target_name,'130Te')==1

        rho=6.240;        % target density [g/cm^3]
        A=130;
        Z=52;
        E_b_tar=1095.942505;

    end

end
```

Listing A.4: *ionbeam.m loads the nuclear quantities of the ion beam.*

```
function [a,z,n,E_b]=ionbeam( projectile )

    if strcmp( projectile,'18O')==1

        E_b=139.807053;      % MeV    Total binding Energy
        z=8;
        a=18;
        n=a-z;
```

```
9
10      elseif strcmp( projectile,'20Ne')==1
11
12          E_b=160.644852;      % MeV
13          z=10;
14          a=20;
15          n=a-z;
16
17      elseif strcmp( projectile,'18Ne')==1
18
19          E_b=132.153488;      % MeV
20          z=10;
21          a=18;
22          n=a-z;
23
24      elseif strcmp( projectile,'20O')==1
25
26          E_b=151.370728;      % MeV
27          z=8;
28          a=20;
29          n=a-z;
30
31
32      elseif strcmp( projectile,'12C')==1
33
34          E_b=92.161751;      % MeV
35          z=6;
36          a=12;
37          n=a-z;
38
39
40      elseif strcmp( projectile,'28Si')==1
41
42          E_b=236.536880;      % MeV
43          z=14;
44          a=28;
45          n=a-z;
46      end
47
```

```
48 end
```

In the function *temp_function.m* the time and space infinitesimals are defined; in particular, the time interval is defined relatively to the space intervals, following the criteria for an explicit computational method.
The r- and z- axis are created using the function *vettori.m*, based on the mesh and space intervals. After having defined the axis, another function called *beam_heat.m* deals with the profile of the beam, creating a gaussian profile based upon the variables defined so far.
The core of the code is the *fast_central_deriv.m* function, which calculates the first and second derivatives along r- and z- coordinates. The values of the derivatives are then summed up in the temperature equation, together with the incoming heat. The equation is iteratively solved and the result of the current time step is then stored in a plot. The plot is automatically saved in two files, as a matrix of values and as a jpeg image.

Listing A.5: *temp_function.m solves the temperature equation.*

```
1
2  function [Temp, dummyTemp]= temp_function (T_heat,G_heat,
       target_name, beam_type, ion_energy, current, rho_t, c_t, k_t, Z_t
       , N_time,tenths,dummyTemp,R_b, R_t, Z_g, Nr_in, Nr_out, Nz_t,
       Nz_g, Nr_tot, Nz_tot, Tc)
3
4  %%% Function for temperature numerical solution
5
6  %%% physical parameters: units
7  % k=[J/(mm*s*K)]
8  % rho=[Kg/mm^3]
9  % c=[J/Kg*K]
10
11 k_gr=1950e-3;        %[J/(mm*s*K)]
12 k_gz=6e-3;           %[J/(mm*s*K)]
13 rho_g=2130e-9;       %[Kg/mm^3]
14 c_g=720;             %[J/Kg*K]
15
16 %%% geometrical parameters: units [mm]
17
18 dr_in=R_b/Nr_in;                          % infinitesimal distance
       in r, under beam
```

```
19 dr_out=(R_t-R_b)/Nr_out;                    % infinitesimal distance
       in r, outside beam
20 dz_t=Z_t/Nz_t;                              % infinitesimal distance
       in z, in target
21 dz_g=Z_g/Nz_g;                              % infinitesimal distance
       in z, in graphite
22 dt_values=0.25*[rho_t*c_t/k_t*dz_t^2 rho_t*c_t/k_t*dr_in^2 rho_g*c_g
      /k_gz*dz_g^2 rho_g*c_g/k_gr*dr_in^2];
23 dt=min(dt_values(dt_values>0));   % infinitesimal time interval for
      the explicit method with central derivatives
24
25 Calculation_length=dt*N_time*tenths;   % time covered by the code [s
      ]
26 Total_iter=N_time*tenths;
27
28 k_rhoc_r=zeros(Nr_tot,Nz_tot);
29 k_rhoc_z=zeros(Nr_tot,Nz_tot);
30 Dr=zeros(Nr_tot, Nz_tot);
31 D2r=zeros(Nr_tot, Nz_tot);
32 D2z=zeros(Nr_tot, Nz_tot);
33
34 [r,z]=vettori(R_b, Z_t,Nr_in, Nr_tot, Nz_t, Nz_tot,dr_in,dr_out,dz_t
      ,dz_g );
35
36 DQ=beam_heat(T_heat,G_heat,r,R_t,Z_t,Z_g, Nr_tot,Nz_tot, Nz_t,Nz_g,
      rho_t,c_t,rho_g,c_g,dr_in, dz_t,dz_g);   % gaussian heat in
      target and graphite
37
38 k_rhoc_r(1:Nr_tot,1:Nz_t)=k_t/(rho_t*c_t);
39 k_rhoc_r(1:Nr_tot,Nz_t+1:Nz_tot)=k_gr/(rho_g*c_g);
40 k_rhoc_z(1:Nr_tot,1:Nz_t)=k_t/(rho_t*c_t);
41 k_rhoc_z(1:Nr_tot,Nz_t+1:Nz_tot)=k_gz/(rho_g*c_g);
42
43 for iter=1:N_time
44
45 [Dr,D2r,D2z]=fast_central_deriv(Dr,D2r,D2z,Nr_tot,Nz_t,Nz_tot,dr_in,
      dz_t,dz_g,dummyTemp);   % function for the calculation of the
      derivatives along r and z.
46
```

```
%%%%% Temperature update %%%%%%

    Temp_Before=dummyTemp(:,:);

    for j=1:Nz_tot

        dummyTemp(2:Nr_tot+1,j+1)=Temp_Before(2:Nr_tot+1,j+1)+(
           k_rhoc_r(:,j).*(D2r(:,j)+Dr(:,j)./r(:))+k_rhoc_z(:,j).*
           D2z(:,j)+DQ(:,j)).*dt;    % Temperature update

    end

    dummyTemp(:,1)=dummyTemp(:,2);                  % boundary
       update
    dummyTemp(1,:)=dummyTemp(2,:);                  % boundary
       update
    dummyTemp(:,Nz_tot+2)=dummyTemp(:,Nz_tot+1);    % boundary
       update

%%%%%--------end of section---------------%%%%%

end

Temp=dummyTemp(2:Nr_tot+1,2:Nz_tot+1);

figure

surf(z*1e3,r,Temp,'FaceColor', 'interp')
colormap default
view(150, 40)

title_m1=['Target: ', num2str(target_name), ', ',num2str(Z_t*1e3), '
    \mum thick' ];
title_m2=['Beam: ',num2str(current), ' \muA of ', beam_type, ' ions
   at ', num2str(ion_energy),' MeV/nucleon'];
title_m3=['Time span: ',num2str(Calculation_length), ' s, ', 'dt=',
   num2str(dt), ' s '];

title({title_m1; title_m2; title_m3})
```

```
78 xlabel('Depth [\mum]')
79 ylabel('Radius [mm]')
80 zlabel('Temperature [K]')
81
82 filename = [num2str(target_name), '_',num2str(Z_t*1e6), 'nm_',
      num2str(ion_energy), 'MeV_',num2str(current), 'uA_',num2str(
      Total_iter),'iter'];
83 saveas(gca, [pwd '\Plots\' filename '.fig']);
84 saveas(gca, [pwd '\Plots\' filename '.jpg']);
85
86 close all
87
88 end
```

Listing A.6: *vettori.m creates the r- and z-axis.*

```
1  function [ r,z] = vettori(R_b, Z_t,Nr_in, Nr_tot, Nz_t, Nz_tot,dr_in
       ,dr_out,dz_t,dz_g )
2
3  %
4
5  r=ones(Nr_tot,1);
6  z=ones(Nz_tot,1);
7  %t=ones(N_time,1);
8
9      %%% r
10
11     for i=1:Nr_in
12         r(i)=(i-0.5)*dr_in;
13     end
14
15     for i=Nr_in+1:Nr_tot
16         r(i)=R_b+(i-Nr_in-0.5)*dr_out;
17     end
18
19     %%% z
20
21     for j=1:Nz_t
22         z(j)=(j-0.5)*dz_t;
```

```
    end

    for j=Nz_t+1:Nz_tot
        z(j)=Z_t+(j-Nz_t-0.5)*dz_g;
    end

    %%% t

%     for l=1:N_time
%         t(l)=(l-1)*dtime;
%     end
end
```

Listing A.7: *beam_heat.m creates the gaussian profile of the beam based on the input parameters.*

```
function [ DQ ] = beam_heat(T_heat,G_heat,r,R_t,Z_t,Z_g, Nr_tot,
   Nz_tot, Nz_t,Nz_g,rho_t,c_t,rho_g,c_g,dr_in, dz_t,dz_g)

DQ=zeros(Nr_tot,Nz_tot);

sigma=1;

qt=T_heat/(sigma^2*(1-exp(-0.5*(R_t/sigma)^2))*Z_t*2*pi); % [J/(s*mm
   ^3)] gaussian's maximum height in target
qg=G_heat/(sigma^2*(1-exp(-0.5*(R_t/sigma)^2))*Z_g*2*pi); % [J/(s*mm
   ^3)] gaussian's maximum height in graphite

E_gauss_t=qt*exp(-r.^2/(2*sigma^2));   % [J/(s*mm^3)] gaussian
   density over r in target
E_gauss_g=qg*exp(-r.^2/(2*sigma^2));   % [J/(s*mm^3)] gaussian
   density over r in graphite

J1=sum(E_gauss_t.*r*2*pi*dr_in*dz_t)*Nz_t;     % [J/s] total heat in
    target
J2=sum(E_gauss_g.*r*2*pi*dr_in*dz_g)*Nz_g;     % [J/s] total heat in
    graphite

    for j=1:Nz_t
```

```
17
18          DQ(1:Nr_tot,j)=E_gauss_t(1:Nr_tot)/(rho_t*c_t);   % [K/s]
               temperature rise in target
19
20      end
21
22      for j=Nz_t+1:Nz_tot
23
24          DQ(1:Nr_tot,j)=E_gauss_g(1:Nr_tot)/(rho_g*c_g);   % [K/s]
               temperature rise in graphite
25
26      end
27
28  end
```

Listing A.8: *fast_central_deriv.m calculates the derivatives along r- and z-coordinates.*

```
1   function [Dr,D2r,D2z]=fast_central_deriv(Dr,D2r,D2z,Nr_tot,Nz_t,
       Nz_tot,dr_in,dz_t,dz_g,dummyTemp )
2
3       % columns first, through all the range
4
5       % target region
6
7       for j=1:Nz_t-1
8           j4T=j+1;
9
10          Dr(:,j)=(dummyTemp(3:Nr_tot+2,j4T)-dummyTemp(1:Nr_tot,j4T))
               /(2*dr_in);
11          D2r(:,j)=(dummyTemp(3:Nr_tot+2,j4T)-2*dummyTemp(2:Nr_tot+1,
               j4T)+dummyTemp(1:Nr_tot,j4T))/dr_in^2;
12          D2z(:,j)=(dummyTemp(2:Nr_tot+1,j4T+1)-2*dummyTemp(2:Nr_tot
               +1,j4T)+dummyTemp(2:Nr_tot+1,j4T-1))/dz_t^2;
13
14      end
15
16      % target-graphite interface
17
```

```
18          j=Nz_t;
19          j4T=j+1;
20
21          Dr(:,j)=(dummyTemp(3:Nr_tot+2,j4T)-dummyTemp(1:Nr_tot,j4T))
                /(2*dr_in);
22          D2r(:,j)=(dummyTemp(3:Nr_tot+2,j4T)-2*dummyTemp(2:Nr_tot+1,
                j4T)+dummyTemp(1:Nr_tot,j4T))/dr_in^2;
23          D2z(:,j)=(dummyTemp(2:Nr_tot+1,j4T+1)/dz_g-(1/dz_g+1/dz_t)*
                dummyTemp(2:Nr_tot+1,j4T)+dummyTemp(2:Nr_tot+1,j4T-1)/
                dz_t)/dz_t;
24
25      % graphite region
26
27      for j=Nz_t+1:Nz_tot
28          j4T=j+1;
29
30          Dr(:,j)=(dummyTemp(3:Nr_tot+2,j4T)-dummyTemp(1:Nr_tot,j4T))
                /(2*dr_in);
31          D2r(:,j)=(dummyTemp(3:Nr_tot+2,j4T)-2*dummyTemp(2:Nr_tot+1,
                j4T)+dummyTemp(1:Nr_tot,j4T))/dr_in^2;
32          D2z(:,j)=(dummyTemp(2:Nr_tot+1,j4T+1)-2*dummyTemp(2:Nr_tot
                +1,j4T)+dummyTemp(2:Nr_tot+1,j4T-1))/dz_g^2;
33
34      end
35
36  end
```

A.2 MONTE CARLO CODE

The calculation of the total energy resolution of DCE reactions has been performed with a Monte Carlo code. The main code is called *Resolution.m*; here the constants are initialized and it is possible to choose the target material, thickness and non uniformity. It is possible to add a graphite substrate, with its own thickness non uniformity. All of the superficial non uniformity are supposed to follow a gaussian distribution, with a certain σ_{target} or $\sigma_{graphite}$.
After having chosen the parameters, the functions *Materials.m*, *ion$_b$eam.m* and *masses.m* calculates all the quantities necessary for the calculation.
It is possible to choose the number of particles, which is also the number of

iterations the code will perform. For each particle, the code works as follows. The effective path that the particle will travel is calculated by adding to the average thickness of the target a random number which follow a gaussian distribution with σ equal to σ_{target}. Same speech for the graphite, but for the σ which is equal to $\sigma_{graphite}$. In the newly calculated target thickness, the depth at which the DCE reaction occurs is sorted randomly (it does not depend on the target thickness).
The average energy loss and the straggling are calculated up to the reaction point by using the Bethe Bloch formula and the Gaussian model, respectively. The energy at which the DCE reaction occurs is calculated by adding a random number, which follows the straggling gaussian distribution, to the average energy loss.

Listing A.9: *Resolution.m is the main code in which all the contribution to the total energy resolution are calculated.*

```
function [Dr,D2r,D2z]=fast_central_deriv(Dr,D2r,D2z,Nr_tot,Nz_t,
   Nz_tot,dr_in,dz_t,dz_g,dummyTemp )

    % columns first, through all the range

    % target region

    for j=1:Nz_t-1
        j4T=j+1;

        Dr(:,j)=(dummyTemp(3:Nr_tot+2,j4T)-dummyTemp(1:Nr_tot,j4T))
           /(2*dr_in);
        D2r(:,j)=(dummyTemp(3:Nr_tot+2,j4T)-2*dummyTemp(2:Nr_tot+1,
           j4T)+dummyTemp(1:Nr_tot,j4T))/dr_in^2;
        D2z(:,j)=(dummyTemp(2:Nr_tot+1,j4T+1)-2*dummyTemp(2:Nr_tot
           +1,j4T)+dummyTemp(2:Nr_tot+1,j4T-1))/dz_t^2;

    end

    % target-graphite interface

        j=Nz_t;
        j4T=j+1;

```

```
21          Dr(:,j)=(dummyTemp(3:Nr_tot+2,j4T)-dummyTemp(1:Nr_tot,j4T))
                /(2*dr_in);
22          D2r(:,j)=(dummyTemp(3:Nr_tot+2,j4T)-2*dummyTemp(2:Nr_tot+1,
                j4T)+dummyTemp(1:Nr_tot,j4T))/dr_in^2;
23          D2z(:,j)=(dummyTemp(2:Nr_tot+1,j4T+1)/dz_g-(1/dz_g+1/dz_t)*
                dummyTemp(2:Nr_tot+1,j4T)+dummyTemp(2:Nr_tot+1,j4T-1)/
                dz_t)/dz_t;
24
25      % graphite region
26
27      for j=Nz_t+1:Nz_tot
28          j4T=j+1;
29
30          Dr(:,j)=(dummyTemp(3:Nr_tot+2,j4T)-dummyTemp(1:Nr_tot,j4T))
                /(2*dr_in);
31          D2r(:,j)=(dummyTemp(3:Nr_tot+2,j4T)-2*dummyTemp(2:Nr_tot+1,
                j4T)+dummyTemp(1:Nr_tot,j4T))/dr_in^2;
32          D2z(:,j)=(dummyTemp(2:Nr_tot+1,j4T+1)-2*dummyTemp(2:Nr_tot
                +1,j4T)+dummyTemp(2:Nr_tot+1,j4T-1))/dz_g^2;
33
34      end
35
36  end
```

Listing A.10: *materials.m loads the material density, binding energy, atomic and mass number.*

```
1
2   function [rho,A,Z,E_b_tar]=materials( target_name )
3
4       if strcmp( target_name,'116Sn')==1
5
6           rho=7.310;          % target density [g/cm^3]
7           A=116;
8           Z=50;
9           E_b_tar=989;
10
11      elseif strcmp( target_name,'116Cd')==1
12
```

```
        rho=8.650;          % target density [g/cm^3]
        A=116;
        Z=48;
        E_b_tar=987;

    elseif strcmp( target_name,'76Se')==1

        rho=4.819;          % target density [g/cm^3]
        A=76;
        Z=34;
        E_b_tar=662.0721;

    elseif strcmp( target_name,'76Ge')==1

        rho=5.323;          % target density [g/cm^3]
        A=76;
        Z=32;
        E_b_tar=661.5981;

    elseif strcmp( target_name,'130Te')==1

        rho=6.240;        % target density [g/cm^3]
        A=130;
        Z=52;
        E_b_tar=1095.942505;

    end

end
```

Listing A.11: *ionbeam.m loads the nuclear quantities of the ion beam.*

```
function [a,z,n,E_b]=ionbeam( projectile )

    if strcmp( projectile,'18O')==1

        E_b=139.807053;      % MeV    Total binding Energy
        z=8;
        a=18;
```

```
8           n=a-z;
9
10      elseif strcmp( projectile,'20Ne')==1
11
12          E_b=160.644852;      % MeV
13          z=10;
14          a=20;
15          n=a-z;
16
17      elseif strcmp( projectile,'18Ne')==1
18
19          E_b=132.153488;      % MeV
20          z=10;
21          a=18;
22          n=a-z;
23
24      elseif strcmp( projectile,'20O')==1
25
26          E_b=151.370728;      % MeV
27          z=8;
28          a=20;
29          n=a-z;
30
31
32      elseif strcmp( projectile,'12C')==1
33
34          E_b=92.161751;      % MeV
35          z=6;
36          a=12;
37          n=a-z;
38
39
40      elseif strcmp( projectile,'28Si')==1
41
42          E_b=236.536880;      % MeV
43          z=14;
44          a=28;
45          n=a-z;
46      end
```

```
47
48 end
```

Listing A.12: *masses.m calculates the masses in MeV of the nuclei involved in the reaction.*

```
1
2  function [m_proj, m_ejec, m_tar1, m_tar2]=masses(target_name)
3
4  global p_mass n_mass z_ejec
5
6      if strcmp( target_name,'116Sn')==1
7
8          A_tar1=116;
9          Z_tar1=50;
10         E_b_tar1=989;
11         A_tar2=116;
12         Z_tar2=48;
13         E_b_tar2=987;
14         E_b_proj=139.807053;      % MeV    Total binding Energy
15         z_proj=8;
16         a_proj=18;
17         E_b_ejec=132.153488;      % MeV
18         z_ejec=10;
19         a_ejec=18;
20
21
22     elseif strcmp( target_name,'116Cd')==1
23
24         A_tar1=116;
25         Z_tar1=48;
26         E_b_tar1=987;
27         A_tar2=116;
28         Z_tar2=50;
29         E_b_tar2=989;
30         E_b_proj=160.644852;      % MeV
31         z_proj=10;
32         a_proj=20;
33         E_b_ejec=151.370728;      % MeV
```

```
34          z_ejec=8;
35          a_ejec=20;
36
37      elseif strcmp( target_name,'76Se')==1
38
39          A_tar1=76;
40          Z_tar1=34;
41          E_b_tar1=662.0721;
42          A_tar2=76;
43          Z_tar2=32;
44          E_b_tar2=661.5981;
45          E_b_proj=139.807053;      % MeV    Total binding Energy
46          z_proj=8;
47          a_proj=18;
48          E_b_ejec=132.153488;      % MeV
49          z_ejec=10;
50          a_ejec=18;
51
52      elseif strcmp( target_name,'76Ge')==1
53
54          A_tar1=76;
55          Z_tar1=32;
56          E_b_tar1=661.5981;
57          A_tar2=76;
58          Z_tar2=34;
59          E_b_tar2=662.0721;
60          E_b_proj=160.644852;      % MeV
61          z_proj=10;
62          a_proj=20;
63          E_b_ejec=151.370728;      % MeV
64          z_ejec=8;
65          a_ejec=20;
66
67      elseif strcmp( target_name,'130Te')==1
68
69          A_tar1=130;
70          Z_tar1=52;
71          E_b_tar1=1095.942505;
72          A_tar2=130;
```

```
        Z_tar2=54;
        E_b_tar2=1096.906738;
        E_b_proj=160.644852;      % MeV
        z_proj=10;
        a_proj=20;
        E_b_ejec=151.370728;      % MeV
        z_ejec=8;
        a_ejec=20;

    end


m_proj=z_proj*p_mass+(a_proj-z_proj)*n_mass-E_b_proj;      % MeV
m_ejec=z_ejec*p_mass+(a_ejec-z_ejec)*n_mass-E_b_ejec;
m_tar1=Z_tar1*p_mass+(A_tar1-Z_tar1)*n_mass-E_b_tar1;
m_tar2=Z_tar2*p_mass+(A_tar2-Z_tar2)*n_mass-E_b_tar2;

end
```

Listing A.13: *twobody.m calculates the energy of the ejectile after the DCE reaction.*

```

%%%%%%%%  two body kinematics DCE

function [E_ejec]=twobody(m_proj, m_ejec, m_tar1, m_tar2, theta,
   E_proj)

p_proj=((E_proj+m_proj)^2-m_proj^2)^0.5;
E_i=(p_proj^2+m_proj^2)^0.5+m_tar1;
beta_i=p_proj/E_i;
d=(E_i^2+m_ejec^2-m_tar2^2-p_proj^2)/(2*E_i);
c=m_ejec^2-d^2;
a=1-beta_i^2*(cos(theta))^2;
b=d*beta_i*cos(theta);
discrim=b^2-a*c;
p_ejec=(b+(abs(discrim))^0.5)/a;
E_ejec=(p_ejec^2+m_ejec^2)^0.5-m_ejec;


```

```
18 end
```

The energy of the reaction product is calculated in the function *twobody.m*. Afterward, the new particle crosses the remaining portion of the target. Its final energy is calculated as before the reaction (average energy loss + random straggling value). If the substrate is present, the particle final energy will be again the average energy loss plus a random number coming from the straggling.
This procedure is repeated for each particle and the final energy distribution is plotted in a histogram.

A.3 SOLUTION OF THE HEAT EQUATION IN THE CLAMPED REGION OF THE NUMEN TARGET

Referring to figure 15 of Chapter 3, we shall study the temperature during the heat transfer from the red part to the blue through the yellow region of one side of the target, under the following hypotheses:

a) After an initial transient, the system reaches a thermodynamic steady state;

b) The internal conductivity coefficient is isotropic inside the target;

c) The temperatures of the heated (red) target Θ_{Hot} and of the cooled (blue) regions Θ_{Cold} are constant and uniform. Also the light-blue corners are at constant temperature Θ_{Cold};

d) The side of each yellow region opposite to the one adjacent to the red region is maintained at constant temperature, since the 2 cold frames are very close to each other (nearly touching because s is of the order of ≈ 400 nm);

The equation that must be solved is:

$$\frac{\partial^2\Theta}{\partial x^2} + \frac{\partial^2\Theta}{\partial y^2} + \frac{\partial^2\Theta}{\partial z^2} = 0 \tag{A.3.1}$$

The B.C. of the problem are listed in the above points a, b, c, d. It is convenient to shift the temperature scale by an offset equal to Θ_{Cold}, i.e. to search for the temperature T(x,y,z) defined as:

$$T(x,y,z) = \Theta(x,y,z) - \Theta_{Cold} \tag{A.3.2}$$

which obviously satisfies the same Laplace equation:

$$\frac{\partial^2 T}{\partial x^2} + \frac{\partial^2 T}{\partial y^2} + \frac{\partial^2 T}{\partial z^2} = 0 \tag{A.3.3}$$

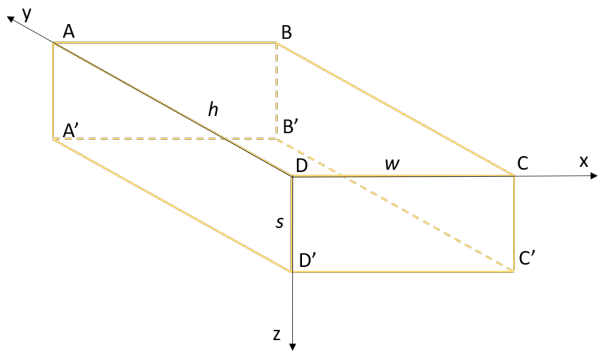

Figure A.3.1: *something*

Taking a reference system as in figure A.3.1, the B.C. become $T = \Theta_{Hot} - \Theta_{Cold}$ on the surface CBB'C' and $T = 0$ on the other 5 surfaces, i.e.:

$$\begin{aligned} &\Theta(x = 0, y, z) = \Theta_{Cold} \rightarrow T(x = 0, y, z) = 0 \\ &\Theta(x = w, y, z) = \Theta_{Hot} \rightarrow T(x = w, y, z) = \Theta_{Hot} - \Theta_{Cold} \end{aligned} \tag{A.3.4a}$$

$$\begin{aligned} &\Theta(x, y = 0, z) = \Theta_{Cold} \rightarrow T(x, y = 0, z) = 0 \\ &\Theta(x, y = h, z) = \Theta_{Hot} \rightarrow T(x, y = h, z) = 0 \end{aligned} \tag{A.3.4b}$$

$$\begin{aligned} &\Theta(x, y, z = 0) = \Theta_{Cold} \rightarrow T(x, y, z = 0) = 0 \\ &\Theta(x, y, z = s) = \Theta_{Hot} \rightarrow T(x, y, z = s) = 0 \end{aligned} \tag{A.3.4c}$$

Let us search for a solution as a product of the type:

$$T(x, y, z) = X(x) \cdot Y(y) \cdot Z(z) \tag{A.3.5}$$

Inserting equation A.3.5 in equation A.3.3 one obtains:

$$\frac{1}{X(x)} \frac{d^2 X(x)}{dx^2} + \frac{1}{Y(y)} \frac{d^2 Y(y)}{dy^2} + \frac{1}{Z(z)} \frac{d^2 Z(z)}{dz^2} = 0 \tag{A.3.6}$$

To satisfy the above equation each term in (8) must be equal to a constant:

$$\frac{1}{X(x)} \frac{d^2 X(x)}{dx^2} = \alpha; \tag{A.3.7a}$$

$$\frac{1}{Y(y)}\frac{d^2Y(y)}{dy^2} = \beta; \tag{A.3.7b}$$

$$\frac{1}{Z(z)}\frac{d^2Z(z)}{dz^2} = \gamma \tag{A.3.7c}$$

with $\alpha + \beta + \gamma = 0$. It must be remarked that at least one constant must be negative and at least one must be positive. Each equation A.3.7 has solutions depending on the positive or negative value of the constants:

$$\begin{aligned}
&\alpha > 0 \rightarrow X(x) = a \cdot e^{-\sqrt{\alpha}\cdot x} + b \cdot e^{\sqrt{\alpha}\cdot x} \\
&\alpha < 0 \rightarrow X(x) = a \cdot \sin(\sqrt{-\alpha}\cdot x) + b \cdot \cos(\sqrt{-\alpha}\cdot x) \\
&\beta > 0 \rightarrow Y(y) = a \cdot e^{-\sqrt{\beta}\cdot y} + b \cdot e^{\sqrt{\beta}\cdot y} \\
&\beta < 0 \rightarrow Y(y) = a \cdot \sin(\sqrt{-\beta}\cdot y) + b \cdot \cos(\sqrt{-\beta}\cdot y) \\
&\gamma > 0 \rightarrow Z(z) = a \cdot e^{-\sqrt{\gamma}\cdot z} + b \cdot e^{\sqrt{\gamma}\cdot z} \\
&\gamma < 0 \rightarrow Z(z) = a \cdot \sin(\sqrt{-\gamma}\cdot z) + b \cdot \cos(\sqrt{-\gamma}\cdot z)
\end{aligned} \tag{A.3.8}$$

To choose which constants are positive or negative, it must be remarked that the Boundary Conditions on x are asymmetric, while those ones on y and z are symmetric. This suggests to use the exponential form (asymmetric) for X(x) and the trigonometric form (symmetric) for Y(y) and Z(z). In fact, applying the exponential function to Y(y) in A.3.8, the B.C. A.3.4b in y=0 and y=h require:

$$X(x)\cdot Y(0)\cdot Z(z) = X(x)\cdot Y(h)\cdot Z(z) = 0 \rightarrow Y(0) = Y(h) = 0 \tag{A.3.9}$$

The last 2 equalities in A.3.9 imply: $a = -b$ and $a = -be^{-2\sqrt{\beta}\cdot h}$, which are inconsistent. Same speech applies for Z(z), therefore trigonometric solutions are chosen for both Y(y) and Z(z):

$$\begin{aligned}
Y(y) &= a \cdot \sin(\sqrt{-\beta}\cdot y) + b \cdot \cos(\sqrt{-\beta}\cdot y) \\
Z(z) &= c \cdot \sin(\sqrt{-\gamma}\cdot z) + d \cdot \cos(\sqrt{-\gamma}\cdot z)
\end{aligned} \tag{A.3.10}$$

In order to satisfy the B.C. in y and z we must require that equation A.3.10 satisfies such B.C., obtaining:

$$\begin{aligned}
Y(0) = 0 &= a \cdot \sin(\sqrt{-\beta}\cdot 0) + b \cdot \cos(\sqrt{-\beta}\cdot 0) \rightarrow b = 0 \\
Z(0) = 0 &= c \cdot \sin(\sqrt{-\gamma}\cdot 0) + d \cdot \cos(\sqrt{-\gamma}\cdot 0) \rightarrow d = 0
\end{aligned} \tag{A.3.11}$$

Therefore Y(y) and Z(z) are *sin* functions only. Moreover, the B.C. require:

$$\begin{aligned} Y(h) = 0 = a \cdot \sin(\sqrt{-\beta} \cdot h) \rightarrow \sqrt{-\beta} \cdot h = m\pi \rightarrow -\beta_m = \frac{m^2\pi^2}{h^2} \\ Z(s) = 0 = c \cdot \sin(\sqrt{-\gamma} \cdot s) \rightarrow \sqrt{-\gamma} \cdot s = n\pi \rightarrow -\gamma_n = \frac{n^2\pi^2}{s^2} \end{aligned} \tag{A.3.12}$$

In A.3.14 m and n are integers (different from 0). Recalling that $\alpha_{mn} = -\beta_m - \gamma_n = (\frac{m^2}{h^2} + \frac{n^2}{s^2})\pi^2 > 0$ we can write:

$$X(x) = a \cdot e^{-\sqrt{\alpha_{mn}} \cdot x} + b \cdot e^{\sqrt{\alpha_{mn}} \cdot x} \tag{A.3.13}$$

and, applying the first B.C. A.3.4a in x = 0, we get:

$$X(0) = 0 = a + b \rightarrow X(x) = b \cdot (e^{\sqrt{\alpha_{mn}} \cdot x} - e^{-\sqrt{\alpha_{mn}} \cdot x}) \tag{A.3.14}$$

Every function $T_{mn}(x, y, z) = b_{mn} \cdot \sin\left(\frac{m\pi}{h} y\right) \cdot \sin\left(\frac{n\pi}{s} z\right) \cdot (e^{\sqrt{\alpha_{mn}} \cdot x} - e^{-\sqrt{\alpha_{mn}} \cdot x})$ is a solution of A.3.3. The general solution is a linear combination:

$$T(x, y, z) = \sum_{\substack{m=1 \\ n=1}}^{\infty} b_{mn} \cdot \sin\left(\frac{m\pi}{h} y\right) \cdot \sin\left(\frac{n\pi}{s} z\right) \cdot (e^{\sqrt{\alpha_{mn}} \cdot x} - e^{-\sqrt{\alpha_{mn}} \cdot x}) \tag{A.3.15}$$

Remark: in principle, the range of the integer indexes is: $-\infty < m, n < \infty$. Since the temperature cannot be negative for all x values, m and n cannot have opposite sign. On the other hand, if their sign is the same, the terms of the series A.3.16 with negative signs have the same values of the corresponding positive ones (remember that the exponents contain only squared m and n). Therefore the meaningful index domain is $1 \leq m, n \leq \infty$. The coefficients b_{mn} are to be found from the B.C. Let us apply the second B.C. of A.3.4a on the surface $x = w$ for all y and z:

$$T(w, y, z) = \sum_{\substack{m=1 \\ n=1}}^{\infty} b_{mn} \cdot \sin\left(\frac{m\pi}{h} y\right) \cdot \sin\left(\frac{n\pi}{s} z\right) \cdot (e^{\sqrt{\alpha_{mn}} \cdot w} - e^{-\sqrt{\alpha_{mn}} \cdot w}) = T_{hot} \tag{A.3.16}$$

In order to obtain the values of the coefficients b_{mn} we can integrate equation A.3.16 in dy and dz over the whole surface $x = w$, using the orthogonality of the functions $\sin(\frac{m\pi}{h} y)$ in the domain $0 \leq y \leq h$ and $\sin(\frac{n\pi}{s} z)$ in the domain $0 \leq z \leq s$. Multiplying both members of equation A.3.16 by $\sin\left(\frac{p\pi}{h} y\right)$, $\sin\left(\frac{q\pi}{s} z\right)$ and integrating in the domains $0 \leq y \leq h$, $0 \leq z \leq s$, we obtain:

$$
\begin{aligned}
&\sum_{\substack{m=1\\n=1}}^{\infty} b_{mn} \cdot (e^{\sqrt{\alpha_{mn}}\cdot w} - e^{-\sqrt{\alpha_{mn}}\cdot w}) \\
&\int_0^h \sin\left(\frac{p\pi}{h}y\right)\cdot\sin\left(\frac{m\pi}{h}y\right)dy \cdot \int_0^s \sin\left(\frac{q\pi}{s}z\right)\cdot\sin\left(\frac{n\pi}{s}z\right)dz = \\
&= T_{hot}\int_0^h \sin\left(\frac{p\pi}{h}y\right)dy \cdot \int_0^s \sin\left(\frac{q\pi}{s}z\right)dz \rightarrow \\
&\rightarrow b_{pq}\cdot(e^{\sqrt{\alpha_{pq}}\cdot w} - e^{-\sqrt{\alpha_{pq}}\cdot w})\cdot\frac{hs}{4} = T_H\cdot\frac{h}{p\pi}(1-(-1)^p)\cdot\frac{s}{q\pi}(1-(-1)^q) \rightarrow \\
&\rightarrow b_{pq} = \frac{16}{(e^{\sqrt{\alpha_{pq}}\cdot w} - e^{-\sqrt{\alpha_{pq}}\cdot w})\cdot pq\pi^2}T_H \equiv \frac{16T_H}{\pi^2}c_{pq}
\end{aligned}
\tag{A.3.17}
$$

Where $p, q = 1, 3, 5...$, because the even numbers give zero in the 3^{rd} line of A.3.17. The temperature A.3.16 becomes:

$$
\begin{aligned}
T(x,y,z) =& \frac{16T_{hot}}{\pi^2}\sum_{m,n=1,3,\dots}^{\infty}\frac{1}{mn}\sin\left(\frac{m\pi}{h}y\right)\sin\left(\frac{n\pi}{s}z\right) \\
& e^{\sqrt{\alpha_{mn}}(x-w)}\frac{1-e^{-2\sqrt{\alpha_{mn}}x}}{1-e^{-2\sqrt{\alpha_{mn}}w}}
\end{aligned}
\tag{A.3.18}
$$

with:

$$
\sqrt{\alpha_{mn}} = \sqrt{-\beta_m - \gamma_n} = \pi\sqrt{\frac{m^2}{h^2}+\frac{n^2}{s^2}} > 0 \tag{A.3.19}
$$

and the temperature of the yellow region:

$$
\begin{aligned}
\Theta(x,y,z) =& \Theta_{Cold} + \frac{16T_{hot}}{\pi^2}\sum_{m,n=1,3,\dots}^{\infty}\frac{1}{mn}\sin\left(\frac{m\pi}{h}y\right)\sin\left(\frac{n\pi}{s}z\right) \\
& e^{\sqrt{\alpha_{mn}}(x-w)}\frac{1-e^{-2\sqrt{\alpha_{mn}}x}}{1-e^{-2\sqrt{\alpha_{mn}}w}}
\end{aligned}
\tag{A.3.20}
$$

A.3.1 *Discussion of the heat transfer through the boundaries*

Formula of the temperature in equation A.3.20 satisfies the boundary conditions A.3.4a, A.3.4b, A.3.4c. In fact:

a) conditions A.3.4b and A.3.4c are satisfied because, for $y = 0, y = h, z = 0, z = s$, in equation in A.3.20 there is a sine function which goes to 0, giving $\Theta(x,0,z) = \Theta(x,y,0) = \Theta(x,h,z) = \Theta(x,y,s) = \Theta_{Cold}$;

b) for $x = 0$, the denominator of the fraction in equation A.3.20 goes to 0, satisfying the first condition of A.3.4a;

c) for $x = w$, the fraction and the exponential are equal to 1 and the remaining series gives the result:

$$\begin{aligned}
&\sum_{m,n=1,3,\ldots}^{\infty} \frac{1}{mn} \sin\left(\frac{m\pi}{h}y\right) \sin\left(\frac{n\pi}{s}z\right) = \\
&= \sum_{m=1,3,\ldots}^{\infty} \frac{1}{m} \sin\left(\frac{m\pi}{h}y\right) \sum_{n=1,3,\ldots}^{\infty} \frac{1}{n} \sin\left(\frac{n\pi}{s}z\right) = \frac{\pi^2}{16} \\
&\rightarrow \Theta(w,y,z) = \Theta_{Cold} + T_H = \Theta_{Hot}
\end{aligned}$$

which satisfies the second condition of A.3.4a.

A.3.2 *Discussion of the temperatures Θ_{Cold} and Θ_{Hot}*

In order to determine these two parameters Θ_{Cold} and T_H, we use a constraint that relates the temperature in the parallelepiped and the heat produced in the illuminated zone. Let us call $\frac{dH_1}{dt}$ the heat passing in the unit time interval through the surface BCB'C' (i.e. the heat received from the parallelepiped ABCDA'B'C'D' per unit time), which satisfies the Fourier Law:

$$\frac{dH_1}{dt} = -k \cdot \int_0^s dz \int_0^h dy \cdot \frac{\partial \Theta(x,y,z)}{\partial x}_{x=w} = -k \cdot \int_0^s dz \int_0^h dy \cdot \frac{\partial T(x,y,z)}{\partial x}_{x=w} \tag{A.3.21}$$

The derivative in A.3.20 is given by:

$$\frac{\partial T(x,y,z)}{\partial x} = \frac{16 T_H}{\pi^2} \sum_{\substack{m=1,3\ldots \\ n=1,3\ldots}}^{\infty} c_{mn} \cdot \sin\left(\frac{m\pi}{h}y\right) \cdot \sin\left(\frac{n\pi}{s}z\right) \cdot \sqrt{\alpha_{mn}} \cdot (e^{\sqrt{\alpha_{mn}} \cdot x} - e^{-\sqrt{\alpha_{mn}} \cdot x}) \tag{A.3.22}$$

After derivative, one has:

$$\begin{aligned}\frac{dH_1}{dt} &= -k \cdot \frac{16T_H}{\pi^2} \sum_{\substack{m=1,3... \\ n=1,3...}}^{\infty} c_{mn} \cdot \sqrt{\alpha_{mn}} \cdot (e^{\sqrt{\alpha_{mn}} \cdot w} + e^{-\sqrt{\alpha_{mn}} \cdot w}) \cdot \\ &\cdot \int_0^h \sin\left(\frac{m\pi}{h} y\right) dy \cdot \int_0^s \sin\left(\frac{n\pi}{s} z\right) dz = \\ &= -k \cdot h \cdot s \frac{16T_H}{\pi^2} \sum_{\substack{m=1,3... \\ n=1,3...}}^{\infty} \frac{\sqrt{\alpha_{mn}} \cdot c_{mn}}{mn} \cdot e^{\sqrt{\alpha_{mn}} \cdot w} (1 + e^{-2\sqrt{\alpha_{mn}} \cdot w}) \equiv \\ &\equiv -k \cdot h \cdot s \frac{16T_H}{\pi^2} \sum_{\substack{m=1,3... \\ n=1,3...}}^{\infty} S_{mn}\end{aligned} \tag{A.3.23}$$

The series element being: $S_{mn} \equiv \frac{\sqrt{\alpha_{mn}}}{m^2 n^2} \cdot \frac{1+e^{-2\sqrt{\alpha_{mn}} \cdot w}}{1-e^{-2\sqrt{\alpha_{mn}} \cdot w}}$

Remark: the heat $\frac{dH_1}{dt}$ is the heat flowing in the direction of the x-axis. Since the temperature decrease is opposite to the x-orientation, the sign is negative, in order to represent the heat flowing from higher to lower temperature. In the case of the NUMEN target, the (positive) heat produced by the ion beam is equal the absolute value $\frac{dH_1}{dt}$ of the heat passing through the surface BCB'C'. The heat $\frac{dH_1}{dt}$ is given by the Bethe-Bloch formula.

A.3.3 *Discussion of the solution $T(x, y, z)$*

Equations A.3.18 and A.3.19 satisfy the Boundary Conditions, in fact:

a) in the cold walls $y = z = 0, y = h$ and $z = s$ the value $T = 0$ is given by the sin functions, while the exponential part is always finished;

b) in the cold wall $x = 0$, the value $T = 0$ is given by the numerator of the exponential fraction;

c) the heat received by the the parallelepiped ABCDA'B'C'D' per unit time through the wall BCB'C' must be equal to the total heat per unit time released through the other 5 surfaces ABCD, A'B'C'D', AA'D'D, ABB'A', DCC'D' (check is done below).

The exponents in A.3.17 are:

$$\sqrt{\alpha_{pq}} \cdot w = \sqrt{\pi^2 \left(\frac{w^2}{h^2} \cdot p^2 + \frac{w^2}{s^2} \cdot q^2\right)} = \pi \frac{w}{s} q \cdot \sqrt{1 + \frac{s^2}{h^2} \cdot \frac{p^2}{q^2}} \tag{A.3.24}$$

BIBLIOGRAPHY

[1] ATLAS Collaboration. "Observation of a new particle in the search for the Standard Model Higgs boson with the ATLAS detector at the LHC". In: *Physics Letters B* 716.1 (2012), pp. 1–29. DOI: https://doi.org/10.1016/j.physletb.2012.08.020.

[2] Y. Fukuda et al. "Evidence for Oscillation of Atmospheric Neutrinos". In: *Phys. Rev. Lett.* 81 (8 1998), pp. 1562–1567. DOI: 10.1103/PhysRevLett.81.1562. URL: https://link.aps.org/doi/10.1103/PhysRevLett.81.1562.

[3] B. Pontecorvo. "Inverse beta processes and nonconservation of lepton charge". In: *Sov. Phys. JETP* 7 (1958). [Zh. Eksp. Teor. Fiz.34,247(1957)], pp. 172–173.

[4] B. Pontecorvo. "Mesonium and Antimesonium". In: *Soviet Journal of Experimental and Theoretical Physics* 6 (1958), p. 429.

[5] Otto Hahn and Lise Meitner. "Uber die Absorption der β-Strahlen einiger Radioelemente". In: *Physikalische Zeitschrift* 9 (1908), p. 321.

[6] "The β-ray spectrum of radium E". In: *Proceedings of the Royal Society of London A: Mathematical, Physical and Engineering Sciences* 175.960 (1940), pp. 71–87. ISSN: 0080-4630. DOI: 10.1098/rspa.1940.0044. eprint: http://rspa.royalsocietypublishing.org/content/175/960/71.full.pdf. URL: http://rspa.royalsocietypublishing.org/content/175/960/71.

[7] Enrico Fermi. "Tentativo di una teoria dei raggi β". In: *Il nuovo cimento* 11.1 (1934), pp. 1–19. DOI: https://doi.org/10.1016/j.physletb.2012.08.020.

[8] B. W. Sargent. "Energy distribution curves of the disintegration electrons". In: *Mathematical Proceedings of the Cambridge Philosophical Society* 28.4 (1932), 538–553. DOI: 10.1017/S0305004100010781.

[9] K.S. Krane. *Introductory Nuclear Physics*. Wiley, 1987. ISBN: 9780471805533. URL: https://books.google.it/books?id=ConwAAAAMAAJ.

[10] C. L. Cowan et al. "Detection of the Free Neutrino: a Confirmation". In: *Science* 124.3212 (1956), pp. 103–104. ISSN: 0036-8075. DOI: 10.1126/science.124.3212.103. eprint: http://science.sciencemag.org/content/124/3212/103.full.pdf. URL: http://science.sciencemag.org/content/124/3212/103.

[11] Abdus Salam and J. C. Ward. "Weak and electromagnetic interactions". In: *Il Nuovo Cimento (1955-1965)* 11.4 (1959), pp. 568–577. ISSN: 1827-6121. DOI: 10.1007/BF02726525. URL: https://doi.org/10.1007/BF02726525.

[12] G. Arnison et al. "Experimental observation of isolated large transverse energy electrons with associated missing energy at s=540 GeV". In: *Physics Letters B* 122.1 (1983), pp. 103 –116. ISSN: 0370-2693. DOI: https://doi.org/10.1016/0370-2693(83)91177-2. URL: http://www.sciencedirect.com/science/article/pii/0370269383911772.

[13] S. R. Elliott, A. A. Hahn, and M. K. Moe. "Direct evidence for two-neutrino double-beta decay in ^{82}Se". In: *Phys. Rev. Lett.* 59 (18 1987), pp. 2020–2023. DOI: 10.1103/PhysRevLett.59.2020. URL: https://link.aps.org/doi/10.1103/PhysRevLett.59.2020.

[14] Giulio Racah. "Sulla Simmetria Tra Particelle e Antiparticelle". In: *Il Nuovo Cimento* 14.7 (1937), p. 322. ISSN: 1827-6121. DOI: 10.1007/BF02961321. URL: https://doi.org/10.1007/BF02961321.

[15] Ettore Majorana. "Teoria simmetrica dell'elettrone e del positrone". In: *Il Nuovo Cimento (1924-1942)* 14.4 (2008), p. 171. ISSN: 1827-6121. DOI: 10.1007/BF02961314. URL: https://doi.org/10.1007/BF02961314.

[16] J. D. Vergados, H. Ejiri, and F. Šimkovic. "Neutrinoless double beta decay and neutrino mass". In: *International Journal of Modern Physics E* 25.11 (2016), p. 1630007. DOI: 10.1142/S0218301316300071. eprint: https://www.worldscientific.com/doi/pdf/10.1142/S0218301316300071. URL: https://www.worldscientific.com/doi/abs/10.1142/S0218301316300071.

[17] M. Fukugita and T. Yanagida. "Barygenesis without grand unification". In: *Physics Letters B* 174.1 (1986), pp. 45 –47. ISSN: 0370-2693. DOI: https://doi.org/10.1016/0370-2693(86)91126-3. URL: http://www.sciencedirect.com/science/article/pii/0370269386911263.

[18] Reyco Henning. "Current status of neutrinoless double-beta decay searches". In: *Reviews in Physics* 1 (2016), pp. 29 –35. ISSN: 2405-4283. DOI: https://doi.org/10.1016/j.revip.2016.03.001. URL: http://www.sciencedirect.com/science/article/pii/S2405428316000034.

[19] Frank T. Avignone, Steven R. Elliott, and Jonathan Engel. "Double beta decay, Majorana neutrinos, and neutrino mass". In: *Rev. Mod. Phys.* 80 (2 2008), pp. 481–516. DOI: 10.1103/RevModPhys.80.481. URL: https://link.aps.org/doi/10.1103/RevModPhys.80.481.

[20] S. Rahaman et al. "Double-beta decay Q values of 116Cd and 130Te". In: *Physics Letters B* 703.4 (2011), pp. 412 –416. ISSN: 0370-2693. DOI: https://doi.org/10.1016/j.physletb.2011.07.078. URL: http://www.sciencedirect.com/science/article/pii/S0370269311008975.

[21] Andrei Neacsu and Mihai Horoi. "An Effective Method to Accurately Calculate the Phase Space Factors for $\beta^-\beta^-$ Decay". In: *Advances in High Energy Physics* 2016 (2016). DOI: https://doi.org/10.1155/2016/7486712.

[22] Jun-Qing Xia et al. "Constraints on massive neutrinos from the CFHTLS angular power spectrum". In: *Journal of Cosmology and Astroparticle Physics* 2012.06 (2012), p. 010. URL: http://stacks.iop.org/1475-7516/2012/i=06/a=010.

[23] J. P. Schiffer et al. "Nuclear Structure Relevant to Neutrinoless Double β Decay: ^{76}Ge and ^{76}Se". In: *Phys. Rev. Lett.* 100 (11 2008), p. 112501. DOI: 10.1103/PhysRevLett.100.112501. URL: https://link.aps.org/doi/10.1103/PhysRevLett.100.112501.

[24] C. J. Guess et al. "The ^{150}Nd(^{3}He,t) and ^{150}Sm(t,^{3}He) reactions with applications to $\beta\beta$ decay of ^{150}Nd". In: *Phys. Rev. C* 83 (6 2011), p. 064318. DOI: 10.1103/PhysRevC.83.064318. URL: https://link.aps.org/doi/10.1103/PhysRevC.83.064318.

[25] Cappuzzello, F. et al. "The NUMEN project: NUclear Matrix Elements for Neutrinoless double beta decay". In: *Eur. Phys. J. A* 54.5 (2018), p. 72. DOI: 10.1140/epja/i2018-12509-3. URL: https://doi.org/10.1140/epja/i2018-12509-3.

[26] N. Auerbach. "Double Charge Exchange Reactions and Double Beta Decay". In: *Journal of Physics: Conference Series* 1023.1 (2018), p. 012032. URL: http://stacks.iop.org/1742-6596/1023/i=1/a=012032.

[27] F. Cappuzzello et al. "Heavy-ion double charge exchange reactions: A tool toward $0\nu\beta\beta$ nuclear matrix elements". In: *The European Physical Journal A* 51.11 (2015), p. 145. ISSN: 1434-601X. DOI: 10.1140/epja/i2015-15145-5. URL: https://doi.org/10.1140/epja/i2015-15145-5.

[28] K. Alfonso et al. "Search for Neutrinoless Double-Beta Decay of ^{130}Te with CUORE-0". In: *Phys. Rev. Lett.* 115 (10 2015), p. 102502. DOI: 10.1103/PhysRevLett.115.102502. URL: https://link.aps.org/doi/10.1103/PhysRevLett.115.102502.

[29] M. Agostini et al. "Results on Neutrinoless Double-β Decay of ^{76}Ge from Phase I of the GERDA Experiment". In: *Phys. Rev. Lett.* 111 (12 2013), p. 122503. DOI: 10.1103/PhysRevLett.111.122503. URL: https://link.aps.org/doi/10.1103/PhysRevLett.111.122503.

[30] F. Cappuzzello et al. "The MAGNEX spectrometer: Results and perspectives". In: *The European Physical Journal A* 52.6 (2016), p. 167. ISSN: 1434-601X. DOI: 10.1140/epja/i2016-16167-1. URL: https://doi.org/10.1140/epja/i2016-16167-1.

[31] M. Cavallaro et al. "Measuring nuclear reaction cross sections to extract information on neutrinoless double beta decay". In: *Journal of Physics: Conference Series* 966.1 (2018), p. 012021. URL: http://stacks.iop.org/1742-6596/966/i=1/a=012021.

[32] A. Calanna. "High-intensity extraction from the Superconducting Cyclotron at LNS-INFN". In: *Nuovo Cimento C Geophysics Space Physics C* 40, 101 (Mar. 2017), p. 101. DOI: 10.1393/ncc/i2017-17101-y.

[33] Peter Sigmund. *Particle Penetration and Radiation Effects*. Springer, 2006. ISBN: 978-3-540-31718-0. DOI: 10.1007/3-540-31718-X.

[34] Balraj Singh. "Nuclear Data Sheets Update for A = 76". In: *Nuclear Data Sheets* 74.1 (1995), pp. 63 –164. ISSN: 0090-3752. DOI: https://doi.org/10.1006/ndsh.1995.1005. URL: http://www.sciencedirect.com/science/article/pii/S0090375285710058.

[35] Jean Blachot. "Nuclear Data Sheets for A = 116". In: *Nuclear Data Sheets* 111.3 (2010), pp. 717 –895. ISSN: 0090-3752. DOI: https://doi.org/10.1016/j.nds.2010.03.002. URL: http://www.sciencedirect.com/science/article/pii/S0090375210000281.

[36] BALRAJ SINGH. "Nuclear Data Sheets for A = 130". In: *Nuclear Data Sheets* 93.1 (2001), pp. 33 –242. ISSN: 0090-3752. DOI: https://doi.org/10.1006/ndsh.2001.0012. URL: http://www.sciencedirect.com/science/article/pii/S0090375201900122.

[37] John P. Greene et al. "Rotating target wheel system for super-heavy element production at ATLAS". In: *Nuclear Instruments and Methods in Physics Research Section A: Accelerators, Spectrometers, Detectors and Associated Equipment* 521.1 (2004). Accelerator Target Technology for the 21st Century. Proceedings of the 21st World Conference of the International Nuclear Target Society, pp. 214 –221. ISSN: 0168-9002. DOI: https://doi.org/10.1016/j.nima.2003.11.411. URL: http://www.sciencedirect.com/science/article/pii/S0168900203030882.

[38] Atsushi Yoshida et al. "High-power rotating wheel targets at RIKEN". In: *Nuclear Instruments and Methods in Physics Research Section A: Accelerators, Spectrometers, Detectors and Associated Equipment* 521.1 (2004). Accelerator Target Technology for the 21st Century. Proceedings of the 21st World Conference of the International Nuclear Target Society, pp. 65 – 71. ISSN: 0168-9002. DOI: https://doi.org/10.1016/j.nima.2003.11.408. URL: http://www.sciencedirect.com/science/article/pii/S0168900203030717.

[39] Mikhail Avilov et al. "A 50-kW prototype of the high-power production target for the FRIB". In: *Journal of Radioanalytical and Nuclear Chemistry* 305.3 (2015), pp. 817–823. ISSN: 1588-2780. DOI: 10.1007/s10967-014-3908-1. URL: https://doi.org/10.1007/s10967-014-3908-1.

[40] F. Pellemoine et al. "Development of a production target for FRIB: thermo-mechanical studies". In: *Journal of Radioanalytical and Nuclear Chemistry* 299.2 (2014), pp. 933–939. ISSN: 1588-2780. DOI: 10.1007/s10967-013-2623-7. URL: https://doi.org/10.1007/s10967-013-2623-7.

[41] T. R. Anthony et al. "Thermal diffusivity of isotopically enriched ^{12}C diamond". In: *Phys. Rev. B* 42 (2 1990), pp. 1104–1111. DOI: 10.1103/PhysRevB.42.1104. URL: https://link.aps.org/doi/10.1103/PhysRevB.42.1104.

[42] F Balestra et al. "Production of a thin diamond target by laser for HESR at FAIR". In: *Journal of Physics: Conference Series* 713.1 (2016), p. 012003. URL: http://stacks.iop.org/1742-6596/713/i=1/a=012003.

[43] V. Grilj et al. "The evaluation of radiation damage parameter for CVD diamond". In: *Nuclear Instruments and Methods in Physics Research Section B: Beam Interactions with Materials and Atoms* 372 (2016), pp. 161 –164. ISSN: 0168-583X. DOI: https://doi.org/10.1016/j.nimb.2015.12.046. URL: http://www.sciencedirect.com/science/article/pii/S0168583X16000021.

[44] S. Prawer and R. Kalish. "Ion-beam-induced transformation of diamond". In: *Phys. Rev. B* 51 (22 1995), pp. 15711–15722. DOI: 10.1103/PhysRevB.51.15711. URL: https://link.aps.org/doi/10.1103/PhysRevB.51.15711.

[45] John M. Andresen. "Graphite and Precursors, World of Carbon; Vol. 1 Edited by Pierre Delhaès. Gordon and Breach Publishers: Amsterdam, 2001; 297 pp. ISBN 90-5699-228-7. $85." In: *Energy & Fuels* 16.1 (2002), pp. 218–218. DOI: 10.1021/ef0101098. URL: https://doi.org/10.1021/ef0101098.

[46] URL: https://industrial.panasonic.com/cdbs/www-data/pdf/AYA0000/AYA0000C27.pdf.

[47] URL: "http://www.optigraph.eu/basics.html".

[48] Y. Bylinskii et al. "Recent Developments for Cyclotron Extraction Foils at TRIUMF". In: International Particle Accelerator Conference 9 (2018). https://doi.org/10.18429/JACoW-IPAC2018-TUPAL062, pp. 1159–1162. DOI: doi:10.18429/JACoW-IPAC2018-TUPAL062. URL: http://jacow.org/ipac2018/papers/tupal062.pdf.

[49] URL: https://www.mathworks.com/products/matlab.html.

[50] J. P. Draayer and K. J. Weeks. "Shell-Model Description of the Low-Energy Structure of Strongly Deformed Nuclei". In: *Phys. Rev. Lett.* 51 (16 1983), pp. 1422–1425. DOI: 10.1103/PhysRevLett.51.1422. URL: https://link.aps.org/doi/10.1103/PhysRevLett.51.1422.

[51] A. T. A. M. de Waele. "Basic Operation of Cryocoolers and Related Thermal Machines". In: *Journal of Low Temperature Physics* 164.5 (2011), p. 179. ISSN: 1573-7357. DOI: 10.1007/s10909-011-0373-x. URL: https://doi.org/10.1007/s10909-011-0373-x.

[52] W. E. Gifford. "The Gifford-McMahon Cycle". In: (1966). Ed. by K. D. Timmerhaus, pp. 152–159.

[53] Michio Inagaki, Yutaka Kaburagi, and Yoshihiro Hishiyama. "Thermal Management Material: Graphite". In: *Advanced Engineering Materials* 16.5 (), pp. 494–506. DOI: 10.1002/adem.201300418. eprint: https://onlinelibrary.wiley.com/doi/pdf/10.1002/adem.201300418. URL: https://onlinelibrary.wiley.com/doi/abs/10.1002/adem.201300418.

[54] P Duthil. "Material Properties at Low Temperature". In: arXiv:1501.07100. arXiv:1501.07100 (2015). Comments: 18 pages, contribution to the CAS-CERN Accelerator School: Superconductivity for Accelerators, Erice, Italy, 24 April - 4 May 2013, edited by R. Bailey, 77–95. 18 p. URL: http://cds.cern.ch/record/1973682.

[55] G. Audi et al. "The Nubase evaluation of nuclear and decay properties". In: *Nuclear Physics A* 729.1 (2003). The 2003 NUBASE and Atomic Mass Evaluations, pp. 3 –128. ISSN: 0375-9474. DOI: https://doi.org/10.1016/j.nuclphysa.2003.11.001. URL: http://www.sciencedirect.com/science/article/pii/S0375947403018074.

[56] URL: ByJatosado-PowerPoint,CCBY-SA3.0,https://commons.wikimedia.org/w/index.php?curid=20296340.

[57] Shunichi Hishita et al. "Sn film deposition on silica glass substrates". In: *Thin Solid Films* 464-465 (2004). Proceedings of the 7th International Symposium on Atomically Controlled Surfaces, Interfaces and Nanostructures, pp. 146 –149. ISSN: 0040-6090. DOI: https://doi.org/10.1016/j.tsf.2004.06.072. URL: http://www.sciencedirect.com/science/article/pii/S004060900400762X.

[58] URL: Photocredit:"https://emresolutions.com/wp-content/uploads/2015/12/Tin_on_carbon-_resolution_standard-3.jpg".

[59] URL: "https://applications.zeiss.com/C125792900358A3F/0/24BC112D50B8038BC1257B$FILE/N_42_011_096_MERLIN_fast_imaging_and_analysis.pdf".

[60] Robert M. Ireland et al. "Tellurium Thin Films in Hybrid Organic Electronics: Morphology and Mobility". In: *Advanced Materials* 25.31 (), pp. 4358–4364. DOI: 10.1002/adma.201203647. eprint: https://onlinelibrary.wiley.com/doi/pdf/10.1002/adma.201203647. URL: https://onlinelibrary.wiley.com/doi/abs/10.1002/adma.201203647.

[61] A. I. GOLOVASHKIN and G. P. MOTULEVICH. "OPTICAL AND ELECTRICAL PROPERTIES OF TIN". In: *SOVIET PHYSICS JETP* 19.2 (), pp. 310–317. URL: http://jetp.ac.ru/cgi-bin/dn/e_019_02_0310.pdf.

[62] Ben Cornelius et al. "The phenomenon of tin pest: A review". In: *Microelectronics Reliability* 79 (2017), pp. 175 –192. ISSN: 0026-2714. DOI: https://doi.org/10.1016/j.microrel.2017.10.030. URL: http://www.sciencedirect.com/science/article/pii/S0026271417305061.